The Study of Exciton-Polariton Phase Transitions Through Spontaneous Vortices and First-Order Correlation

by

Gle Leung

A dissertation submitted in partial fulfillment
of the requirements for the degree of
Doctor of Philosophy
(Physics)
in The University of Michigan
2020

Doctoral Committee:

Professor Hui Deng, Chair
Professor Jennifer Ogilvie
Professor Vanessa Sih
Associate Professor Kai Sun
Professor Herbert G. Winful

Gle Leung

lhofai@umich.edu

ORCID iD: 0000-0002-1223-8679

To those who believed in me, when I didn't believe in myself.

To those who were patient, when I didn't have patience.

To those who deflated my ego, when it got a little too large.

To those who raised me up, when I put myself down.

ACKNOWLEDGEMENTS

The story always begins the same way: an eager, ambitious, confident student arrives in the US hoping to make it big in graduate school. He then meets with numerous trials and tribulations which makes him question his abilities and whether he should be in graduate school in the first place. He was made to face all his weaknesses laid bare, his very identity questioned. With all these factors, it seemed like there was only one way the story would end.

But the story did not end that way. This student is blessed with a fantastic advisor, who could always be counted on for support. He is blessed with amazing mentors, who saw him for the human being that he is, even when he did not. He is blessed with great friends, who taught him to value things outside of academics. He is blessed with a great family, who showered him with love, support and understanding. Through all these blessings, he learned that success can never exist in a vacuum, and that the very fact that this thesis exists is the result of a powerful support network. Among the many lessons this student had learned, the most important one is the value of humanity and humility.

That student is me, and I really do have a lot of things to be thankful for. I would like to thank my advisor, Associate Professor Hui Deng, who never gave up on me and is always patient and supportive. I would like to thank Jiaqi Hu, whose sharp eye and mind has helped me out an uncountable number of times. I would also like to thank my other group mates; Eunice Paik, Rahul Gogna, Long Zhang and Jason Horng, who has provided opportunities for engaging discussion and debate.

There are also my former group members who have since graduated; Paul Bierdz, Bo Zhang, Zhaorong Wang, Lei Zhang, Tyler Hill, Adam Katcher, and Seonghoon Kim. You guys have given me very fond memories. I would also like to thank my friends outside my group, who has taught me a side of American life and culture different from the one portrayed in exported media. Thanks also to Nicole Tuttle from CRLT; my time as a GSIC has taught me a lot of valuable things about teaching that I would probably never have picked up on my own. A big thank you to my committee members, Professor Vanessa Sih, Professor Jennifer Ogilvie, Associate Professor Kai Sun and Professor Herbert Winful, for agreeing to be part of my graduate school journey.

Finally, I would like to acknowledge and thank my family, especially my father. He has given me a lot of valuable advice and I would like to mention the one that I have found most helpful. "A half-bucket makes the most noise, but the noise does not have to be that of arrogance. It could be curiosity." This piece of advice has taught me to be fearless in asking questions and comfortable with not being the smartest guy in the room.

There are simply too many people involved in my journey through graduate school to be all listed in this acknowledgements section. The title 'Doctor of Philosophy' symbolizes the highest level of learning, and it is my hope that I am deserving of it. If not for me, then for all the effort you have put into my education and for all the faith you have in me. Even after this chapter is over, I will not stop being a student of life, and I will do my best to shine my light for others, just as how you have shined your light for me.

TABLE OF CONTENTS

LIST OF FIGURES

Figure

LIST OF TABLES

Table

LIST OF APPENDICES

Appendix

ABSTRACT

Phase transitions are among the most fascinating phenomena discovered in the last century, with collective molecular dynamics leading to novel observations such as superconductivity and superfluidity. Yet even in the highly-ordered state of such systems, defects could still form and persist. Investigating the behavior of such defects is not just a matter of fundamental interest, but also valuable in applications where macroscopic order is important. Our studies of order and defects make use of an exciton-polariton (polaritons hereafter) system. These are quasi-particles with part-matter and part-light components, with a bosonic nature that allows for observation of macroscopic quantum phenomena typically seen in conventional atomic condensates. Their low effective mass allows for such observations at relatively high temperatures (10K - 300K), and the photonic component allows for experimental access using standard table-top optical techniques. These factors have generated much interest in the field of polaritonics over the past two decades. In a two-dimensional system like the polaritons, defects appear in phase transitions as spontaneously-formed vortices. While such vortices have been observed, their reported behaviors were influenced by sample properties or pump configurations. Formation and behaviors in which phase-transition mechanisms and polariton hydrodynamics are primary contributing factors have yet to be observed. Such observations would allow for comparisons with analogous results in atomic condensates and allow for deeper studies in universality. In this thesis, I present efforts taken towards the realization of such observations. I will propose the design of a Compact Mirroring Mach-Zehnder interferometer (CoMMZI) for the detection of photonic orbital angular momentum (OAM) states. The observation of such states would be an unequivocal indication of spontaneously-formed quantum

vortices. I will demonstrate that the proposed interferometer is capable of detecting OAM states with a low number of photons, thereby making it suitable for the detection of moving vortices in a single-shot realization of a polariton condensate. I will then discuss how the interferometer was tested with vortex states formed with a spatial light modulator and continuous-wave lasers. I will show that the interferometer is capable of detecting vortex phases and present techniques to increase the chances of successful detection. I will also show preliminary experiments with a polariton condensate formed with non-resonant pump configurations. OAM states within an optically-induced ring trap have been detected. Finally, I will show spectrometric and temporal first-order correlation functions for polaritons within an optically-induced ring trap, a potential system for the observation of vortices. I will show the presence of three population fractions with coherence times spanning three orders of magnitude and briefly discuss possible implications for vortex-detection experiments. The efforts in this thesis demonstrate the possibilities and challenges associated with the detection of spontaneously-formed vortices within a single instance of a polariton condensate, providing insight for attempts at experimental realizations.

CHAPTER I

Introduction

The last century has seen numerous exciting advances in the area of light-matter science and engineering. Since the photoelectric effect, the development of new technologies have fundamentally changed the way we live. From lasers to LEDs, the field of optical engineering has continued to churn out more marvels, and our knowledge of light-matter interactions have led to state of the art research aimed at creating new technologies that could usher in another renaissance. One such area of research is cavity quantum electrodynamics (QED) [1, 2], which examines the interaction between photons and matter within a reflective cavity. This led to the study of quasiparticles used to describe the resulting hybrid light-matter behavior.

In this work, our focus will be on the quasiparticle known as the exciton-polariton (known hereafter as polaritons), the hybrid light-matter state in which the matter component is an exciton. The strong interaction between the exciton dipole moment and the confined optical field within a microcavity gives rise to two new eigenstates, known as the upper polaritons and lower polaritons [3, 4]. The part-light, part-matter nature of the polaritons allows us to take advantage of either component. The photon component gives a low effective mass, leading to observations of macroscopic quantum phenomena at relatively high temperatures (10 K - 300 K) [5, 6, 7]. The exciton component allows for interaction with surrounding matter, thus enabling

the controlled manipulation of its properties, such as through dispersion engineering [8, 9]. This has made polaritons a strong candidate for applications such as quantum simulators [10, 11, 12] and quantum computers [13].

In addition to their potential for realizing long dreamed-of applications, the bosonic properties of polaritons have also made them an alternative for studies done in cold-atom systems. Polaritons have finite lifetimes limited by the quality factor (Q-factor) of the microcavity. When a polariton decays, it emits a photon carrying the same energy and momentum of the polariton at the time of decay. The emitted photons can then be studied using standard optical methods, such as spectrometry and interferometry. This thus allows for the study of macroscopic quantum phenomenon in an accessible semiconductor environment, rather than the extreme conditions typically required for cold-atom experiments [14]. Some examples of such studies include the observation of Bose-Einstein condensation (BEC) [15, 16], the Berizinskii-Kosterlitz-Thouless (BKT) transition [17, 18], Bogoliubov dispersion [19, 20], Feshbach resonance [21] and quantum vortices [22, 23]. In addition, the exciton and photon fraction can be altered by cavity design, thereby allowing for controlled changes in properties such as the effective mass and oscillator strength.

This work will focus on the spontaneous formation of quantum vortices within a polariton system. These are topological defects that forms in a condensate typically as a result of a phase transition. In a BEC-BKT transition, the evolution of the system into a less ordered phase is associated with the appearance of free vortex-antivortex pairs. The formation of vortices as a result of the merger of localized condensate domains has also been a subject of study in cosmology, known as the Kibble-Zurek mechanism [24]. Experimental studies of this mechanism has been demonstrated in tabletop systems [25], and it is exciting to think that a theory associated with cosmology can also be tested in a microcavity environment. Aside from the accessibility, these studies could also allow for comparisons with vortex behaviors for systems in

thermal and dynamic equilibrium, potentially paving the way for more comprehensive studies of universality. More towards the application side, the formation and persistence of vortices during polariton phase transitions can be a detriment to the coherence of the system, affecting the phase relationships of energy states and resulting in loss of information. It thus is important to understand how vortices are likely to behave in polaritonic devices, and take any necessary steps to circumvent their deleterious effects.

While quantum vortices have been seen in polariton condensates, the observation of spontaneous formation and behavior of vortices in a single shot realization of a condensate has yet to be achieved. Vortices that have been observed thus far have been created by controlled pumping conditions [26, 27, 28], and their behavior have been influenced by such pump conditions or properties of the sample. The observation of spontaneous vortices would be necessary for insight into their formation mechanism and would be revealing of phenomenon predicted in polariton condensates but have not yet been observed, such as the BEC-BKT transition. The experimental observation of how such vortices interact with each other in the absence of other influencing factors would undoubtedly provide insight into polariton hydrodynamics.

In this first chapter, I will begin by giving the relevant mathematics and theory of microcavity polaritons. I will then discuss an important aspect of a successful detection method, optical vortices. By the end of this chapter, the reader would have the knowledge needed to understand the fundamentals of polaritons and appreciate the significance and relevance of this work. More detailed explanations of relevant theories and methods will be given at the beginning of the corresponding chapters.

1.1 Fundamentals of Microcavity Exciton Polaritons

In this section, I will discuss the fundamental physics of microcavities and microcavity polaritons. I will begin by detailing the structure of microcavities and how that

enables effective confinement of light. I will then talk about the basic formulation of exciton-polaritons, such as the Hamiltonian and the transformations necessary to obtain the two polariton eigenstates, the Lower Polariton and Upper Polariton. I will also talk about how various photon and exciton fractions can be obtained. Finally, I will discuss phase transitions in polariton systems and the experimental advantages of using polaritons to study them.

1.1.1 Structure of a microcavity

The basic structure of a microcavity is shown in Figure 1.1 (a). It comprises a central cavity of refractive index n_c, and the thickness of the cavity is an integer multiple of half the cavity wavelength $\lambda_c/2$. Quantum wells are placed at the antinodes of the cavity to maximize the overlap with the photon field, as shown in Figure 1.1(b). The cavity is sandwiched by layers of Distributed Bragg Reflectors (DBR) to form 2 end mirrors. The DBRs comprise alternating layers of materials with refractive indices n_1 and n_2 respectively, and each have a thickness of one quarter the wavelength, $\lambda/4$. At the cavity resonant wavelength λ_c, the transmission of the cavity is greatly increased, given by:

$$T = \frac{(1-R_1)(1-R_2)}{(1-\sqrt{R_1R_2})^2 + 4\sqrt{R_1R_2}\sin^2(\phi/2)}, \tag{1.1}$$

where R_1 and R_2 are the reflectivity of the two end mirrors. The quality or Q factor of the cavity is then given by:

$$Q = \frac{\lambda_c}{\Delta\lambda_c} \simeq \frac{\pi(R_1R_2)^{1/4}}{1-(R_1R_2)^{1/2}}, \tag{1.2}$$

where $\Delta\lambda_c$ is the linewidth of the resonant state. The Q factor represents the average number of round trips the photon makes before leaving the cavity, and thus largely determines the lifetime of the polaritons formed within it (as explained in section (1.1.2) . An ideal cavity would have a Q factor of infinity, in which case the polaritons

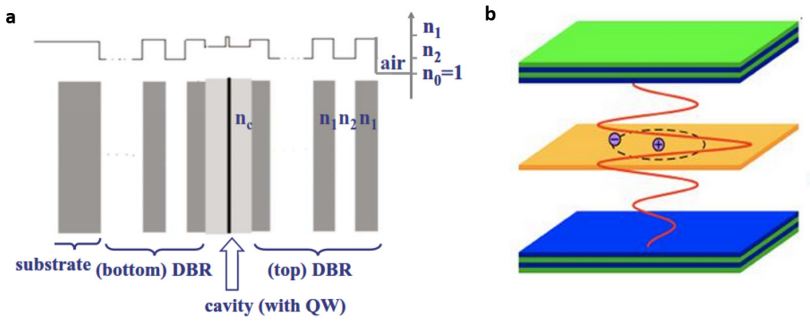

Figure 1.1: The structure of a DBR-DBR microcavity (**a**), taken from [4]. A schematic showing the enhancement of the photon field at the location of the quantum well, to maximize the overlap with the excitons (**b**), taken from `https://web.stanford.edu/group/yamamotogroup/research/EP/EP_main.html`

would have infinite lifetime. The reflectivity of a DBR set increases with the number of layers:

$$R = \left(\frac{n_o(n_2)^{2N} - n_c(n_1)^{2N}}{n_o(n_2)^{2N} + n_c(n_1)^{2N}} \right), \tag{1.3}$$

with N being the number of repeated pairs. Hence, the lifetime of the microcavity polaritons can be increased by increasing the number of layers of the DBRs.

The field of the cavity is confined along its longitudinal axis, but not in the plane of the cavity itself. Hence, the resonant wavelength of the cavity can be altered by changing the angle of incidence of the incoming light. Given an angle of incidence θ, the resonant wavelength would be given by $\lambda_c' = \lambda_c / \cos\theta$, for which λ_c is the resonant wavelength at normal incidence. The cavity energy thus depends on the in-plane wavenumber $k_\parallel = \sqrt{\mathbf{k} \cdot \hat{x}^2 + \mathbf{k} \cdot \hat{y}^2}$. It is given as:

$$E_c av = \frac{\hbar c}{n_c} \sqrt{k_\perp^2 + k_\parallel^2}, \tag{1.4}$$

where $k_\perp = n_c(2\pi/\lambda_c)$ is the wavenumber along the cavity axis. Assuming a small angle of incidence, $k_\parallel$ can be given as:

$$k_{\parallel} \simeq \frac{2\pi}{\lambda_c}\theta \tag{1.5}$$

For such angles of incidence, the cavity energy can be approximated to a parabolic dispersion in $k_{\parallel}$:

$$\begin{aligned} E_{cav} &\simeq \frac{\hbar c}{n_c} k_{\perp} \left(1 + \frac{k_{\parallel}^2}{2k_{\perp}^2}\right) \\ &E_{cav}(k_{\parallel} = 0) + \frac{\hbar^2 k_{\parallel}^2}{2m_{cav}} \end{aligned} \tag{1.6}$$

where $m_{cav} = \frac{E_{cav}(k_{\parallel}=0)}{c^2/n_c^2}$ is the cavity-photon effective mass.

1.1.2 Mathematical description of Microcavity Polaritons

Excitons are formed in a semiconductor when an electron is excited from the valence band into the conduction band. The repulsion it experiences from surrounding electrons form an effective attraction towards the hole created in the valence band. The bound electron-hole pair form a dipole that interacts with an optical field. A simple model of this effect is the oscillation of the electron bound to its hole by a spring, with the oscillation caused by the incident electromagnetic wave. For a wave with frequency ω, the oscillator strength is given as

$$f = \frac{2m^*\omega}{\hbar} |\langle u_v|\mathbf{r}.\mathbf{e}|u_c\rangle|^2 \frac{V}{\pi a_B^3}, \tag{1.7}$$

with m^* the effective mass of the exciton, $|u_c\rangle$ and $|u_v\rangle$ are the Bloch functions of the electron and hole respectively, V is the quantization volume, and a_B^3 is the Bohr radius of the exciton. The Hamiltonian of this interaction between the exciton and the photon can be written as:

$$\begin{aligned}\hat{H} &= \hat{H}_{cav} + \hat{H}_{exc} + \hat{H}_I \\ &= \Sigma E_{cav}(k_\parallel, k_c)\hat{a}^\dagger_{k_\parallel}\hat{a}_{k_\parallel} + \Sigma E_{exc}(k_\parallel)\hat{b}^\dagger_{k_\parallel}\hat{b}_{k_\parallel} \\ &+ \Sigma f(\hat{a}^\dagger_{k_\parallel}\hat{b}_k + \hat{a}_{k_\parallel}\hat{b}^\dagger_{k_\parallel}),\end{aligned} \tag{1.8}$$

where $\hat{a}^\dagger_{k_\parallel}$ is the photon creation operator with the in-plane wave number $k_\parallel$ and the longitudinal wave number $k_c = \mathbf{k} \cdot \hat{z}$ which is determined by the cavity resonance. $\hat{b}^\dagger_{k_\parallel}$ is the exciton creation operator with the same in-plane wave number $k_\parallel$. f is the interaction strength between the exciton dipole and the photon and is described by Equation (1.7). Intuitively, the interaction term can be visualized as the absorption and re-emission of a photon by an exciton. Equation (1.8) can be diagonalized making use of the following transformations:

$$\begin{aligned}\hat{P}_{k_\parallel} &= X_{k_\parallel}\hat{b}_{k_\parallel} + C_{k_\parallel}\hat{a}_{k_\parallel}, \\ \hat{Q}_{k_\parallel} &= -C_{k_\parallel}\hat{b}_{k_\parallel} + X_{k_\parallel}\hat{a}_{k_\parallel}.\end{aligned} \tag{1.9}$$

The Hamiltonian then becomes:

$$\hat{H}_{pol} = \Sigma E_{LP}(k_\parallel)\hat{P}^\dagger_{k_\parallel}\hat{P}_{k_\parallel} + \Sigma E_{UP}(k_\parallel)\hat{Q}^\dagger_{k_\parallel}\hat{Q}_{k_\parallel}, \tag{1.10}$$

where $\hat{P}_{k_\parallel}$ and $\hat{Q}_{k_\parallel}$ represent the creation and annihilation operators of two new eigenmodes, known as the Lower Polariton (LP) and Upper Polariton (UP). The terms $X_{k_\parallel}$ and $C_{k_\parallel}$ are known as the Hopfield coefficients [29], and their squared amplitudes are the exciton and photon fractions of the polaritons. They can be calculated as follows:

$$
\begin{aligned}
|X_{k_\parallel}|^2 &= \frac{1}{2}\left(1 + \frac{\Delta E(k_\parallel)}{\sqrt{\Delta E(k_\parallel)^2 + 4f^2}}\right), \\
|C_{k_\parallel}|^2 &= \frac{1}{2}\left(1 - \frac{\Delta E(k_\parallel)}{\sqrt{\Delta E(k_\parallel)^2 + 4f^2}}\right).
\end{aligned}
\tag{1.11}
$$

They satisfy:

$$
|X_{k_\parallel}|^2 + |C_{k_\parallel}|^2 = 1. \tag{1.12}
$$

Here $\Delta E(k_\parallel)$ is known as the detuning, given as the difference between the cavity energy and exciton energy, $E_{cav}(k_\parallel, k_c) - E_{exc}(k_\parallel)$. The dependence of E_{cav} on k_c thus indicates that the detuning would depend on the resonance energy and thus the thickness of the cavity. For controlled variation of the detuning, wedged cavities with thickness linearly varying along its length are used, and the properties of the polaritons thus depend on the position of the sample under investigation. At $\Delta E(k_\parallel) = 0$, the exciton and photon fractions are equal at $\frac{1}{2}$ each. Using the transfer-matrix method, the energies of the LP and UP across wedged cavities (Figure 1.2) are given as:

$$
E_{LP,UP}(k_|) = \frac{1}{2}\left[E_{exc} + E_{cav} \mp \sqrt{4f^2 + \Delta E(k_\parallel)^2}\right]. \tag{1.13}
$$

An example of LP and UP dispersions are also given in Figure 1.3. Note that the LP's dispersion is closer to that of the cavity photon at lower momentums and closer to the exciton's at higher momentum. The opposite is true for the UP's dispersion.

The polariton effective mass can be determined by the Hopfield coefficients, given as:

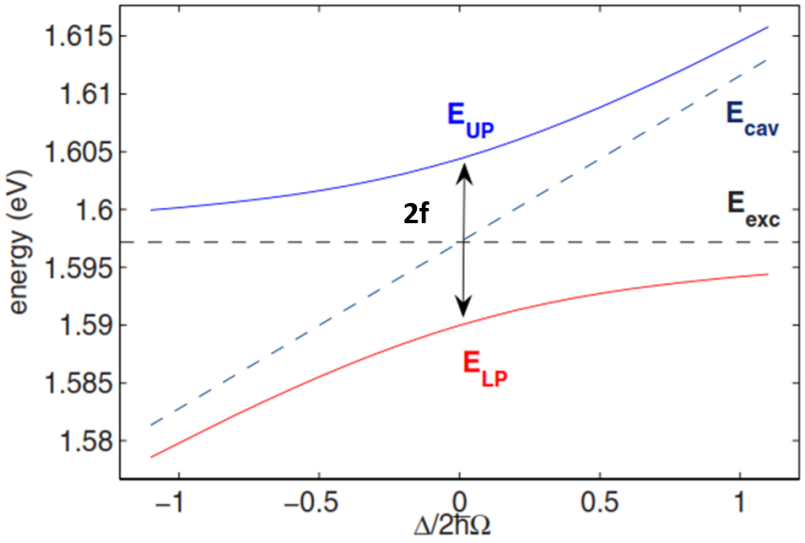

Figure 1.2: Lower (E_{LP}) and Upper (E_{UP}) Polariton energy together with the corresponding cavity (E_{cav}) and exciton (E_{exc}) energy as a function of detuning (Δ). Taken from [4].

$$\frac{1}{m_{LP}} = \frac{|X|^2}{m_{exc}} + \frac{|C|^2}{m_{cav}}, \tag{1.14}$$

$$\frac{1}{m_{UP}} = \frac{|C|^2}{m_{exc}} + \frac{|X|^2}{m_{cav}}. \tag{1.15}$$

The photon's effective mass is on the order of $10^{-5}m_e$, with m_e being the electron mass. Thus, the cavity mass is much smaller than the exciton mass m_{exc}. Hence, Equation 1.14 can be approximated as:

$$m_{LP}(k_{\|} \sim 0) \simeq m_{cav}/|C^2| \sim 10^{-4} m_{exc}, m_{UP}(k_{\|} \sim 0) \simeq m_{cav}/|X^2|. \tag{1.16}$$

The incredibly low effective mass of the LP at low momentums is what allows for phase transitions at relatively high temperatures.

In the next section, I will discuss the basic physics of phase transitions in polaritons.

1.1.3 Phase transitions in polaritons

The semiclassical Boltzmann equations have been used to describe exciton condensation kinetics [30, 31, 32] and cavity polariton relaxation [33, 34, 35, 36, 37, 38]. To understand the processes leading to phase transitions in polaritons, it would be useful to look at them:

$$\begin{aligned} \frac{\partial}{\partial t} n_{\mathbf{k}} &= P_{\mathbf{k}}(t) - \frac{n_{\mathbf{k}}}{\tau_{\mathbf{k}}} + \frac{\partial}{\partial t} n_{\mathbf{k}}\big|_{LP-LP} + \frac{\partial}{\partial t} n_{\mathbf{k}}\big|_{LP-ph}, \\ \frac{\partial}{\partial t} n_0 &= -\frac{n_0}{\tau_0} + \frac{\partial}{\partial t} n_0\big|_{LP-LP} + \frac{\partial}{\partial t} n_0\big|_{LP-ph}. \end{aligned} \tag{1.17}$$

In the above equation, $n_{\mathbf{k}}$ represents the population of the polariton excited states with momentum k. n_o represents the population of the polariton ground state. $P_{\mathbf{k}}$ represents the pumping rate at momentum k, $\tau_{\mathbf{k}}$ is the characteristic decay time of the excited state population and τ_0 is the corresponding decay time for the ground state. The two scattering processes represented in this equation are polariton-polariton scattering (LP-LP) and polariton-phonon scattering (LP-ph).

The LP-phonon scattering rate is given by

$$\frac{\partial}{\partial t}\big|_{LP-ph} = -\sum_{\mathbf{k}'} (W^{LP-ph}_{\mathbf{k}\to\mathbf{k}'} n_{\mathbf{k}}(1+n_{\mathbf{k}'}) - W^{LP-ph}_{\mathbf{k}'\to\mathbf{k}}(1+n_{\mathbf{k}})n_{\mathbf{k}'}), \tag{1.18}$$

where $W^{LP-ph}_{\mathbf{k}\to\mathbf{k}'}$ is the probability of the transition from the state k to state k' and $W^{LP-ph}_{\mathbf{k}'\to\mathbf{k}}$ is the probability of the opposite transition. The LP-LP scattering rate is given by

$$\frac{\partial}{\partial t}\Big|_{LP-LP} = -\sum_{\mathbf{k}'}(W^{LP-LP}_{\mathbf{k},\mathbf{k}',\mathbf{k_1},\mathbf{k_2}} n_{\mathbf{k}} n_{\mathbf{k}'}(1+n_{\mathbf{k_1}})(1+n_{\mathbf{k_2}}) - n_{\mathbf{k_1}} n_{\mathbf{k_2}}(1+n_{\mathbf{k}})(1+n_{\mathbf{k}'})), \quad (1.19)$$

where $W^{LP-LP}_{\mathbf{k},\mathbf{k}',\mathbf{k_1},\mathbf{k_2}}$ it the probability of the transition of two polaritons from initial momentum k and k' to final momentum k_1 and k_2. Between the two scattering processes, LP-LP scattering is the faster process, being able to thermalize the LP gas in a few picoseconds. However, the total energy of the LP gas is reduced by LP-phonon scattering. Both processes thus play important roles in polariton condensation.

The factor $(1 + n_0)$ in the rate equations represent a process known as stimulated scattering, which is also the process distinguishing polariton condensation from regular photon lasing. The final-state occupation number n_o enhances the scattering rate, and at a critical density, this population would see a sharp increase. In many polariton experimental reports, this threshold behavior would be shown in spectrometric measurements, with the increase in population often by 3 orders of magnitude. Since population inversion is not required for threshold to occur, polariton systems have also been touted as a more efficient means of producing coherent light [39]. In large 2-dimensional systems, a true Bose-Einstein condensate is not attainable due to disruptions of the long range coherence by long wavelength phonons [40, 41]. As such, the phase transition within such systems are described as a Berezinskii-Kosterlitz-Thouless (BKT) transition [42]. The BKT transition is an infinite-order phase transition, meaning that there is no discontinuity observed in any of the derivatives of heat capacity across this transition. Rather, it is characterized by a change of the first-order spatial correlation function from a short-range exponentially decaying one to a longer range one with algebraic decay. The BKT transition is also characterized by a binding of free vortex-antivortex pairs, thereby reducing the topological disorder within the system [43]. Nevertheless, it is possible to attain a BEC if the system

is confined within the length scale of fluctuations (such as in microcavity polariton systems), or if the amount of interactions is negligible [44]. This topic will be explored more in Chapter III. Correlation functions will be further explored in Chapter IV. At this point, it is worthwhile summarizing the advantages of a polariton system over an atomic system for research pertaining to phase transitions. The first would be the incredibly low effective mass of the lower polaritons at low momentum, which results in a low density of states. This thus makes it easier to form a degenerate seed of low-energy polaritons, thus enhancing stimulated scattering into the final state. In addition, the dressing of excitons by the vacuum field helps in suppressing the effects of disorders within the sample, and the phase space filling of the excitons can be worked around by using a cavity with multiple quantum wells to dilute the exciton density. These advantages allow for much simpler experimental set-ups that allow for direct observations, as opposed to their atomic counterparts. In the next section, I will discuss an important property of light which is instrumental for studies of vortices forming in polariton condensates.

1.2 Orbital angular momentum of light

In this section, I will go over photon states carrying orbital angular momentum (OAM), often referred to as optical vortices. I will talk about the mathematical description of optical vortices, give a brief explanation on how these states are instrumental to the detection of quantum vortices in polariton condensates, and why such studies are useful for phase transitions.

1.2.1 Mathematical description of optical vortices

Vortex carrying beams can be described with the Laguerre-Gaussian polynomials, given as

$$u(r,\phi,z) = C_{lp}^{LG}\frac{w_o}{w(z)}\left(\frac{r\sqrt{2}}{w(z)}\right)^{|l|}\exp\left(-\frac{r^2}{w^2(z)}\right)L_p^{|l|}\left(\frac{2r^2}{w^2(z)}\right) \exp\left(-ik\frac{r^2}{2R(z)}\right)\exp(-il\phi)\exp(i\psi(z)). \quad (1.20)$$

L_p^l are the generalized Laguerre polynomials, with the closed form

$$L_p^{(l)}(x) = \sum_{i=0}^{p}(-1)^i\binom{p+l}{p-i}\frac{x^i}{i!}. \quad (1.21)$$

C_{lp}^{LG} is the normalization constant, given by

$$C_{lp}^{LG} = \sqrt{\frac{2p!}{\pi(p+|l|)!}}. \quad (1.22)$$

Lastly, $\psi(z)$ is the Gouy phase given by

$$\psi(z) = (|l| + 2p + 1)\arctan\left(\frac{z}{z_R}\right). \quad (1.23)$$

Laguerre-Gaussian polynomials are solutions to the paraxial equation, and thus, any paraxial beam can be described by a superposition of vortex states characterized by the 2 integer quantum numbers l and p. p is the spatial quantum number, and determines the number of nodes present in the transverse amplitude profile of the beam. The orbital angular momentum is described by the number l. In the transverse phase profile of the beam, l determines the phase change going 1 round around the vortex core, given as $2\pi l$. The longitudinal phase of the vortex-carrying beam shows a helical structure, and the number l determines the number of 'twists' within a single wavelength (Figure 1.4). This is also the more important quantum number in vortex detection, as they mostly make use of interferometric or optomechanical methods. In Chapter II and III, I will be discussing one such interferometric method.

The Laguerre-Gaussian polynomials are useful for describing vortex carrying beams in cylindrical coordinates. These beams can also be described in different coordinate systems using different solutions to the paraxial equation, such as Hermite-Laguerre-Gaussian modes and Ince-Gaussian modes for elliptical coordinates [45]. Since we are mostly interested in the phase profile of the beam, we will focus our attention on Laguerre-Gaussian modes in this work.

1.2.2 Utility of optical vortices for the detection of polariton vortices

Optical vortices have found their way into many fascinating applications ever since their discovery in 1992 [46]. Due to their ability to exert optomechanical torque, they have been used in biomedicine and chemistry as optical tweezers for manipulation on the molecular scale [47, 48, 49, 50]. The spiral phase has also been used in phase-contrast microscopy, demonstrating high-resolution micro-imaging. Optical vortices also exist naturally in the cosmic microwave background and have been taken advantage of in astronomical studies [51, 52, 53, 54, 55] and the detection of extra-solar planets. Orbital angular momentum of light can also be used as a degree of freedom in multiplexing, thereby enlarging the capacity for optical communication [56, 57, 58, 59, 60, 61].

In this work, I will discuss the utility of optical vortices for the detection of polariton vortices. As discussed in the beginning of this chapter, polaritons emit a photon with the same energy and momentum at the point of decay. Thus, vortices within the condensate upon decay would transfer their phase information to the emitted photons, after which standard optical vortex detection techniques can be used. In fact, interferometric methods have already been utilized for the detection of such vortices, in references [22] and [23]. However, such methods rely on a large number of photons carrying the vortex phase, and would thus only work if the vortices were stationary or move along a deterministic path over multiple realizations of the

condensate. This thesis describes my work towards a method that would circumvent this problem, and thus enable the detection of spontaneously created vortices in a single realization of polariton condensation.

1.3 Preview of thesis

In Chapter II, I will show simulation results for a proposed method of vortex detection using expected behaviors of a single vortex and vortex-antivortex pairs. I will show that the photon number requirement for this proposed method is much less than existing interferometric methods. In Chapter III, I will describe tests on a compact interferometric method designed to be used for the detection of optical vortices with a low number of photons. The tests will make use of a continuous wave laser and a phase-only spatial light modulator. In Chapter IV, I will show experimental spectroscopic measurements and temporal first-order correlation measurements of long-lifetime polaritons confined within an optically-induced trap. Optically-induced traps would confine polaritons, and thus vortices, within a limited collection area. Spectroscopic and correlation function measurements would be useful in predicting the existence and behavior of polariton vortices. Finally, in Chapter V, I will summarize this work and propose future work towards realizing the detection of spontaneous vortices in a single realization of polariton condensation.

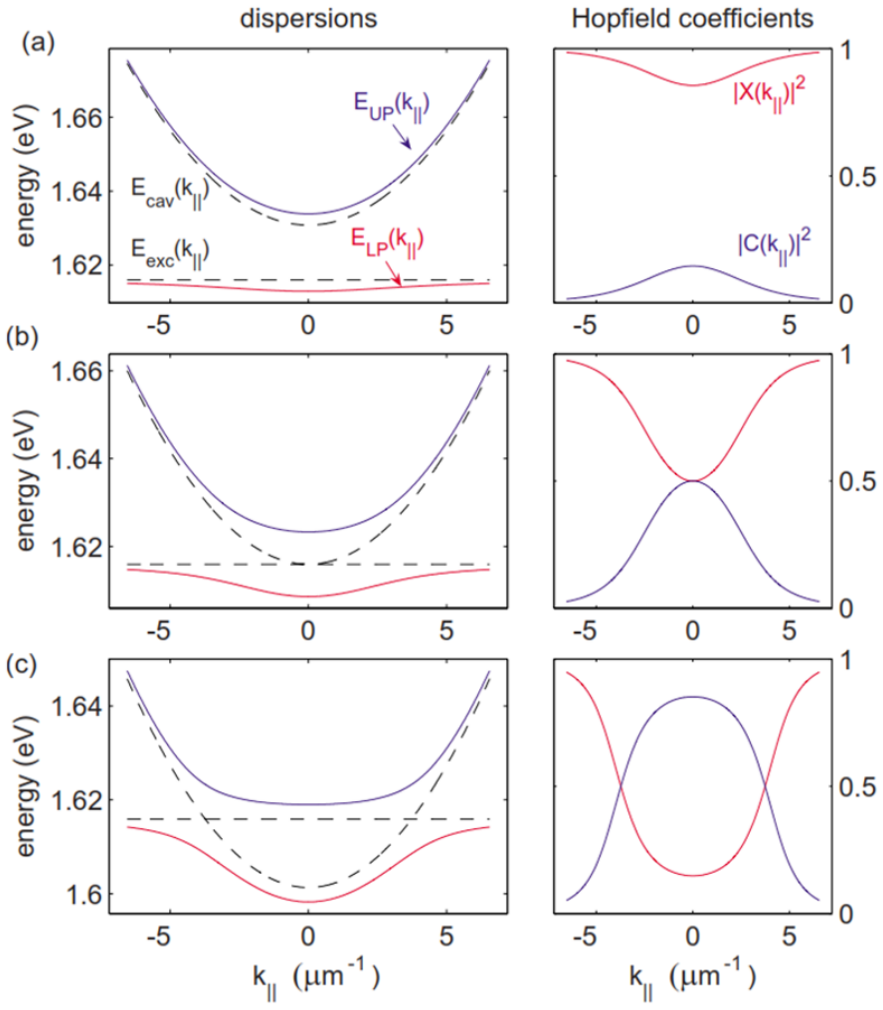

Figure 1.3: Dispersion relationships and corresponding Hopfield coefficients taken for positive (top), zero (middle) and negative (bottom) detuning. Taken from [4].

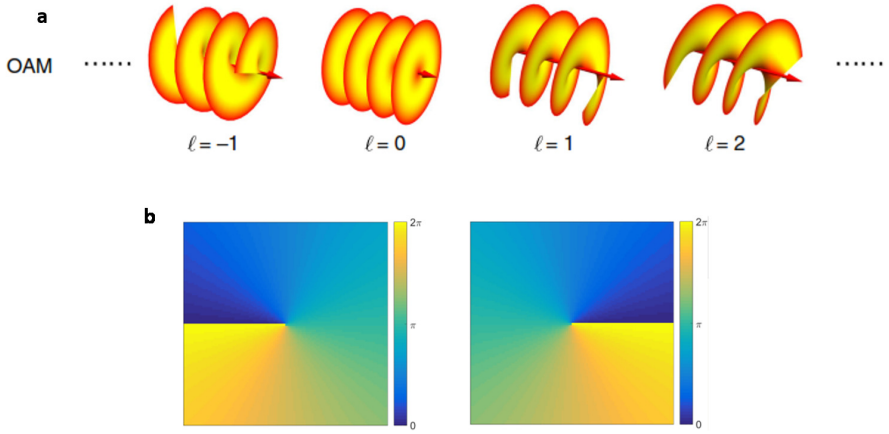

Figure 1.4: **a** shows the helical profile of a vortex-carrying beam , taken from [45]. **b** shows the transverse profile of a l=-1 beam (left) and a l=1 beam (right)

CHAPTER II

Simulating Vortex Detection in Polariton Systems Using Orbital Angular Momentum Interferometry

This chapter will focus on simulations we had done to determine the efficacy of an Orbital Angular Momentum (OAM) Interferometry set-up for the detection of quantum vortices. I will first give some background on quantum vortices, including some studies that have been done on it. I will then discuss the fundamental physics of quantum vortices before talking about their formation in phase transitions in 2-dimensional systems. I will then show a proposal for a compact OAM interferometry set-up before discussing the simulation results. I will show that the proposed set-up would be able to detect optical vortices using a low number of photons.

2.1 Quantum vortices

Quantum vortices are a type of topological defect, a field with a fascinating history. It has its roots in cosmology, being used to explain the formation of large-scale structures in the Universe, and found its way into the laboratory when it was discovered that condensed-matter systems display similar structures upon phase transitions [62, 63, 64, 65, 66, 67, 68, 69]. Experiments involving the observation of such topological defects include liquid crystals, liquid Helium [70, 71], and atomic Bose-Einstein

Condensates [72, 73, 74, 75, 76, 77]. Quantum vortices were the defects observed in the latter two systems. Aside from their formation in phase transitions, quantum vortices can also be created under controlled conditions. They have been formed in superfluids which were rotated by the resonant injection of angular momentum, through changing the ellipticity of the confining potential [78], or by stirring the superfluid with a focused laser beam [79]. Quantum vortices were also found to form in Type II superconductors when an external magnetic field penetrates the material in the form of quantized flux [80, 81]. While most of the focus has been on the fundamental physics, the quantized vorticity and their ability to form entangled states have engendered discussion on using them in quantum computing [82].

Much of the interest in quantum vortices stems from its quantized vorticity, a key distinguishing feature from classical vortices. In the next section, I discuss the physics of quantum vortices from the perspective of superfluidity, and show how its quantized nature leads to various unique properties.

2.1.1 Physics of quantum vortices

Quantized vortices were first predicted by Onsager and Feynman [83] and it initially presented a paradox. Superfluids were known not to rotate, since unlike rigid systems, they have zero curl. Here, I show how this paradox is resolved.

In interacting condensates, the time evolution of the system is given by the nonlinear Schrodinger equation

$$i\hbar\frac{d}{dt}\psi_0(r,t) = \left[-\frac{\hbar^2\nabla^2}{2m} + V_{ext}(r,t) + g|\psi_0(r,t)|^2\right]\psi_0(r,t), \tag{2.1}$$

also known as the Gross-Pitaevskii Equation (GPE). ψ_0 is the order parameter and is given by

$$\psi_0(r,t) = \sqrt{n(r,t)}\exp(iS(r,t)), \tag{2.2}$$

where n (r,t) is the local density of particles. g is the effective potential experienced by the particles and in an interacting condensate, is determined by the interaction strength. S (r,t) is the phase of the order parameter.

The particle current density is defined as

$$j(r,t) = -\frac{-i\hbar}{2m}(\psi_0^*\nabla\psi_0 - \psi_0\nabla\psi_0^*). \tag{2.3}$$

Substituting this with Equation (2.2), we can then rewrite the above as

$$j(r,t) = n(r,t)\frac{\hbar}{m}\nabla S(r,t). \tag{2.4}$$

The superfluid velocity of a condensate particle is thus given by

$$v_s(r,t) = \frac{\hbar}{m}\nabla S(r,t). \tag{2.5}$$

Thus, the superfluid velocity is determined by the gradient of the phase of the order parameter.

For a superfluid rotating around the z-axis, the solution to the GPE can be written as

$$\psi_0(r) = |\psi_0(r)|\exp(il\phi), \tag{2.6}$$

where l needs to be an integer to ensure single-valuedness of the phase. Here we only consider the time-independent portion of the order parameter, and the time-dependent term is assumed to be a separate phase term. Using Equation 2.5 and Equation 2.6, we obtain a new expression for the tangential velocity of the superfluid

$$v_s = \frac{\hbar}{m}|\nabla S| = \frac{\hbar}{m}\frac{1}{r}\frac{\partial}{\partial\phi}S = \frac{\hbar l}{mr} \tag{2.7}$$

The $\frac{1}{r}$ dependence of this velocity thus tells us of the irrotational nature of quantum

vortices. It is notably distinct from rigid rotators of which the velocity is proportional to r. At large distances from the vortex core, the velocity goes to zero and the irrotationality of the superfluid is satisfied. The circulation around the z-axis is given by

$$\oint v_s dl = 2\pi l \frac{\hbar}{m}, \tag{2.8}$$

independent of the radius of the contour. This is the Onsager-Feynman quantization condition. It is also instructive to examine the modulus of the order parameter. If the time-dependent order parameter is of the form

$$\psi_0(r,t) = \psi_0(r)\exp(-i\mu t), \tag{2.9}$$

with $\hbar\mu$ being the chemical potential, the GPE can be rewritten as

$$\left(-\frac{\hbar^2}{2m}\nabla^2 + V_{ext}(r) - \hbar\mu + g|\psi_0(r)|^2\right)\psi_0(r) = 0 \tag{2.10}$$

We then substitute Equation 2.6 into Equation 2.10 to obtain

$$-\frac{\hbar^2}{2m}\frac{1}{r}\frac{\partial}{\partial r}\left(r\frac{d}{dr}|\psi_0|\right) + \frac{\hbar^2 l^2}{2mr^2}|\psi_0| + g|\psi_0|^3 - \hbar\mu|\psi_0| = 0. \tag{2.11}$$

We then assume a solution of the form

$$|\psi_0| = \sqrt{n}f(\eta), \tag{2.12}$$

for which $\eta = r/\xi$ where $\xi = \hbar/\sqrt{2mgn}$ is the healing length, defined as the distance over which the condensate re-acquires its unperturbed value. The real function f(η) satisfies the equation

$$\frac{1}{\eta}\frac{d}{d\eta}\left(\eta\frac{df}{d\eta}\right) + \left(1 - \frac{l^2}{\eta^2}\right)f - f^3 = 0 \tag{2.13}$$

with the constraint of $f(\infty) = 1$. The total energy of the system is given by

$$E = \left(\frac{\hbar^2}{2m} \nabla \psi_0^2 + V_{ext}(r)|\psi_0|^2 + \frac{g}{2}|\psi_0(r)|^4 \right) dr, \tag{2.14}$$

and with the order parameter given by Equation 2.6, and in terms of f(η), it can be written as

$$\begin{aligned} E_v &= E(s \neq 0) - E(s = 0) \\ &= \frac{L\pi\hbar^2 n}{m} = \frac{L\pi\hbar^2 n}{m} \int_0^{R/\xi} \left[\left(\frac{df}{d\eta} \right)^2 + \frac{l^2}{\eta^2} f^2 + \frac{1}{2}(f^2 - 1)^2 \right] \eta d\eta. \end{aligned} \tag{2.15}$$

Here, L is the length of a cylinder for which the system is contained, and R is the radius of that cylinder. For a vortex with non-trivial vorticity, its energy is thus

$$E_v = L\pi n \frac{\hbar^2 l^2}{m} ln \left(\frac{R}{r_c} \right), \tag{2.16}$$

where r_c is the size of the vortex core, typically close in value to the healing length. Thus, we see that the energy of the vortex depends on the square of its vorticity. In systems and processes where vortices spontaneously form, it is thus reasonable to expect that all spontaneous vortices have a vorticity value of 1 or -1.

In the next section, I will discuss a such a mechanism for the formation of quantum vortices: phase transitions in 2-dimensional systems.

2.1.2 Formation of vortices in 2-dimensional phase transitions

In this section, I discuss two mechanisms for vortex formation in phase transitions within 2-dimensional systems, the Berezinskii-Kosterlitz-Thouless transition and the Kibble-Zurek mechanism.

2.1.2.1 Berezinskii-Kosterlitz-Thouless transition

As mentioned in Chapter I, the Berezinskii-Kosterlitz-Thouless (BKT) transition is an infinite order phase transition, and is sometimes referred to as a crossover rather than a transition. It is characterized by the transition from a long range, power-law dependence of the first-order spatial correlation function to a short range exponential one when the temperature of the system rises above a critical value.

The transition to the exponentially decaying correlation function is associated with the appearance of free vortices as bound vortex-antivortex pairs separate [84]. To understand this from a thermodynamic standpoint, we consider the change in free energy during the appearance of a vortex

$$\Delta F = \Delta U - T\delta S \tag{2.17}$$

where ΔU is given by Equation 2.16. The change in entropy ΔS for the appearance of a vortex is given by

$$S = k_B ln W = k_B ln \left(\frac{R^2}{r_c^2}\right) \tag{2.18}$$

for which the number of microstates W is determined by the number of possible sites that a vortex can be located in the system. This does assume that the vortex core is much smaller than the system size and thus may differ in polariton systems where the healing length is typically on the same order as the system size. It would be interesting to see if vortex formation in a finite polariton system deviates from expectations because of this, but for the purpose of this work, it will be assumed that the above equation holds.

The change in free energy is thus given by

$$\Delta F = (L\pi n \frac{\hbar^2 l^2}{m} - 2k_B T) ln \left(\frac{R}{r_c}\right) \tag{2.19}$$

Thus, above a certain critical temperature, the appearance of vortices would result in the entropy term $T\Delta S$ exceeding the increase in internal energy ΔU. The change in free energy is negative and it becomes energetically favorable for vortices to form in the system. This critical temperature is given by

$$T_B = L\pi n \frac{\hbar^2 l^2}{2mk_B} \tag{2.20}$$

2.1.2.2 Kibble-Zurek mechanism

In a system that is cooled adiabatically, the entire population undergoes phase transition at the same time. There is thus only one defined global phase in such a quench. If the system is cooled rapidly however, localized domains with their own phase are 'frozen' during the transition. Eventually, the various domains merge into a global phase and if the relative phases of the merging domains allow, quantum vortices form with the core at the intersection points.

Assuming a system in equilibrium characterized by a correlation length ξ, given by

$$\xi \propto |T - T_c|^{-\nu}, \tag{2.21}$$

in which T is the temperature and T_c is the critical temperature for phase transition. ν is the critical exponent that characterizes the divergence of ξ. The relaxation time τ needed to acquire diverging conditions is given by

$$\tau \propto \xi^z, \tag{2.22}$$

where z is another critical exponent. For Bose-Einstein condensation, ν has a value of 1/2 and z has a value of 3/2. From the above two equations, it can be seen that establishing equilibrium becomes more difficult as the critical temperature is approached. This is known as critical slowing down. When the relaxation time

becomes larger than the time before reaching the phase transition, the system becomes 'frozen' and the correlation length takes on a value different from the equilibrium one, ξ'. This then results in the formation of multiple domains with independent values of the order parameter and phase.

We assume a linear decrease in temperature with time,

$$\frac{T(t)}{T_c} = 1 + \frac{(t_c - t)}{\tau_Q} \tag{2.23}$$

with τ_Q being the characteristic quench time, T_c the critical temperature and t_c being the time in which the phase transition is reached. From this assumption, the domain size [69] is given as

$$\xi' \propto \left(\frac{\tau_Q}{\tau}\right)^{\frac{\nu}{1+\nu z}}. \tag{2.24}$$

The average number of phase defects, appearing as vortices, is given thus given as

$$N_d \propto \left(\frac{\tau}{\tau_Q}\right)^{\frac{\alpha\nu}{1+\nu z}}, \tag{2.25}$$

where α is a constant depending on the dimensions of the system and the vortices [64]. Thus, the number of vortices formed in a system undergoing rapid quenching can be counted and compared with predictions by the Kibble-Zurek model.

In this context, a polariton system differs from an atomic system largely due to the fact that temperature remains a constant during the experiment, and that the critical parameter is density. As such, defect density and correlation lengths of the system would be determined by the relaxation time which in turn is determined by factors such as the interaction strength. Polaritons with larger excitonic fraction can thus be expected to have a faster relaxation time and thus a smaller number of vortices formed by the Kibble-Zurek mechanism. A Kibble-Zurek-like mechanism has been numerically studied for a polariton condensate [85] and has shown that this takes

place.

2.2 The Compact Mirroring Mach-Zehnder Interferometer

Our proposed method involves phase identification through interferometry. The big challenge in detecting spontaneous vortices in a single realization of a polariton condensate stems from the relatively low number of photons in the photoluminescence signal (PL). Since orbital angular momentum states of light are primarily defined by its unique phase, many methods for its detection involve interferometry. However, forming a well-defined interference pattern (interferogram) requires a large number of photons. In this section, I discuss the design of the compact OAM interferometer. I will present the original inspiration of the design and show how it works. I will then present my own design and discuss how it solves the issues the original design has.

Figure 2.1 shows the original design conceived by Leach et al [86]. The design is Mach-Zehnder interferometer set-up with two dove prisms in each arm, placed at 90 degree angles relative to each other. The figure illustrates the action of the interferometer on a beam with a centered optical vortex with topological charge $l = 1$, though the same action will be performed on any beam with an odd value of l (l = 1,3,5...). In the arm with the upright Dove prism, the beam undergoes a top-bottom inversion. In the arm with the Dove prism on its side, the beam undergoes a left-right inversion. When the two beams recombine at the second beam splitter, they are at a π phase difference relative to each other. As such, they undergo destructive interference at one port of the beam splitter, hereafter known as the 'even' port. In the other port, the reflected beam undergoes another π phase shift and constructive interference occurs instead. This port will hereafter be known as the 'odd' port. If a non vortex-carrying beam or a beam with an even value of l (l = 0,2,4...) were to enter the interferometer, constructive interference will occur at the even port and destructive interference takes place at the odd port instead. The success of Leach's design

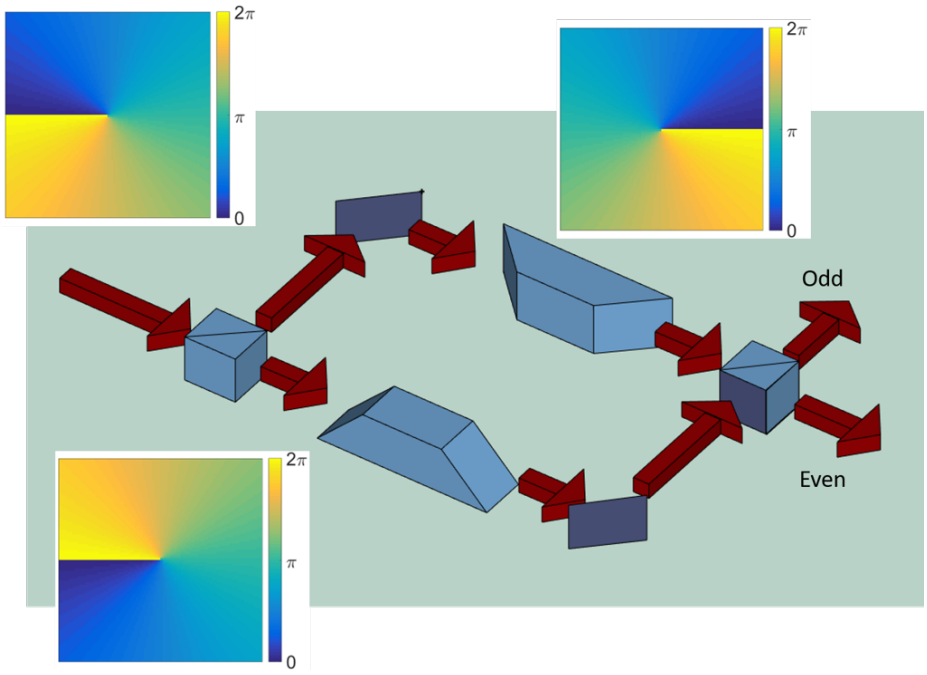

Figure 2.1: The design of an OAM sorting interferometer by Leach et al. The phase profile of a vortex beam with l=1 is shown to demonstrate the action of the interferometer on the beam in each arm. The odd/even labels of the output of the second beamsplitter refer to the port in which constructive interference takes place if the beam has an odd/even value of l.

depends very much on the meticulous alignment of the various optical components. For optimal contrast between the two ports, the two beams should be collinear at the second beamsplitter and have equal path lengths. With 24 degrees of freedom across all optical components, this set-up is highly susceptible to thermal and mechanical drift within the laboratory environment, even if the original alignment was done well.

To solve such issues, a compact version of this interferometer was conceived by Lavery et al [86]. The design, shown in Figure 2.2, eliminates any free space path after the splitting of the beam at the first beam splitter. The mirrors are replaced with right-angled prisms and the Dove prisms were replaced with custom M-shaped prisms. These prisms are positioned with the same relative angle as in Leach's design, and the beam is inverted in a similar manner as in the Dove prisms. With Lavery's design, the number of degrees of freedom has been reduced to 5, making the overall

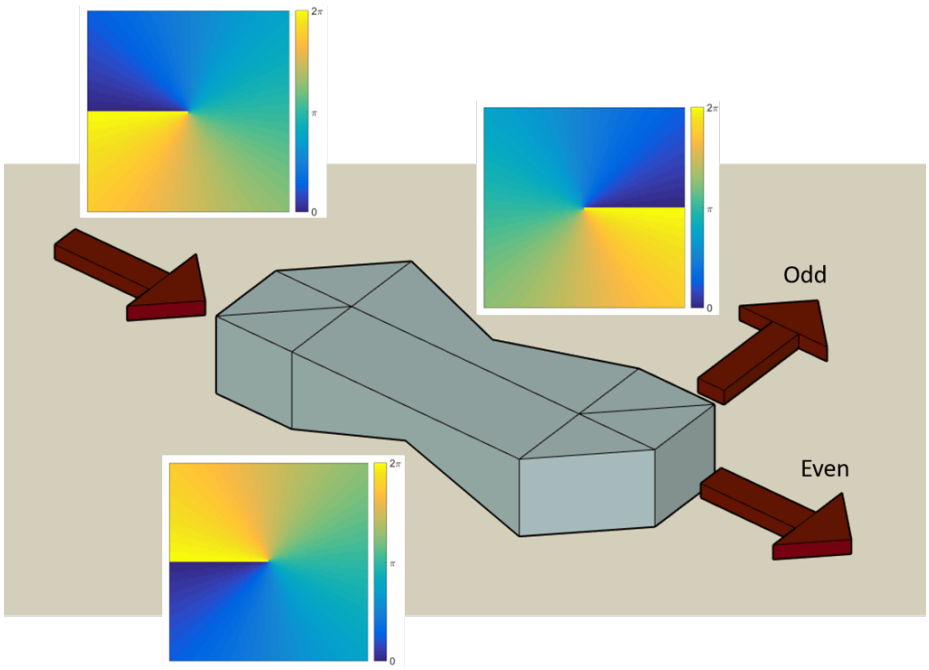

Figure 2.2: The design of a compact version of the OAM sorting interferometer shown in Figure 2.1 and introduced by Lavery et al. [87]. Two custom M-shaped prisms take the place of the free-space arms and dove prisms.

set-up much more stable. This design has also been tested to be effective in sorting odd and even orbital angular momentum states.

Despite the compactness and simplicity, Lavery's design has its share of issues; the main issue being that the M-shaped prisms are difficult to manufacture. In attempting to recreate the design, we had wanted to avoid using prisms that were made of two separate parts glued together with epoxy, out of concern for its effect on the beam quality. However, the resulting single-piece prism was expensive to make, with few manufacturers capable of doing so. In addition, we were also concerned that the narrow middle portion may be susceptible to breakage.

As such, I developed a new but conceptually similar design. This is shown in Figure 2.3. The PL signal is first split into two paths, with one path entering a large dove-like prism to undergo left-right inversion, while the other path is directed into a smaller Dove-like prism by right-angled prisms to undergo top-bottom inversion.

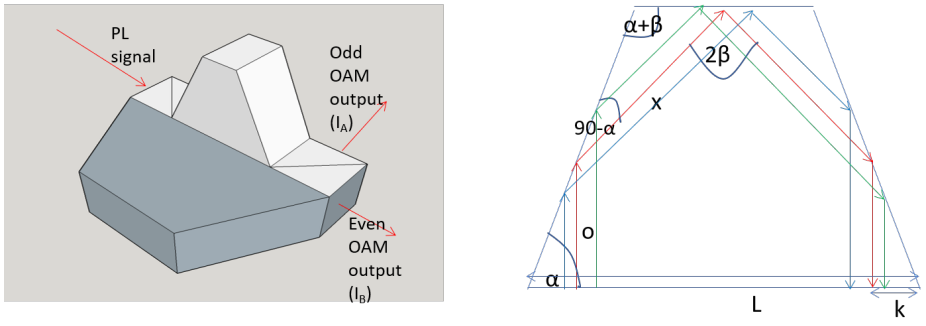

Figure 2.3: The design of the Compact Mirroring Mach-Zehnder Interferometer. The beam undergoes inversion in the custom dove-like prisms. The beam is directed into the smaller, upright prism using 2 retroreflectors.

Unlike normal Dove prisms, these Dove-like prisms do not have 45 degree apex angles (α in Figure 2.3). Just as with the M-shaped prisms, these are designed to force the beam to undergo 3 reflections to achieve inversion. These Dove-like prisms turned out to be far easier and far less expensive to make. Hereafter, this design will be known as the Compact Mirroring Mach-Zehnder Interferometer (CoMMZI).

Just as with Lavery's design, the CoMMZI has a total of 5 degrees of freedom in its alignment. The first 4 come from the two mirrors used to align the beam prior to entering the first beam splitter, while the 5th is the position of the large Dove-like prism. In Lavery's design, the 5th degree of freedom is the position of one of the right-angled prisms. This also highlights another advantage of the CoMMZI's design. Since the large prism is more easily removed from the overall structure, it is therefore easier to plan the translation stage platforms which holds all the components. The large prism is placed on its own piezo-controllled stage while the other components are placed on their own immobile platforms. One precautionary measure we needed to take was the placement of the small Dove-like prism on top of the right-angled prisms. Abrasive placement would cause damage to the anti-reflection coating on the bottom of the prism, and the experimenter should not try to shift the prism once it has been put in place. The measurements for the large and small prism are shown

in Appendix A.2. In the next section, we discuss simulations of vortex behaviors and the ability of the CoMMZI to detect such situations.

2.3 Simulating CoMMZI detection for expected vortex behavior

With vortices one of the most important features in 2D condensates, numerous studies on vortices in polariton condensates have been carried out. These studies include vortices produced by sample defects [23, 22] and artificial barriers [88, 89, 90], vortices created by direct injection of orbital angular momentum [91, 28, 92, 93], and vortex formation in the Optical Parametric Oscillator regime [94, 95, 96, 97]. Vortices have also been generated through the breaking of radial symmetry [27, 98] and perturbations to a condensate minimum [26]. Vortex lattices have also been found to form in traps [99]. Despite these accomplishments, experimental observations of vortices formed from the BKT transition and KZ mechanism, along with their subsequent behavior unaffected by localizing mechanisms, have yet to be achieved. The primary reason why such observations have not been made lies in the existing detection method for polariton vortices. To our knowledge, the only way polariton vortices have been observed is through the use of Michelson interferometry, which depends on a relatively large number of photons and the vortices having a well-defined average position, which would result in a clear fork interference pattern at the location of the vortex core. In the absence of deterministic flow, vortices do not generally meet these criteria. The resulting reduced interferometric contrast along with the relatively low number of photons expected from a single realization of a condensate, make observing fork interference patterns of randomly appearing and/or moving vortices challenging. In this section, we propose a method to detect the existence of random polariton vortices that require only very few photons collected

by presently available detectors. We first illustrate the ineffectiveness of Michelson interferometry with low photon numbers, with the examples of a single vortex and a vortex-antivortex pair. We will then show how our method can enable the detection of the existence of vortices with as low as ≈ 10 photons. Finally, we will evaluate the effects of vortex core radii on our results.

2.4 Modelling and analysis

A polariton vortex is generally described as:

$$\Psi = f(r)\exp(il\phi). \tag{2.26}$$

Since the energy of the vortex increases quadratically with charge, we will restrict our analysis to only $l = 1$. For the amplitude profile $f(r)$, we will use a hyperbolic tangent profile, or $f(r) = \tanh(\frac{r}{r_c})$, a known dark soliton solution in Bose-Einstein condensates [100]. r_c is the radius of the vortex core, which we will assume to be 1 μm [23]. We discuss three specific scenarios of vortex behavior. Figure 2.4 to Figure 2.6 shows the intensity (left) and phase (right) profiles for each scenario, along with the vortices' location at an earlier and later time. In all 3 scenarios, the vortices are moving from the top to bottom of the collection area. The first scenario, S1, is a single vortex moving across the collection area. S2 is a vortex-antivortex pair with a fixed separation moving across the collection area. S3 is a vortex-antivortex pair moving while separating or recombining at the same time. We define the angle of separation, θ, as the angle between vertical – the direction the center of the pair moves along – and the direction the vortex moves along, as illustrated in Figure 2.6. Positive θ corresponds to separating vortices while negative θ, recombining ones. Separation occurs when there are repulsive forces, such as the interaction of the condensate with a large central polariton population arising from a focused pump spot, and recombination

could happen if forces arising from interactions with a reservoir causes the pair to lose energy [101]. We also examine the dependence on the velocity of the vortex and consider velocities between 0.1 μm/ps and 1 μm/ps [101, 22]. We will use a 50 by 50 μm collection area on a 200 by 200 grid, a 0.2 ps time step and a fixed integration time of 100 ps.

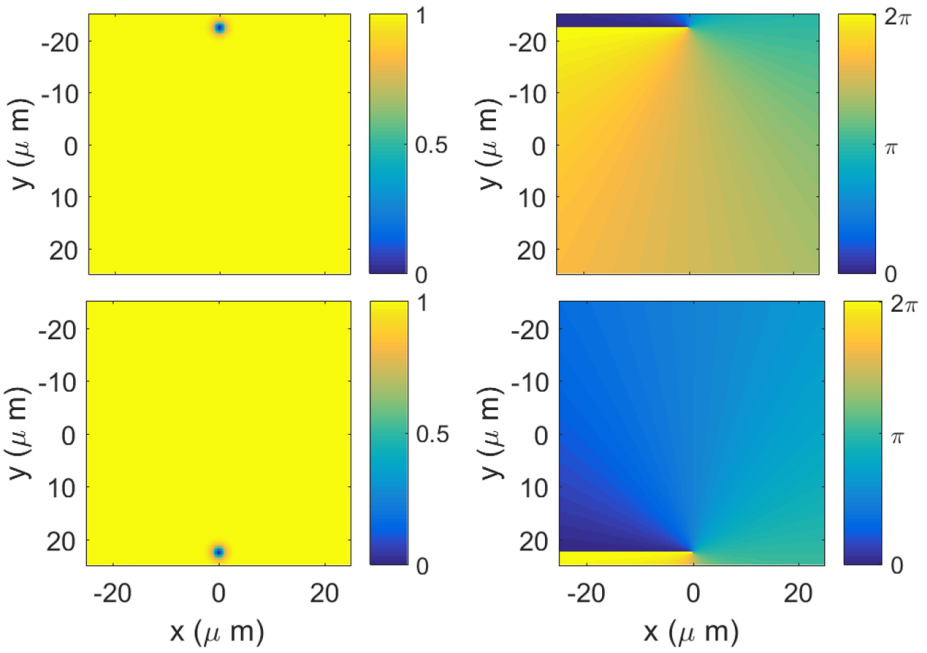

Figure 2.4: One scenario considered is a single vortex moving from the top to bottom edge of the collection area (S1). The left column depicts the intensity profile at 0ps (top) and after 100ps (bottom). The right column depicts the corresponding phase.

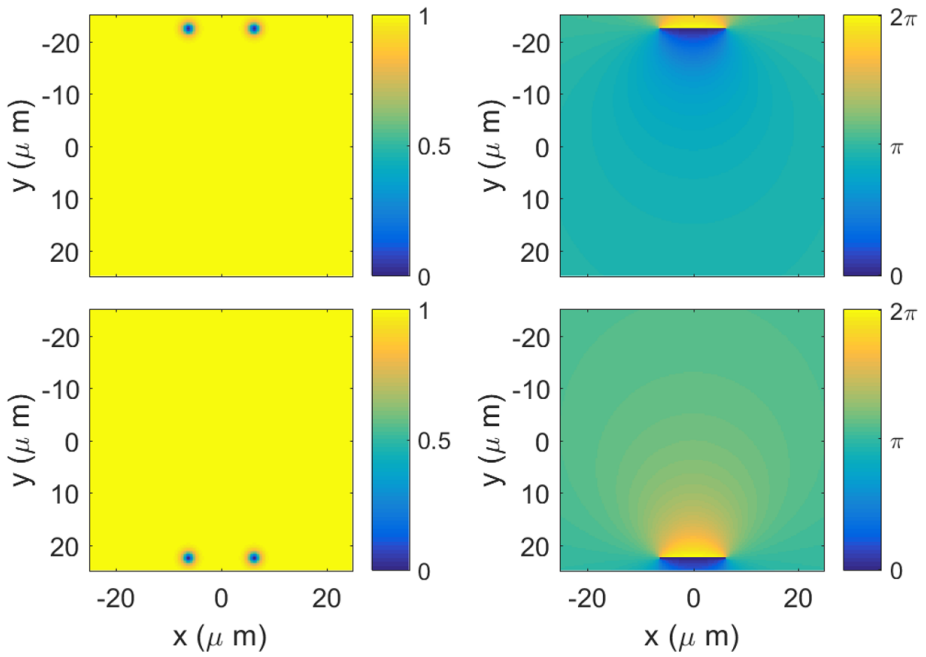

Figure 2.5: One scenario considered is a vortex-antivortex pair moving from the top to bottom edge of the collection area (S2). The left column depicts the intensity profile at 0ps (top) and after 100ps (bottom). The right column depicts the corresponding phase.

2.4.1 Analysis of Michelson intererometry's capability for vortex detection

We first evaluate a Michelson interferometer for detection of the moving vortices. The intensity output of a Michelson interferometer can be described by:

$$I_{Michelson}(x,y) = \int_0^T \left|\Psi(x,y,t)\exp(i\mathbf{k}\cdot\mathbf{x}) + \Psi(-x,y,t)\exp(-i\mathbf{k}\cdot\mathbf{x})\right|^2 dt, \tag{2.27}$$

$$\Psi(x,y,t) = f(x - R_{x,v}(t), y - R_{y,v}(t))f(x - R_{x,av}(t), y - R_{y,av}(t))\exp(i\Phi(x,y,t)), \tag{2.28}$$

where $R_{x,yv,av}(t)$ and $\Phi(x,y,t)$ represent the position of the vortex/anti-vortex and the transverse phase at time t respectively. T is the total integration time of 100 ps. In addition to finding the expected intensity distribution, we also calculated the

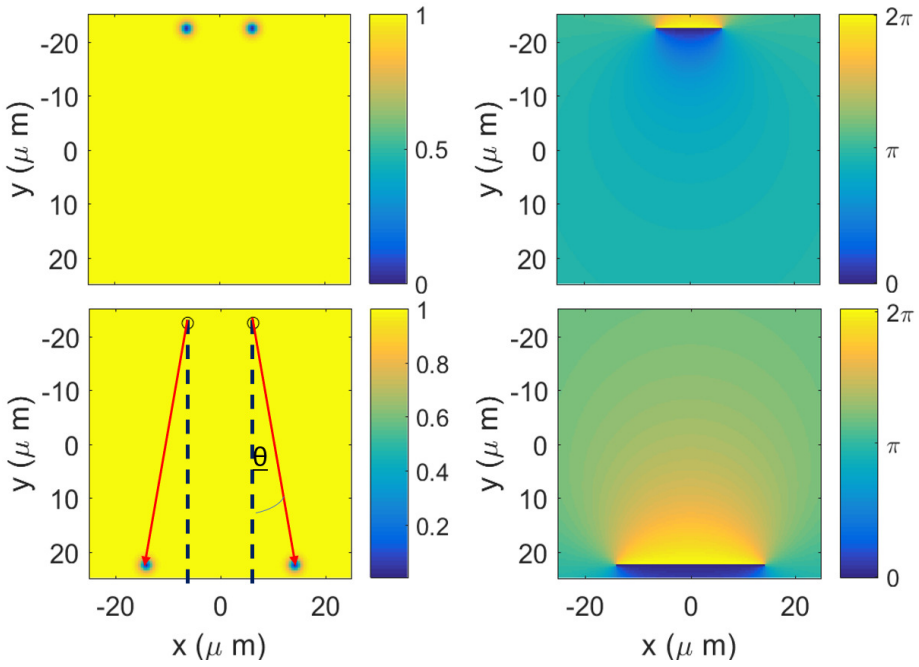

Figure 2.6: One scenario considered is a vortex-antivortex pair moving from the top to bottom edge of the collection area at an angle (S3). The left column depicts the intensity profile at 0ps (top) and after 100ps (bottom). The right column depicts the corresponding phase. The separation angle θ is defined as the angle between the vertical and the line of movement of the vortices. Positive values of θ indicate separating vortices while negative values indicate recombining vortices.

intensity profile for a limited number of photons. 1000 photons were distributed across a grid using a probability distribution that is normalized from the expected intensity distribution. We used a 100 by 100 grid instead of the original 200 by 200 one, which simulates the focusing of the output beams of the interferometer into a smaller area. This would increase the signal to noise ratio in an image acquisition device , which is an important consideration in a single-shot experiment. We chose to use 1000 photons to reflect an upper limit to the number of photons produced in a single realization of the condensate, a 3 order of magnitude increase from threshold. [15].

Figure (2.7) shows $I_{Michelson}$ for S1 and S2. For each scenario, both the expected intensity distribution (left) and the corresponding single shot (right) interferograms

are shown. In S1, fork patterns with reduced contrast can be seen near the center if there are enough number of photons to form the interferogram (left image), since the vortex moves across only a fifth of the length of the collection area over the integration time. However, no discernable features can be seen when only 1000 photons are collected. For S2, no fork patterns are seen even in the expected intensity distribution. This is due to the overlap of vortex phases that are exactly π out of phase with each other.

2.4.2 Analysis of CoMMZI's capabilities for vortex detection

In this section, we discuss how we calculate, for each scenario, the minimum number of photons required by the CoMMZI to conclusively detect the vortex/anti-vortex above incoherent background or shot noise. At time t, the average intensity expected from the odd and even ports of the OAM interferometer is:

$$I_{e,o}(x,y,t) = \left| \frac{1}{2}\Psi(x,y,t) \pm \frac{1}{2}\Psi(-x,-y,t) \right|^2, \tag{2.29}$$

where $\Psi(x,y,t)$ is defined in Section (2.4.1), I_e and I_o are the even and odd intensities respectively. The time integrated intensity is:

$$\tilde{I}_{e,o}(x,y) = \int_0^T I_{e,o}(x,y,t)dt. \tag{2.30}$$

Using these intensities, we define our vortex visibility V as the expected normalized intensity differences between the odd and even ports:

$$|V| = |f_e - f_o| = \frac{\int\int \left| \tilde{I}_e(x,y) - \tilde{I}_o(x,y) \right| dxdy}{\int\int \left| \tilde{I}_e(x,y) + \tilde{I}_o(x,y) \right| dxdy}, \tag{2.31}$$

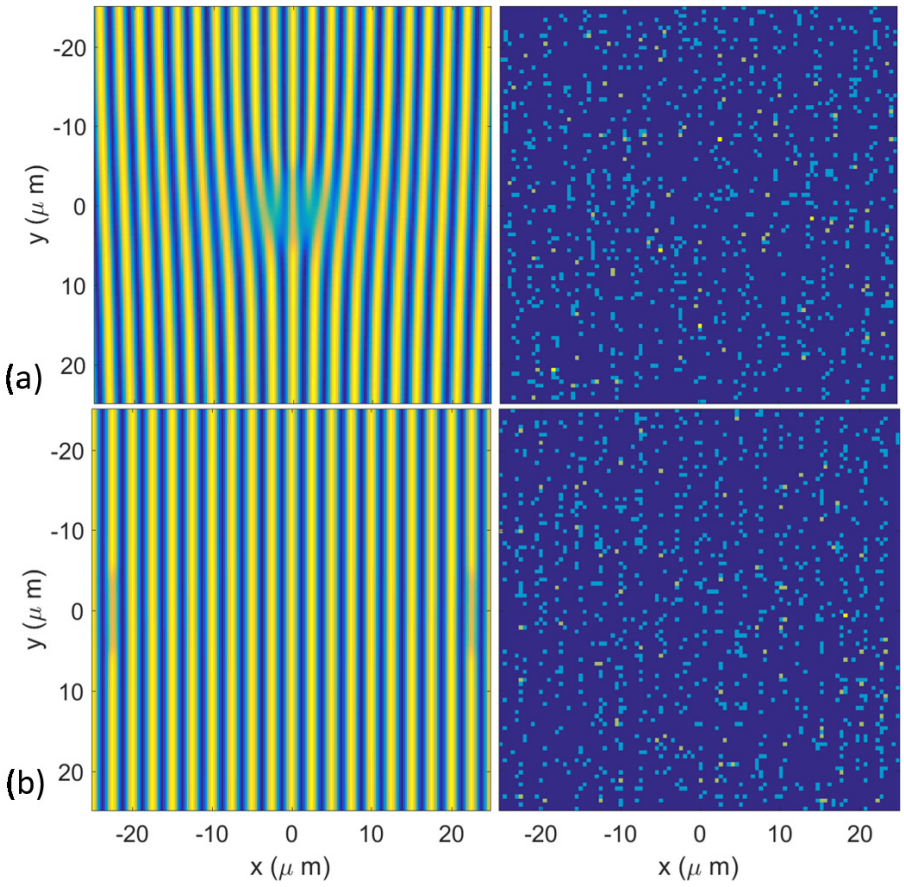

Figure 2.7: Michelson interference images depicting S1 (a) and S2 (b) beside the corresponding images with 1000 photons. The interference images were calculated on a 200 by 200 grid, while the 1000 photon images were produced on a 100 by 100 grid interpolated from the original one. For S1, the vortex starts at $y = -4.7\mu$ m and moves at a speed of 0.1μm/ps. For S2, the vortex-antivortex pair starts at $y = -4.7\mu$m and moves at a speed of 0.1μm/ps while maintaining a separation of 0.9 times the collection area's length.

where the integration is over the detection area, and f_o and f_e are the fractions of photons exiting the odd port and the even port, respectively. A negative value, $V < 0$ beyond the shot noise, corresponds to successful detection of the existence of vortices.

We set a criterion for successful detection when the photon number from the odd port exceeds the photon number from the even port by a confidence level of 99.7%. Assuming both photon numbers follow a Poisson distribution and are independent of each other, we can then calculate the minimum average photon number for successful

detection using

$$|V| * \bar{n} = 3 * \sqrt{\bar{n}}, \tag{2.32}$$

where $\bar{n}$ is the minimum average photon number.

2.4.3 Results

In this section, we present our results for our calculations of the visibility from Equation (2.31) and the minimum average photon number, $\bar{n}$ using Equation (2.32) for the three scenarios S1, S2 and S3.

For S1, the vortex visibility V is shown in Fig.2.8a as a function of the speed of the vortex from 0.1μm/ps to 1μm/ps, and the starting position along the y-axis from $y = -25\mu$m to $y = 0\mu$m.

In the limit of a very slowly moving vortex that starts near the center of the collection area, it can be approximated as a single stationary vortex. In this case, total constructive (destructive) interference takes place in the odd (even) port, giving a maximum positive visibility $V = 1$, corresponding to the lower right corner in the plot. As an example, for a vortex starting at $y = -4.7\mu m$ with a speed of 0.1μm/ps, $V = -0.94 \pm 0.01$, corresponding to $\bar{n} = 11 \pm 1$. Its intensity output at the odd and even ports are shown in Figure 2.8c. In the opposite limit of a fast moving vortex, starting at the same position, it quickly leaves the collection area, and for most of integration time, we measure a beam without vortex. This results in a visibility closer to the maximum negative value of $V = -1$, corresponding to the upper right corner in the plot. An an example, for a vortex starting at $y = -4.7\mu m$ with a speed of 0.96μm/ps, $V = 0.42 \pm 0.01$. As the vortex moves farther from the center of the beam, less constructive (destructive) interference takes place in the odd (even) port due to a smaller overlap of the vortex phase. For this reason, vortices starting farther from the center would result in a more negative visibility, regardless of the speed of the vortex.

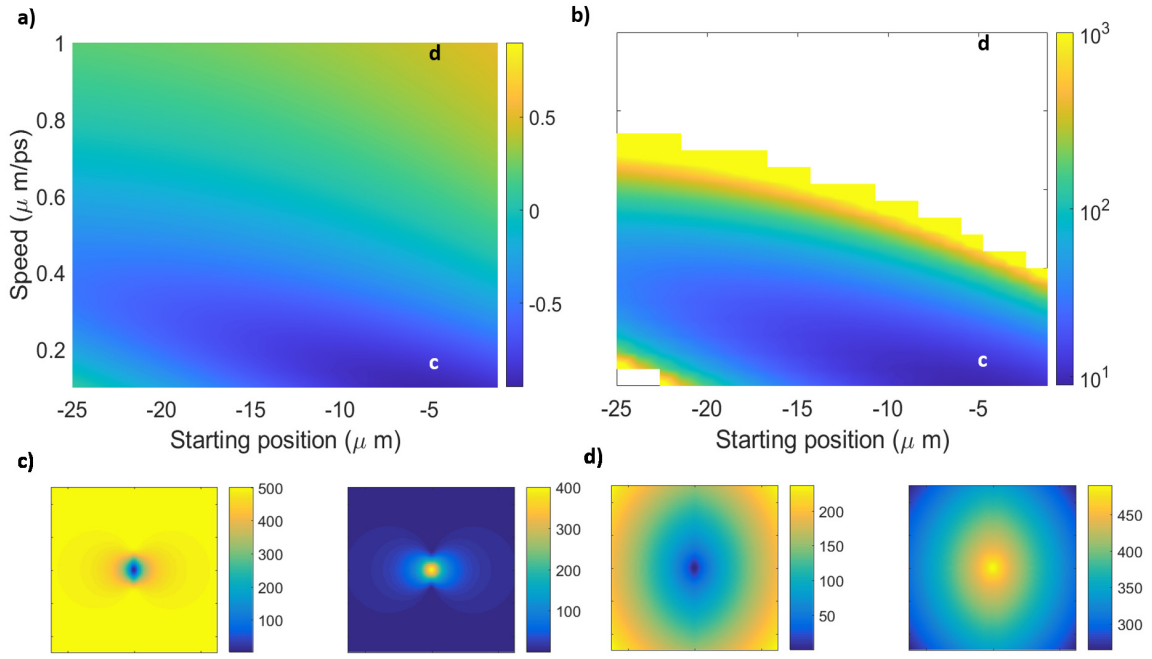

Figure 2.8: (a) depicts the calculated visibility for different positions of vortex starting position and speed for S1 from Eq.(2.31). (b) shows the corresponding calculation for photon number from Eq. (2.32), where we have ignored parameters which return positive values of visibilities. We have also limited the scale to show only photon numbers up to 1000. (c) shows the odd (left) and even (right) intensity outputs from the OAM interferometer for starting position $y = -4.7\mu$ m and speed 0.1μm/ps. (d) shows the same for $y = -4.7\mu$m and speed 0.96μm/ps. Their corresponding positions on (a) and (b) are marked. We find that for the quantities indicated in (c), the visibility calculated is -0.94 ± 0.01 and the corresponding value of $\bar{n}$ is 11 ± 1. For the quantities indicated in (d), the visibility calculated is 0.42 ± 0.01).

2.4.3.1 Vortex-antivortex pair, S2 and S3

For S2, the results are shown in Figure 2.9 for a vortex-antivortex pair with a separation 0.9 times the length of the collection area. Similar to S1, slow moving vortex-antivortex pairs starting near the center are more likely to produce negative values of visibility. However, due to the presence of two opposite topological charges, the visibility is lower for S2 than S1. As examples, for pairs starting at $y = -4.7\mu m$,

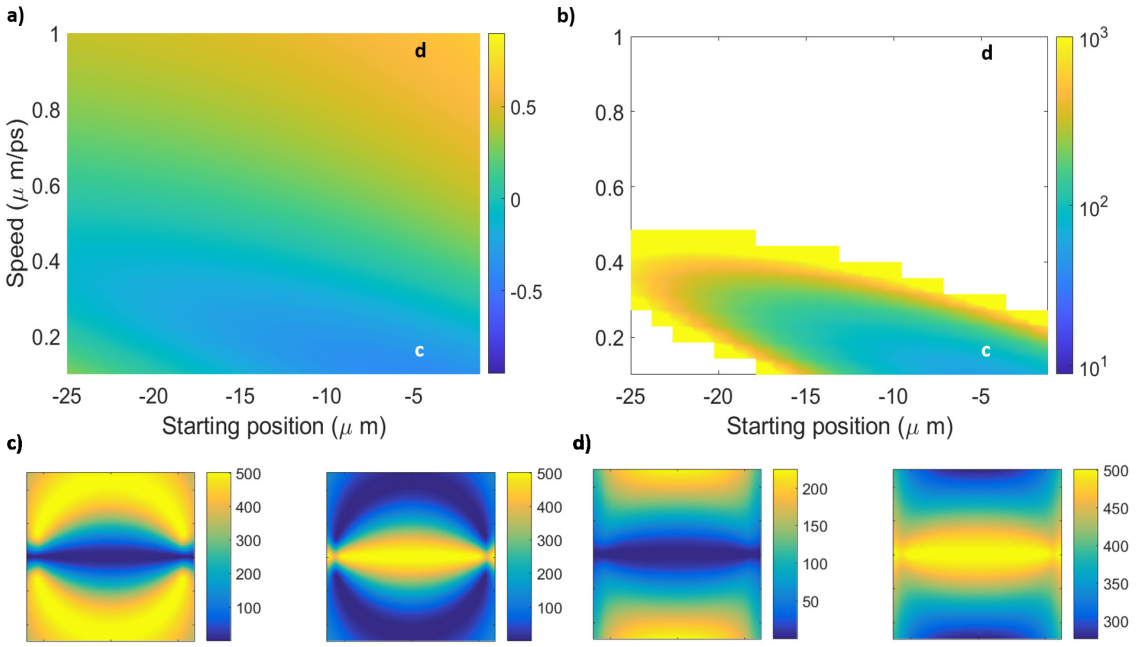

Figure 2.9: (a) depicts the calculated visibility for different values of the vortex-antivortex pair starting position and speed for S2 from Eq. (2.31). (b) shows the corresponding calculation for photon number from Eq. (2.32). (c) shows the odd (left) and even (right) intensity outputs from the OAM interferometer for starting position $y = -4.7\mu$ m and speed 0.1μm/ps. (d) shows the same for $y = -4.7\mu$m and speed 0.96μm/ps. In both cases, the vortex-antivortex separation was set at 0.9 times the collection area's length. Their corresponding positions on (a) and (b) are marked. We find that for the quantities indicated in (c), the visibility calculated is -0.40 ± 0.01 and the corresponding value of $\bar{n}$ is 55 ± 3. For the quantities indicated in (d), the visibility calculated is 0.60 ± 0.01.

and moving at a slow or fast speed of 0.1μm/ps or 0.96μm/ps, the visibility is $V = -0.40 \pm 0.01$ or 0.60 ± 0.01. For the slow moving pair, the corresponding $\bar{n} = 55 \pm 3$. The separation of 0.9 times the collection area was chosen because that was the separation which gave the most negative value of visibility. Experimentally, this can be achieved by using lenses and spatial filters. For S3, Figure 2.10 shows the visibility and the corresponding photon number for a pair recombining at an angle $\theta = -20$ degrees with a mid-point separation of 45μm. The result is qualitatively similar to that of $\theta = 0$ degrees, or S2 (Figure 2.9(a)). Slow moving vortices do not traverse

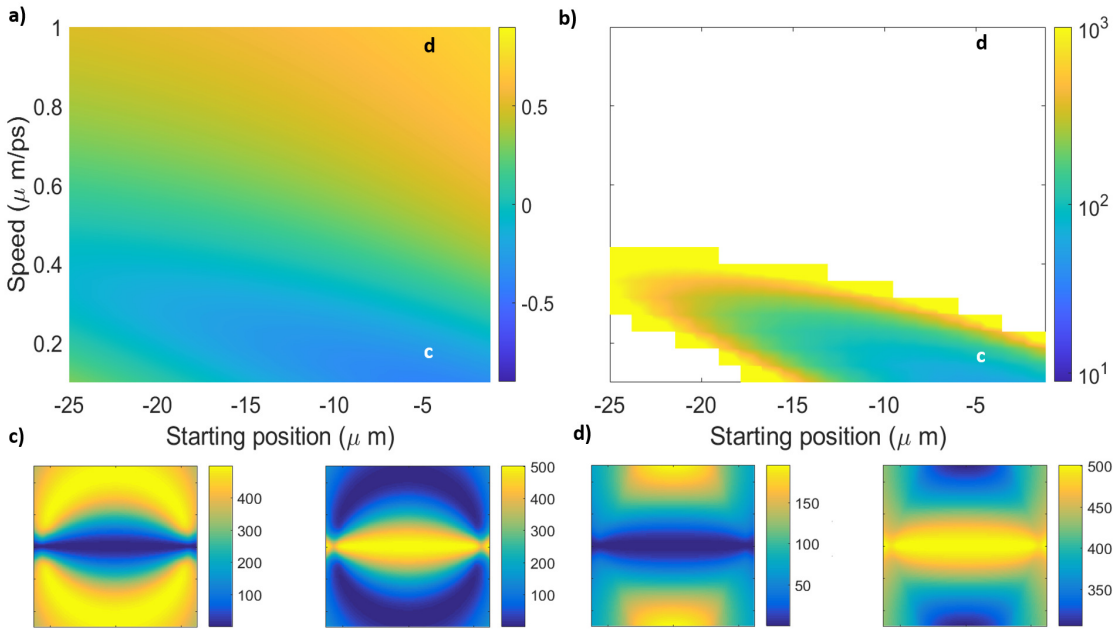

Figure 2.10: (a) depicts the calculated visibility for different values of the vortex-antivortex pair's starting position and speed for S2 from Eq. (2.31) when the pair is recombining at an angle $\theta = -20$ degrees to the vertical. (b) shows the corresponding photon number calculation from Eq. (2.32). (c) shows the odd (left) and even (right) intensity outputs from the OAM interferometer for starting position $y = -4.7\mu$ m and speed 0.1μm/ps for the recombining pair. (d) shows the same for a starting position of $y = -4.7\mu$m and a speed of 0.96μm/ps. In both cases, the pair's separation at y=0 was set at 0.9 times the collection area's length. Their corresponding positions on (a) and (b) are marked. We find that for the quantities indicated in (c), the visibility calculated is -0.40 ± 0.01 and the corresponding value of $\bar{n}$ is 56 ± 3. For the quantities indicated in (d), the visibility calculated is 0.67 ± 0.01.

much in the horizontal direction, making them very similar to S2. Stronger effects of the recombination angle on the intensity outputs can be seen for faster moving vortices. In general the visibility V increases compared to S2, and change is much larger for fast moving vortices than slow ones.

2.4.4 Effect of different vortex core radii

The intensity profile of the beam incident on the interferometer may also influence visibility calculations. A factor that would affect this intensity profile would be the

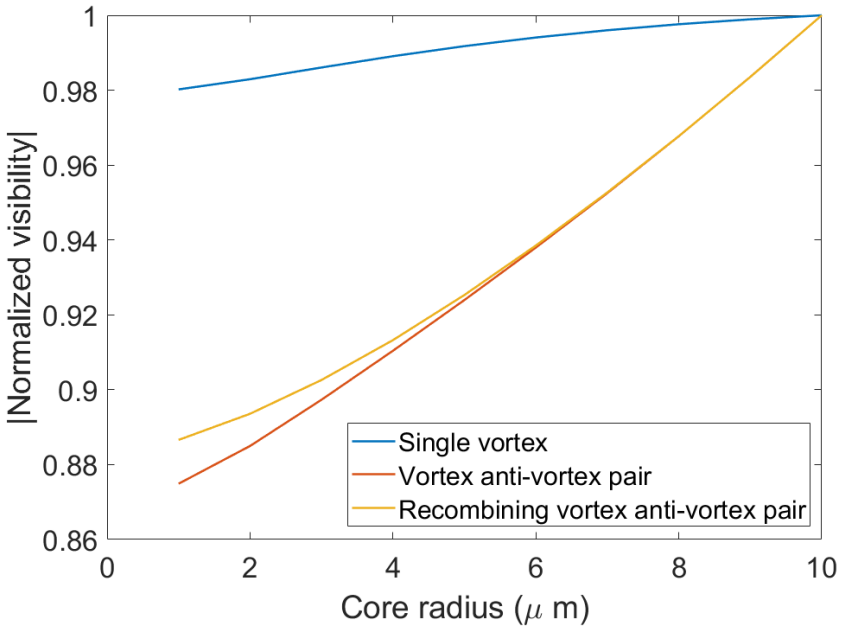

Figure 2.11: For each of the 3 scenarios, the speed and starting positions giving the most negative value of visibilities were chosen and the vortex core radii was varied from 1μm to 10μm to check its effect on the calculated value of visibility. For S3, we considered the pair recombining for $\theta = -20$ degrees. Visibility results shown here are normalized to the maximum negative value at $10\mu m$.

core radii of the vortices. In our calculations, we have assumed a vortex core radii of 1μm, which represents the order of magnitude of the healing length in polariton condensates [23]. The healing length depends on the polariton interaction strength and polariton density, which would depend on sample and experimental parameters. It would thus be instructive to examine the effects of the core radius on our calculations. For each of the three scenarios S1, S2, S3, we chose the speed and starting position that result in the most negative value of visibility and varied the radius of the vortex core. Figure 2.11 shows the result. For all 3 scenarios, the visibility is more negative as the core radius is increased. For S1, a single vortex, the change is small, only $\sim 2\%$. For the vortex-antivortex pairs, S2 and S3, the change is larger, approximately 12%. An increase in core radius would mean a decrease in total intensity, but the decrease

is unequal for the odd and even intensities, with the even intensity decreasing faster than the odd one. This would result in an increase in visibility with larger core radius for the values we are scanning.

We also confirmed that the effect of using different time step sizes and grid resolutions is insignificant. As the grid size is varied from 50 by 50 up to 500 by 500, the change in visibility is less than 0.7%. As the time step is varied from 0.05 ps to 0.5 ps, the change in visibility is less than 0.035%. As such, the effects of changing either the grid resolution or time step on calculated values of visibilities are insignificant compared to the effect of changing the vortex core radii.

2.5 Conclusion

In conclusion, we have proposed a method for the detection of spontaneously generated and randomly moving vortices in an exciton polariton condensate. We have shown that by using the OAM-sorting CoMMZI and comparing the intensities at the two outputs, it is possible detect the existence of a vortices even with as few as 10s of photons collected and when moving vortex-antivortex pairs would not have produced fork patterns in a conventional Michelson interferometer. Single shot images of exciton polariton condensates have been successfully obtained [102]. We thus believe that with our proposed set-up, the detection of spontaneous and randomly moving vortices using single shot imaging is within the realm of possibility.

CHAPTER III

Testing of the Compact Mirroring Mach-Zehnder Interferometer

The detection of orbital angular momentum (OAM) in light has been studied outside the field of polaritons for the last two decades. Many of the applications of optical vortices discussed in Chapter I, such as multiplexing requires unequivocal measurements of the OAM states in use. Such measurements make use of the unique phase property of the optical vortices, making use of tools such as interferometry [86, 87], forked diffraction gratings [103], via transformation to a transverse phase gradient [104], and mapping to cartesian coordinates [105]. Time-mapping involving a vortex phase plate and a single-mode fiber falls among the more creative yet simple methods [106].

In this chapter, I discuss the design and testing of the CoMMZI, an interferometer that can detect vortices with a low number of photons. Calculations for photon numbers were done in Chapter II. I will show how optical vortices are produced in our lab using a spatial light modulator, and how the interferometer distinguishies between a vortex-carrying beam and a non vortex-carrying beam. I will then show some experiments that were done with polariton PL and show that the interferometer can detect vortex carrying states in polaritons. I will then conclude with some considerations for single-shot experiments moving forward.

3.1 Creating optical vortices with the Spatial Light Modulator

The testing of tools for OAM detection would require the generation of pure states of OAM. Methods of producing such states use tools such as the spatial light modulator (SLM) [103], off-axis pumping [107], Q-plates [108, 109], and the Vortex phase plate (VPP) [110]. Due to its ability to produce a variety of transverse phase profiles, the SLM was our equipment of choice. A SLM comprises of a liquid crystal screen with individual pixels controlled via an electric input. Upon the application of voltage, the liquid crystals in each pixel are rotated and the index of refraction of that pixel is changed. Since each pixel has an independent voltage control, the index of refraction across the liquid crystal screen could vary based on the desired transverse phase output. This is illustrated in Figure 3.1

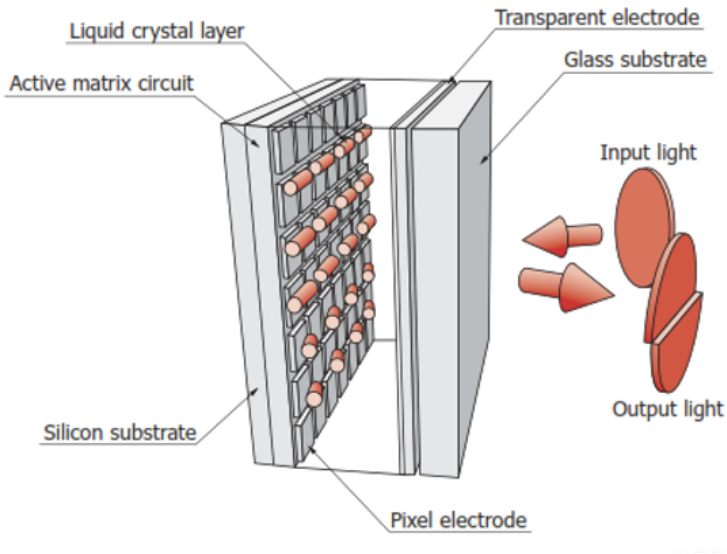

Figure 3.1: The operation of a spatial light modulator, taken from the manual by Hamamatsu.The liquid crystal molecules in each pixel are subjected to applied voltages which depend on user-input. This produces a transverse refractive index variation which modulates the transverse phase in the output light.

Our SLM is a Holoeye PLUTO Phase-only modulator with pixel dimensions 1920

by 1080. Each pixel is 8 μm square and has a fill factor of 93 %. This means 93 % of the pixel area is active. Thus, not all light incident on the SLM will be modulated, and this issue will be discussed in Section 3.1.4.

3.1.1 Computer Generated Holograms

The variation in refractive index across the SLM's screen is determined by Computer Generated Holograms (CGHs). A CGH is a grayscale image of a phase profile that for which the gray value of each pixel determines the voltage applied to the corresponding pixel in the SLM. Users can use built-in CGHs or they can create one using Matlab. It is possible to generate any image in the far-field using a Fourier Transform of the original image as the CGH. For this work, we will focus on the creation of various vortex configurations.

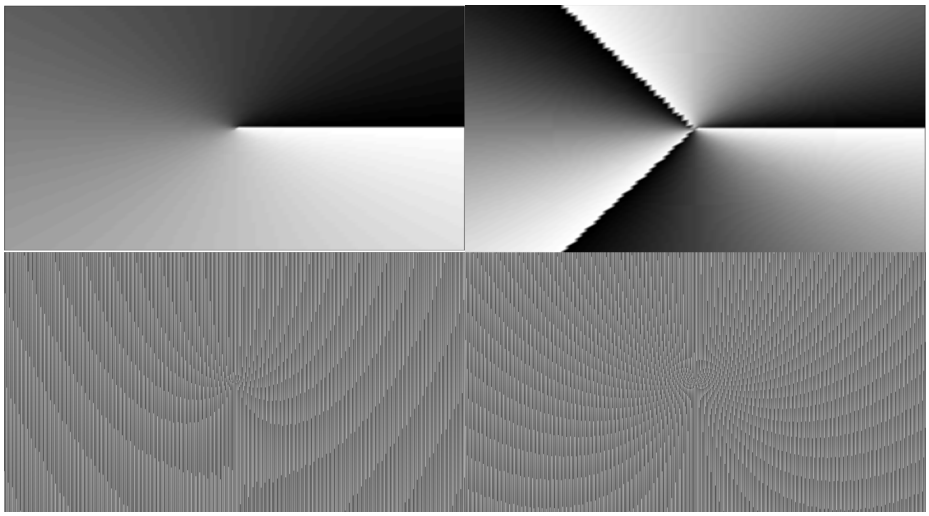

Figure 3.2: Computer Generated Holograms (CGHs) for producing a vortex beam of charge l=1 (left) and l=3 (right). The top row shows the CGHs when the SLM is used in Vortex Phase Plate mode, in which both the incident and the zeroth order reflected beams are normally incident on the SLM screen. The bottom row shows a blazed phase grating superimposed on the CGHs shown in the top row. The blazed phase grating directs intensity into the first diffraction order.

Figure 3.2 shows the CGHs used to create vortices with l=1 (left) and l=3 (right).

The CGH uses grayscale values from 0 to 255, with darker areas indicating less voltage applied. The top 2 CGHs are for configurations used in Vortex Phase Plate (VPP) mode, in which the incident and reflected beams are collinear with respect to each other. The bottom 2 CGHs show the same phase but superimposed with a blazed grating phase. This allows for a large portion of the intensity to be directed into the first diffraction order, thereby reducing the amount of unmodulated beam intensity in the beam to be investigated. This issue will be further explored in Section 3.1.4

We have also performed testing with off-centered vortex beams and vortex and anti-vortex pairs. The CGHs used to generate such configurations can be found in Appendix A.2.

3.1.2 Vortices generated with the Spatial Light Modulator

To create the vortex profiles shown in this section, we used a Gaussian beam of wavelength 633nm and waist 2mm, produced by a HeNe laser and coupled to the testing set-up via single-mode fiber. A Glan-Thompson polarizer was used to linearly polarize the beam in a direction parallel to the long axis of the SLM screen after its exit from the single-mode fiber.

The CGHs shown in Figure 3.2 only allow for phase modulation of the incident beam. As such, the resulting vortices will be superpositions of multiple p states. This can be seen in Figure 3.3, where the central vortex core is shown together with nodes in the radial direction. Since the CoMMZI only sorts odd and even values of l, this is not expected to have a large impact on its efficacy.

Figure 3.4 shows an example of a vortex-antivortex pair generated with a CGH. Such configurations represent the expected type of vortices seen in a system with a net zero orbital angular momentum, with the vortex having a value of l=1 and the antivortex having a value of l=-1. Each vortex center was displaced 0.8 mm along the horizontal profile of the SLM's screen. In the figure, the vortex-antivortex cores

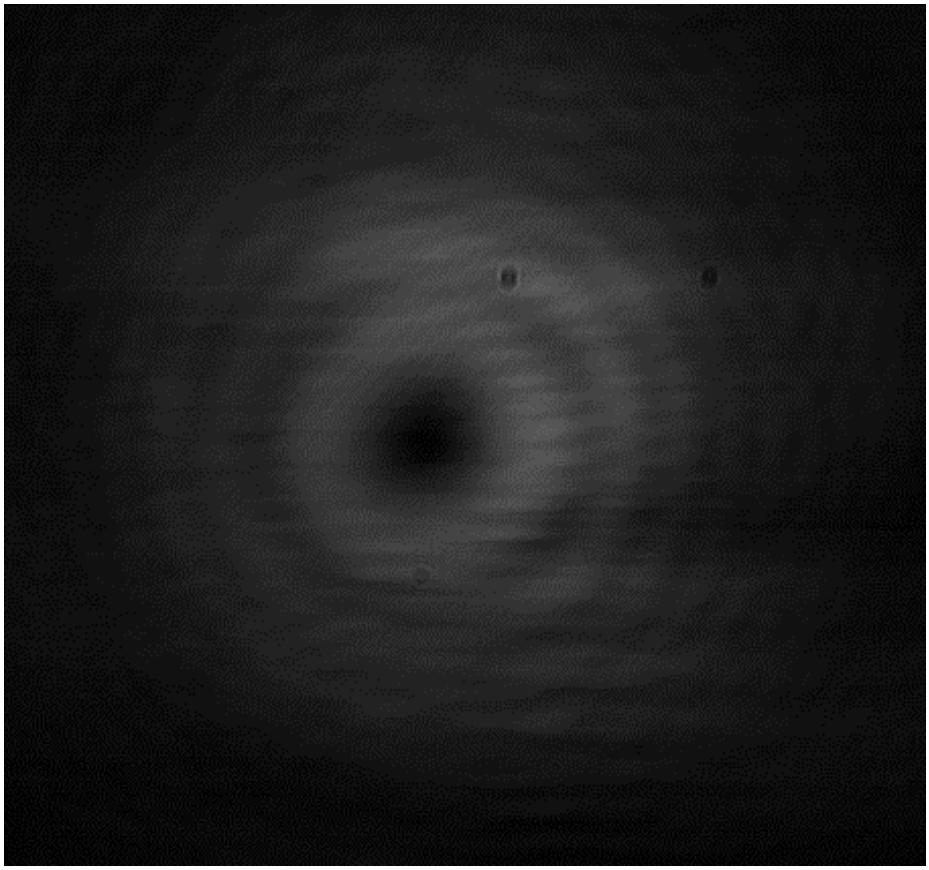

Figure 3.3: An image of a beam with topological charge l=1. The beam is a superposition of p states, which explains the pattern of concentric rings around the central vortex core.

shows an elongated profile and a displacement towards the bottom of the beam. This is a result of the mutual interaction of the phase gradients of the two vortices [111], and it becomes more pronounced the farther the beam propagates. It is evident that the up-down inversion in the CoMMZI will not result in the most effective overlap of the beam's profile.

Figure 3.4 was taken at approximately 1/10 the Rayleigh range of the original Gaussian beam. To maintain as consistent a transverse profile as possible, the beam could be magnified since the Rayleigh range scales with the square of the beam width. For most SLM applications, magnifying the beam to fill the entirety of the screen is recommended to allow for a more uniform beam intensity. This is especially important

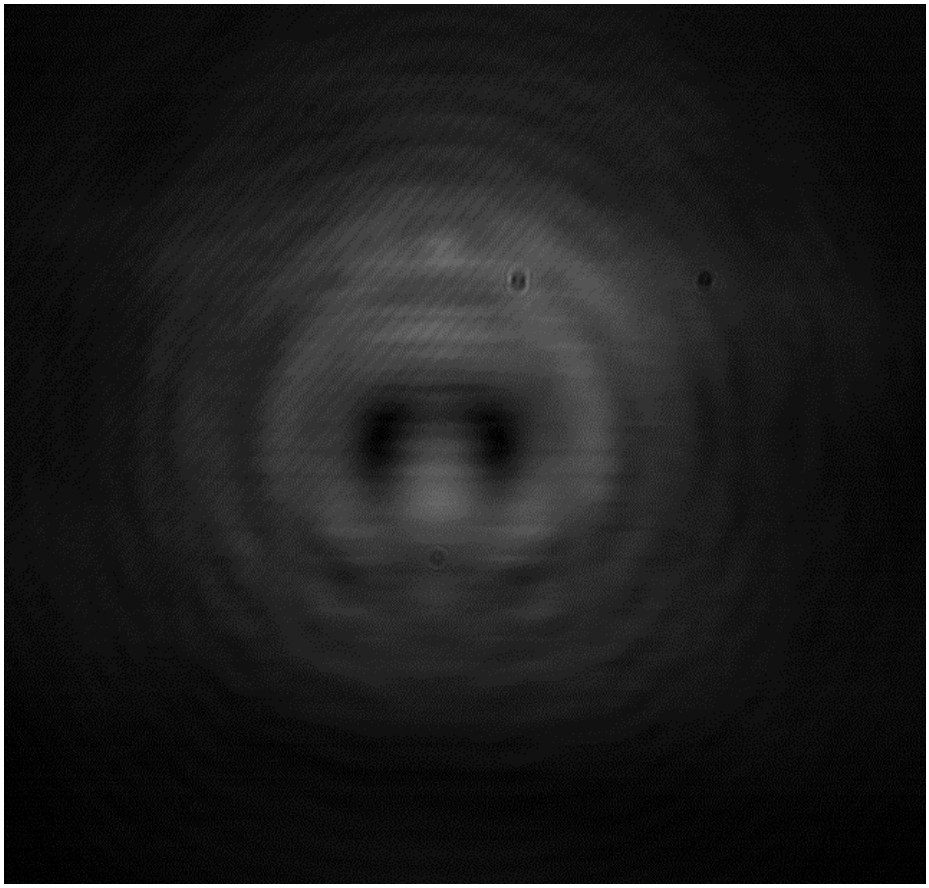

Figure 3.4: An image of a beam with a vortex-antivortex pair, with each vortex core displaced 0.8mm along the horizontal profile of the SLM screen. The elongation and downward displacement of the vortex-antivortex pair is a result of the mutual phase gradient of the vortices.

if intensity modulation is desired. This topic will be covered in the Section 3.1.5.

3.1.3 Phase extraction with the Fringe Demodulation Method

Accurately determining the efficacy of the CoMMZI depends on the controlled production of vortex beams. The appearance of a vortex core alone is not sufficient to determine vorticity. The phase of the beam needs to be examined to ensure that a helical phase is present, and that what is being sorted is indeed a vortex beam with a well-defined orbital angular momentum.

To do this, we use a fringe demodulation method to extract phase information from

interference patterns formed with the phase-modulated beam and an unmodulated component. This can be achieved through the use of Mach-Zehnder interferometer set-up, with the SLM acting as one of the mirrors. This set-up is shown in Figure 3.5. The beam is first split into two components at the first beam splitter. One component is sent directly to the second beam splitter while the other is sent to the SLM. The modulated first-diffraction order is then sent through an iris to filter out the unwanted diffraction orders. Interference between the modulated beam and the unmodulated beam is then observed in a camera. The inset of Figure 3.5 shows an example of an interference pattern for a l=1 beam. The characteristic fork fringe pattern of optical vortices is highlighted for clarity.

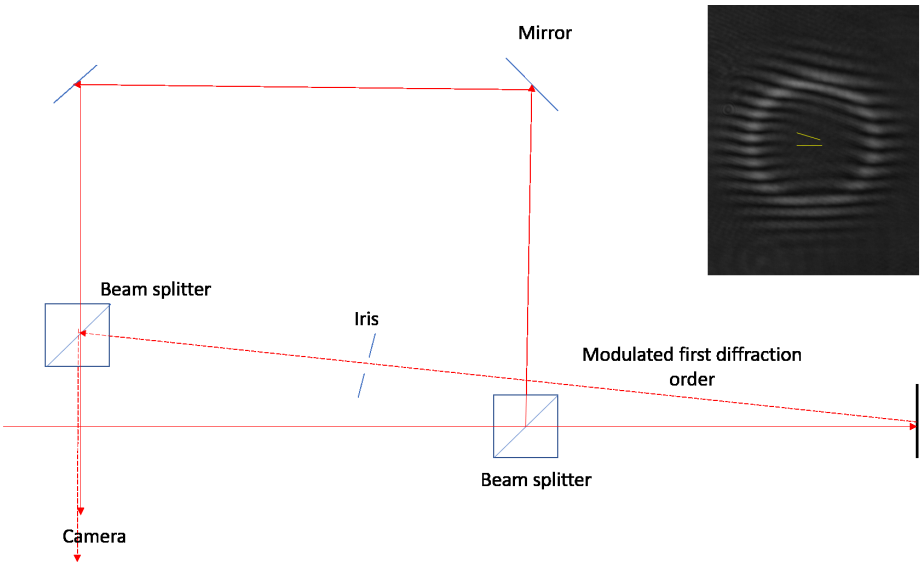

Figure 3.5: Set-up used to create and interferometrically test vortices generated by the SLM. The set-up is not drawn to exact scale and the beamsplitter closest to the camera is at a slight angle to the beam path, to allow for both beams to be collinear. The inset shows the interference pattern formed by a p=1, l=1 beam and an expanded flat-phase beam. The characteristic fork-shaped fringe is highlighted in yellow.

A fork fringe pattern is usually a sufficient indication of optical vortices, but one may be interested in extracting the phase profile of the modulated beam for further confirmation. To extract amplitude and phase information from the fringe patterns,

we can use a fringe demodulation method, shown in Figure 3.6 for a p=0, l=1 beam interfering with a Gaussian beam. For two monochromatic fields interfering with each other in the y-direction, the interference pattern (Figure 3.6**a**) can be written as

$$\begin{aligned}|E_1(x,y)+E_2(x,y)|^2 = E_1(x,y)^*E_1(x,y) + E_2(x,y)^*E_2(x,y)+ \\ E_1(x,y)^*E_2(x,y)\exp(i\phi_2(x,y)-i\phi_1(x,y))\exp(i2k_y y)+ \\ E_2(x,y)^*E_1(x,y)\exp(i\phi_1(x,y)-i\phi_2(x,y))\exp(-i2k_y y), \quad (3.1)\end{aligned}$$

where $\phi_1(x,y)$ and $\phi_2(x,y)$ are the phase of the two beams and $E_1(x,y)$ and $E_2(x,y)$ are the electric fields. k_y is the wavenumber in the y-direction. The spatial Fourier transform of Equation 3.1 can be divided into 3 components (Figure 3.6**b**), given as

$$\begin{aligned}\mathcal{F}(|E_1(x,y)+E_2(x,y)|^2) = \mathcal{F}(E_1(x,y)^*E_1(x,y) + E_2(x,y)^*E_2(x,y))+ \\ \mathcal{F}(E_1(x,y)^*E_2(x,y)\exp(i\phi_2(x,y)-i\phi_1(x,y))\exp(i2k_y y))+ \\ \mathcal{F}(E_2(x,y)^*E_1(x,y)\exp(i\phi_1(x,y)-i\phi_2(x,y))\exp(-i2k_y y)), \quad (3.2)\end{aligned}$$

One can then eliminate the zeroth order term and one of the first order terms by superimposing an appropriate filter (Figure 3.6**c**) . An inverse Fourier transform can then be performed on the remaining first order term to obtain both intensity information $E_1(x,y)^*E_2(x,y)$ and phase information $\exp(i\phi_2 - i\phi_1)\exp(i2k_y y)$ (Figure 3.6**d** and **e** respectively) A phase shift can then be introduced to the phase term to eliminate the tilt term and obtain information on the phase difference between the two interfering beams. This can be given by the equation

$$\psi(x,y) = \mathcal{F}^{-1}[\mathcal{F}(E_1(x,y)^* E_2(x,y)\exp(i\phi_2(x,y) - i\phi_1(x,y))\exp(i2k_y y))]\exp(-i2k_y y). \tag{3.3}$$

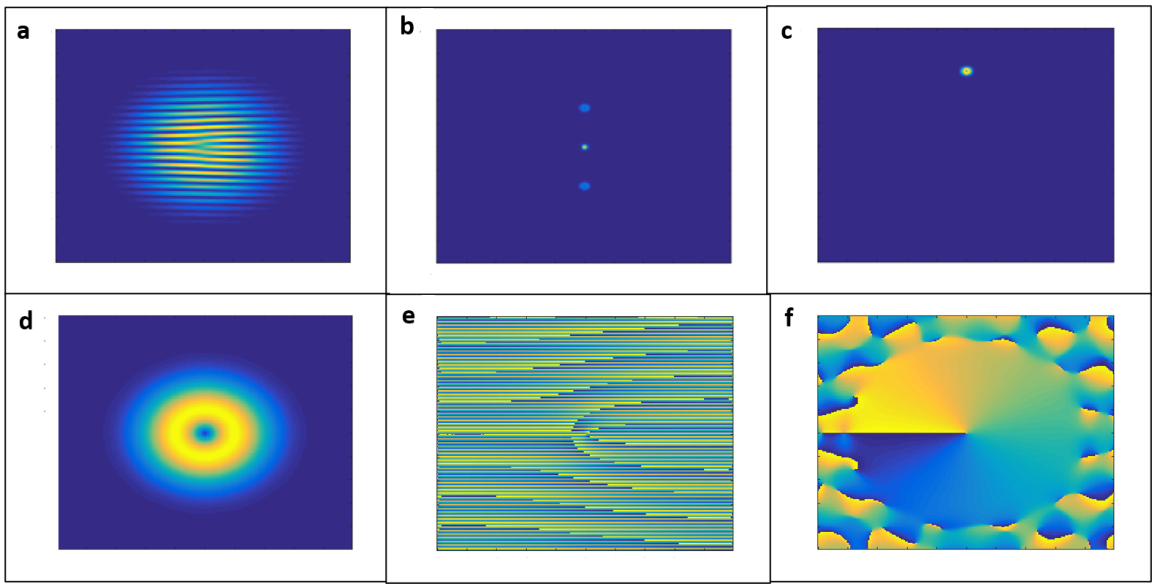

Figure 3.6: The process by which the phase profile of a beam modulated by the SLM is extracted. **a** shows the simulated interference pattern of a Gaussian beam and a l=1 beam. **b** shows the Fourier transform of the interference pattern. In **c**. a Gaussian window is applied on one of the first-order terms. **d** shows the intensity profile of the Inverse Fourier Transform of **c**, while **e** shows its phase profile. A phase tilt term is applied to **e** to obtain the result shown in **f**.

In the example shown in Figure 3.6, the phase difference between the two beams is just the phase of the vortex beam itself. The phase dislocation lines seen on the edges of the phase profile in **f** is due to higher spatial momentum states introduced through the use of the filter needed to isolate the first order term. These have already been reduced by the use of a smoother window. Since phase is our main focus in this method, a Gaussian window has been used as a filter instead of a circular one.

We have tested this method for different values of l using fringe patterns from the set-up shown in Figure 3.5. Figure 3.7 shows the extracted amplitude and phase

information of a l=1 beam. The original profile is shown on the bottom left. The phase dislocation line in the phase profile is curved, indicative of the helical phase at nonzero values of propagation distance z. The amplitude profile also shows the accurate location of the vortex core.

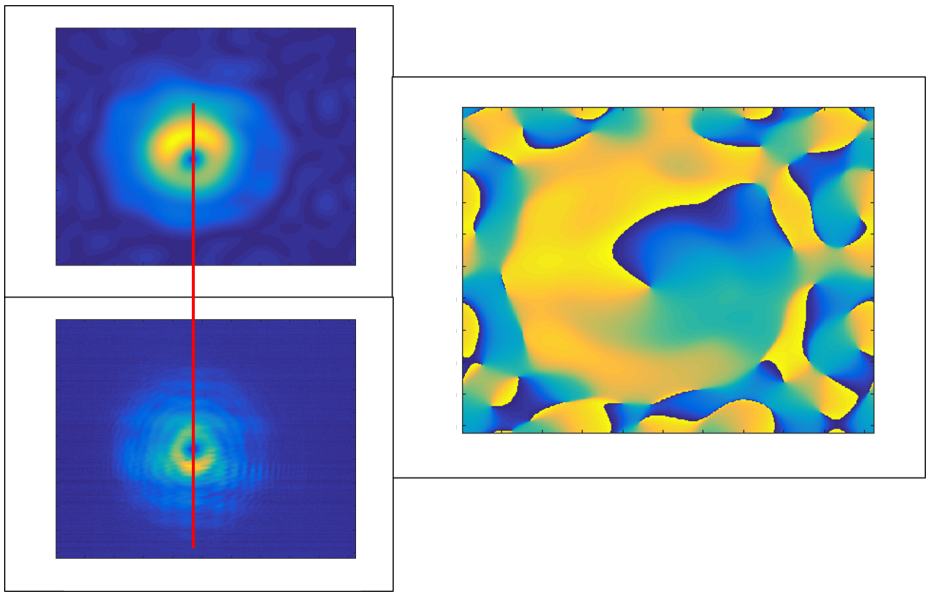

Figure 3.7: The extracted intensity profile for a l=1 beam using the Fringe Demodulation method (top left) and the resulting phase profile (right). The original beam is shown in the bottom left. The intensity profile is a product of the interfering Gaussian beam and the l=1 beam, hence the discrepancy between the extracted and original intensity profiles.

I have thus shown that extraction of the phase profile of the beam is possible. Examples for l=2 and l=0 beams is shown in Appendix A.2.

3.1.4 Corrections in phase modulation

In this section, I will present efforts to correct for errors in the phase modulation process. These errors arise from inaccurate SLM voltages for the wavelength in use, and residual unmodulated components of the original beam.

The index of refraction for each pixel on the SLM screen depends on the wavelength of light incident on it. The SLM software comes with lookup tables for certain

wavelengths, so it may be necessary to fine-tune the voltage applied to each pixel if one were to use a non-listed wavelength. The process by which this is achieved is known as Gamma correction. Similar to the analagous process used in photography, gamma correction alters the shape of the graph of voltage output with gray levels of each pixel. The SLM software comes with controlled gamma correction capabilities, and one just has to move a slider to adjust gamma values. The fringe pattern formed from a Gaussian beam and vortex-carrying beam serves as good feedback for gamma correction. In Figure 3.8, examples of fringe patterns at different values of gamma are shown. The wavelength used for this test was 785nm while the lookup table had values for 750nm. As the value of gamma changes, the fork pattern's symmetry is also altered. The experimenter should change the value of gamma until the fork pattern is as symmetric as possible.

In Figure 3.5, the first diffraction order from the SLM was used. As mentioned in Section 3.1, each pixel of the SLM screen only has a 93% fill factor. As such, the zeroth order component would have unmodulated intensity. An example of this is shown in Figure 3.9. The bright spot near the center of the logo is a result of this unmodulated component. To avoid this component, a blazed grating phase can be superimposed on the original CGH to direct the beam's intensity into the first diffraction order.

The effect of this unmodulated component on vortices is especially significant. Figure 3.10 shows a comparison of a l=2 beam produced in the first diffraction order (left) and the zeroth order (right). The fringe pattern of the beam produced in the first diffraction order shows a three-pronged fork pattern joined at its center. The presence of the unmodulated component in the zeroth order results in the l=2 vortex splitting into two l=1 vortices, thus showing 2 individual fork patterns in the fringes. The intensity profile of the zeroth order beam also shows 2 vortex cores, as opposed to one larger one for the first diffraction order. This phenomenon is explained by the

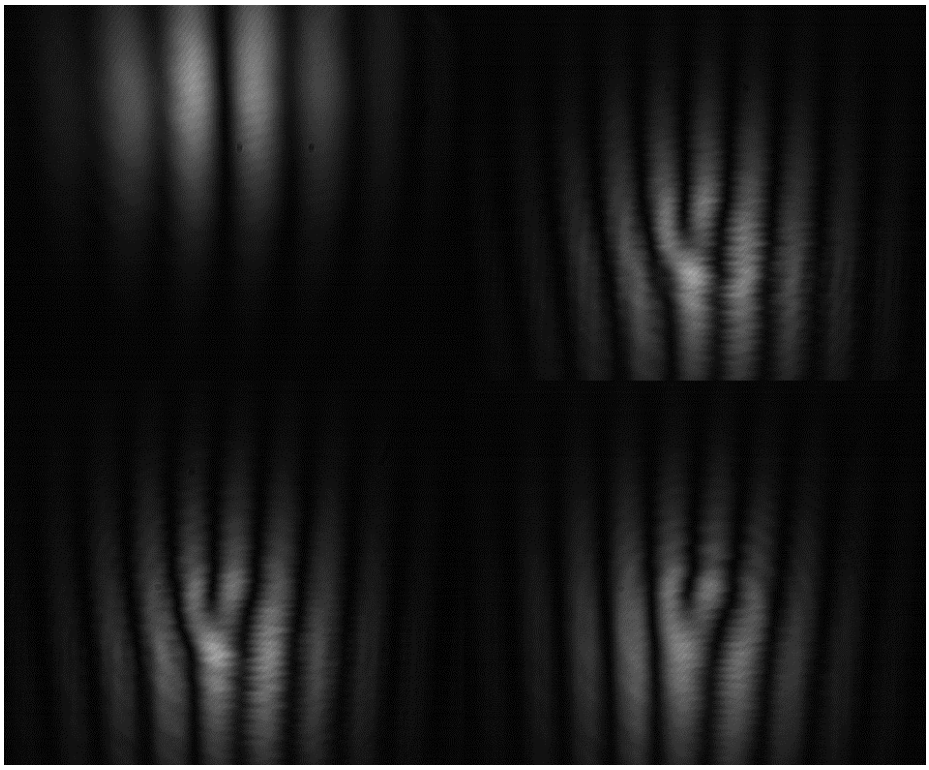

Figure 3.8: Fringes formed by an interference between a Gaussian beam and a l=1 beam at different values of gamma correction, using a wavelength of 785nm and a Lookup table value of 750nm. The top left image shows the fringe pattern without a vortex phase. At the ideal gamma value, the fork pattern should be symmetrical.

change in the shape of zero contours of the real component of the beam's transverse profile due to an additional real component [112]. The intersection of the zero contours from both the real and imaginary parts is no longer at the center, where the core of the pure vortex beam would have been positioned. For the l=2 beam, two new intersection points would form the cores of the individual l=1 vortices.

3.1.5 Intensity modulation with a Phase-only Spatial Light Modulator

While the primary quantity of interest in CoMMZI efficacy is the phase, other factors such as amplitude may play an important role as well, as seen with the case of a propagating vortex-antivortex pair. In addition, the size of the beam's transverse profile also depends on the value of l and the distance of propagation, with larger l

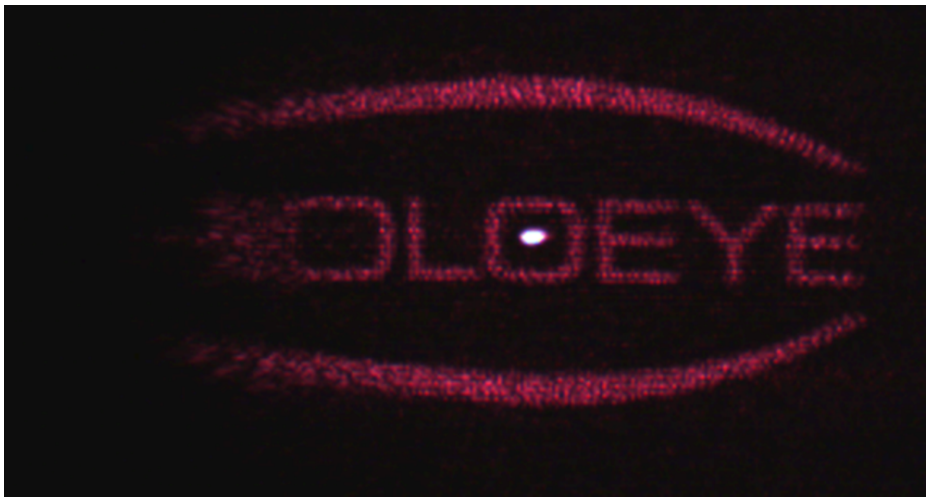

Figure 3.9: The Holoeye logo produced using the zeroth-order reflected beam from a SLM programmed with a CGH coded with the Fourier transform of the image. The bright spot at the center is the unmodulated component of the reflected beam and demonstrates the disadvantages of using the zeroth-order signal.

values corresponding to faster divergence [113]. This would be an issue for the limited cross section of the CoMMZI, and can be mitigated by forcing the beam to adopt a single p value. It thus may be useful to test the CoMMZI using vortices accompanied by different intensity profiles.

Despite being a phase-only SLM, the PLUTO is capable of performing intensity modulation on the transverse profile of the beam. This is done through the use of an amplitude mask designed to recreate the desired intensity profile in the first diffraction order. This mask is superimposed on top of the phase portion of the CGH. The phase portion of the CGH would already have a blazed grating phase superimposed on it, and the intensity profile of the mask would determine the gradient of the blazed grating. As seen in Figure 3.11, a steeper gradient would direct more intensity into the first diffraction order, while the remaining unmodulated intensity is sent to the zeroth order instead. During our tests, we have found that using a mask which simply follows the amplitude profile of a p state was sufficient to create an intensity profile that resembles what we would expect from a pure p state. However, it is still

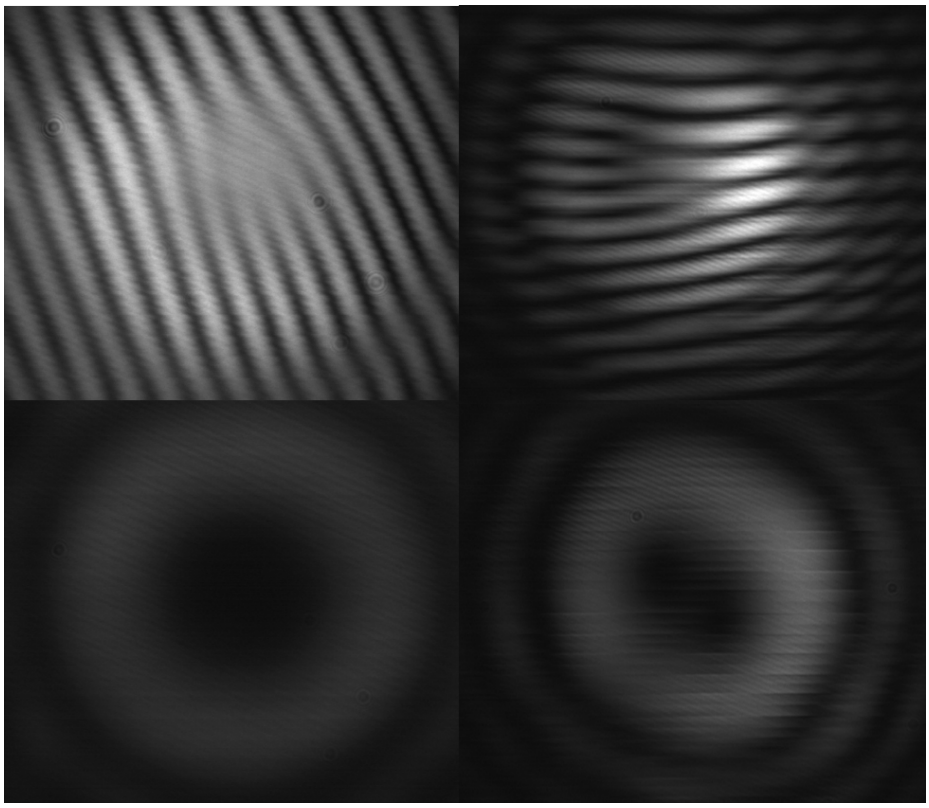

Figure 3.10: The interference fringes (top) of a vortex beam with l=2 when generated using a blazed grating to direct the intensity into the first diffraction order (left), and when generated in Vortex Phase Plate mode and using the zeroth order reflected beam.

important to discuss the formal method for creating a mask that would allow one to recreate any desired intensity profile in the far-field.

We let the desired complex field be expressed as

$$s(x, y) = a(x, y) \exp(i\phi(x, y)), \tag{3.4}$$

where a(x,y) is the desired amplitude and $\phi(x, y)$ is the phase. The transmittance of the CGH used to create this field is given as

$$h(x, y) = \exp(i\psi(a(x, y), \phi(x, y))), \tag{3.5}$$

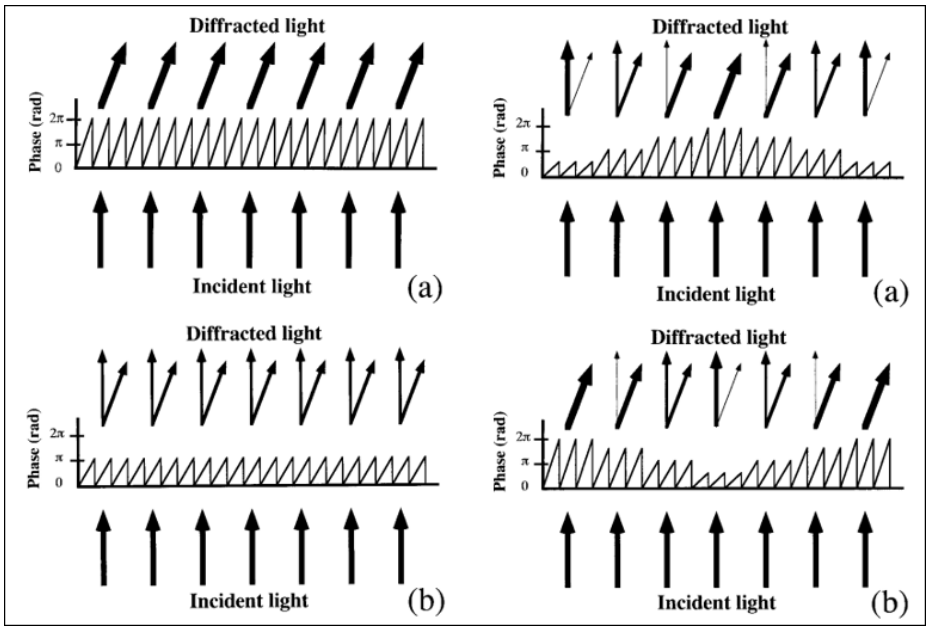

Figure 3.11: How a phase-only SLM can be used for amplitude modulation. The height and gradient of the blazed grating on each pixel is varied depending on the desired intensity profile of the first diffraction order. Taken from Davis et al [114].

where the phase-only CGH is represented as ψ. To understand how the encoded phase and amplitude information would look in the far-field, it would be useful to break down the transmittance into its Fourier components, such that

$$h(x,y) = \sum_{q=-\infty}^{\infty} h_q(x,y), \tag{3.6}$$

where q is the diffraction order, and

$$h_q(x,y) = c_q^q \exp(iq\phi), \tag{3.7}$$

where

$$c_q^a = (2\pi)^{-1} \int_{-\pi}^{\pi} \exp(i\psi(\phi,a)) \exp(-iq\phi) d\phi, \tag{3.8}$$

where the explicit dependence of a and ϕ is not shown.

Several methods of writing the CGH $\psi(\phi, a)$ exist. For our tests, we chose to use the method found in [114] and [115], which takes $\psi(\phi, a)$ to be

$$\psi(\phi, a) = f(a)\phi, \tag{3.9}$$

where f(a) represents the form of the amplitude mask which encodes information about the amplitude a(x,y). From Equation 3.8, the 1st order coefficient is given as

$$c_1^a = sinc(1 - f(a)), \tag{3.10}$$

and equating the first-order coefficient with the desired amplitude, we will get the relation

$$a = sinc(1 - f(a)). \tag{3.11}$$

f(a) can then be solved via numerical methods and be used as the amplitude profile of the CGH mask.

In attempting to solve for f(a), we have found that it to be very resource intensive. As such, we decided to use unaltered amplitude masks and compare the resulting profile with the expected ones.

The set-up we use for testing is shown in Figure 3.12. The beam from the fiber is first expanded with a telescope set-up such that its transverse profile fills the entirety of the SLM's screen. After incidence, the first-diffraction order from the SLM is sent into a second identical telescope set-up with an iris at the focal point of the two lenses. This iris serves as a filter for eliminating higher values of transverse momentum k. The filtered and shrunk beam is then sent into a camera. The bottom of Figure 3.12 shows the camera image when the expanded zeroth order and the first order were captured together. The high-k filtering thus also serves to block out the unwanted zeroth order.

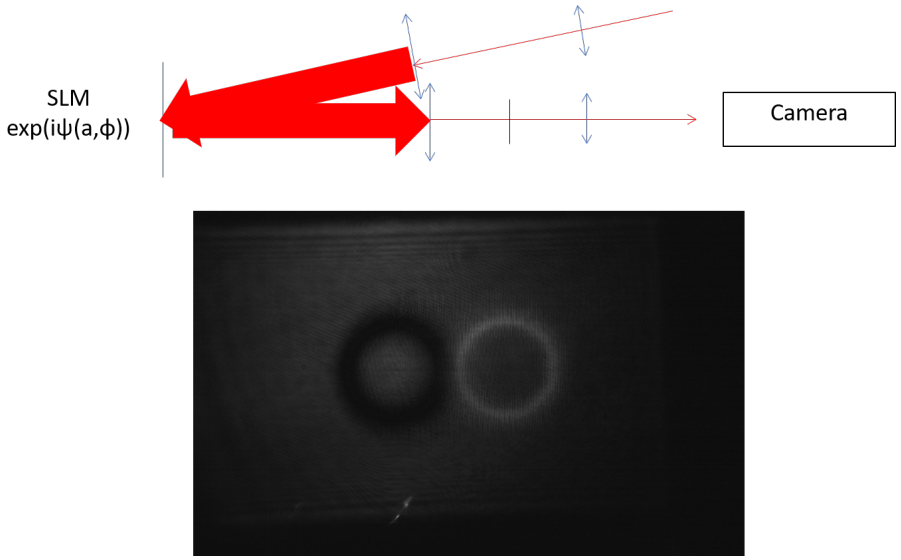

Figure 3.12: The set-up used to perform amplitude modulation testing. The beam was expanded using a telescope set-up such that its transverse profile fills the SLM screen. The first diffraction order was passed through an identical telescope set-up to shrink the beam. An iris was placed at the focal point of the two lenses in the latter telescope for filtering out high-k values and smoothen the signal. The image shown at the bottom shows both the unmodulated zeroth order and the modulated first order captured by the camera. The iris was opened to capture this image.

We have performed amplitude modulation tests with an expanded beam on a Gaussian mask on the SLM. In those tests, we found that the resulting intensity profile resembled the expected ones. Any difference in quality is likely attributed to the use of high-k filtering. Using unaltered amplitude masks (Figure 3.13), we were able to create far-field intensity profiles of l=3 states with 3 different values of p, as shown in Figure 3.14. This is not a surprising result since analysis by [114] has shown that using a simple product of a(x,y) and $\phi(x, y)$ as the CGH creates an approximate reproduction of the desired intensity and phase profile. Any distortion caused by the *sinc* function was not obvious in our result.

Asymmetry in the profiles is likely due to errors in high-k filtering or irregularities in the profile of the output from the fiber. Since the exact profile of the PL from a single realization of a polariton condensate could be rather irregular, we decided

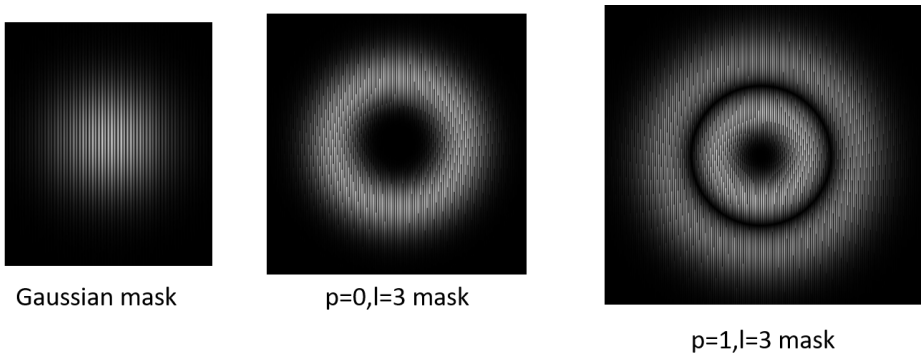

Figure 3.13: Amplitude masks superimposed on top of blazed phase gratings for the purposes of amplitude modulation.

to turn our attention to the more important aspect of the CoMMZI's function, the phase of the SLM output. Re-creation of the PL's output can be attempted once its shape has been determined.

3.2 Testing the CoMMZI with lasers

Initial testing with the CoMMZI made use of 2 lasers, a HeNe laser with 633nm output wavelength and a diode laser with 785nm output wavelength. The 785nm laser was used because that wavelength is closer to the expected wavelength of the polariton PL. The set-up we used was similar to the one shown in Figure 3.12, with the camera replaced with two mirrors guiding the beam into the CoMMZI.

The large prism of the CoMMZI was placed on a piezo-controlled stage. During testing, a sinusoidal signal was sent to the piezo to vary its length. The output from each port of the CoMMZI was directed into a photodetector, from which the voltage output was read on an oscilloscope. An example of an output from one of the photodetectors is shown in Figure 3.15. The output voltage depends on the path difference between both beams in the CoMMZI, with a larger output indicating constructive interference occuring at the port. The two mirrors were then fine-tuned such that the visibility, given as

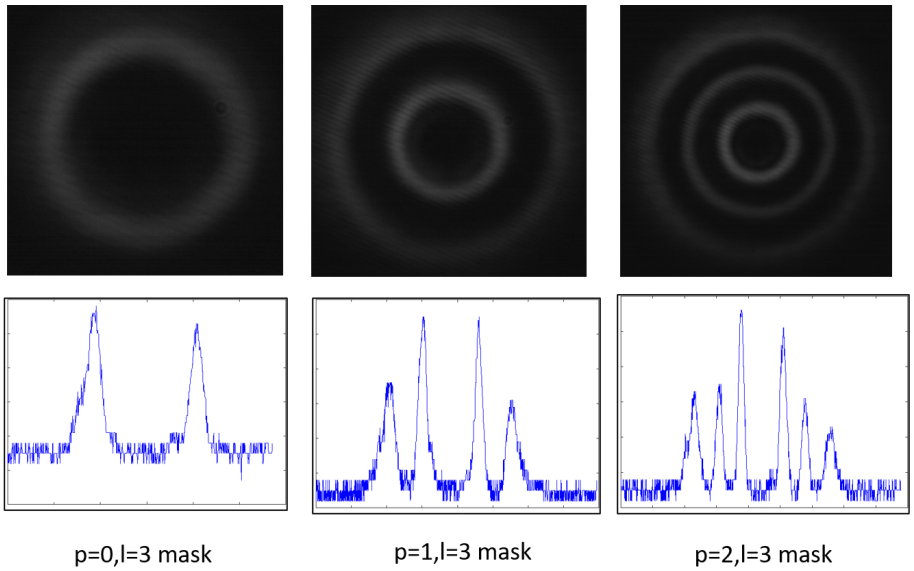

Figure 3.14: The transverse intensity profile of beams produced by different amplitude masks and phase gratings.

$$V = \frac{V_{max} - V_{min}}{V_{max} + V_{min}}, \tag{3.12}$$

was maximized.

We have found that using beams with larger values of l showed greater sensitivity to changes in alignment, due to the greater phase variation on the transverse profile of the beam. For best results, a beam of l=1 was used for the alignment.

Figure 3.16 shows the output of the CoMMZI for a Gaussian beam (top) and a l=1 beam (bottom). The output of the even port is shown on the left while the output of the odd port is shown on the right. The position of the large prism was adjusted such that constructive interference occurred at the even port for the Gaussian beam. As can be seen from the figure, the profiles of the even/odd output are what one would expect for a Gaussian/l=1 beam.

In a real polariton experiment, we do not expect spontaneous vortices to form near the center of the beam. We thus also performed testing for vortex and antivortex pair configurations, as well as off-centered vortices. Figure 3.17 shows the output for two

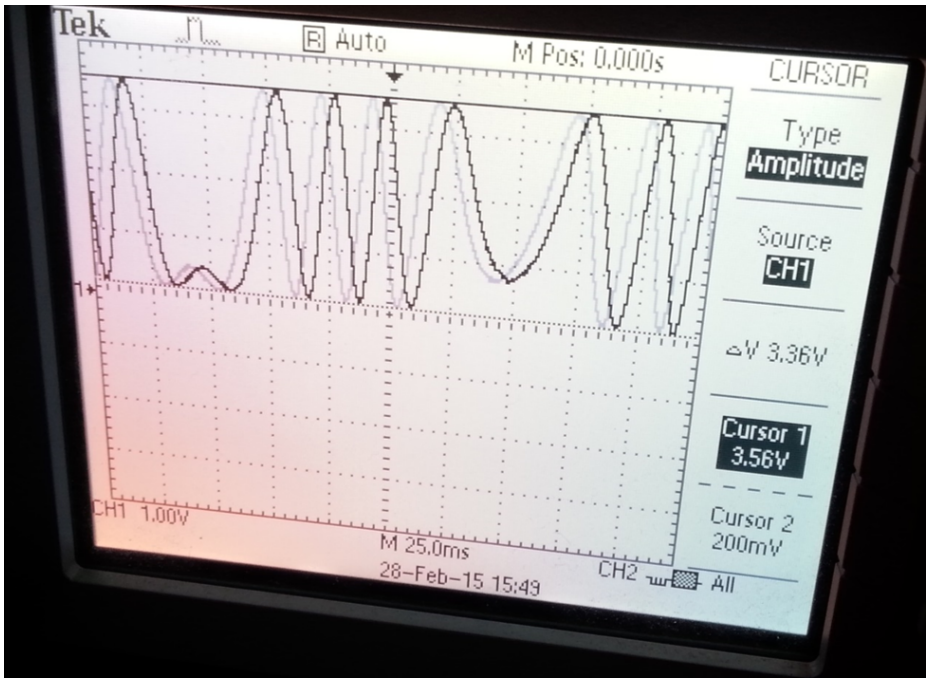

Figure 3.15: Voltage signal used to perform measurements of the CoMMZI's visibility. The voltage is read in a photodetector placed at one port of the CoMMZI's output. The variation in the signal was a result of using a piezoelectric device of which the length is sinusoidally varied in time.

configurations of vortex-antivortex pairs. The top two images show the even (left) and odd (right) outputs for a beam with a vortex and anti-vortex spaced 0.32 mm apart, while the bottom two images show the outputs for a vortex-antivortex pair spaced 0.8 mm apart. The intensity in both outputs are approximately equal, thus making this scenario close to what one would expect from a beam profile with a random phase.

Table 3.2 shows measured and expected visibility values for beams holding off-centered vortices of l=1. The vortices were displaced upward and downward for each value of displacement from center, and the measured value of visibility is the average of both measurements. The expected value of visibility was calculated using numerical simulations, in which the inversion of the beam within the CoMMZI was mimicked and a value of z=0 was assumed.

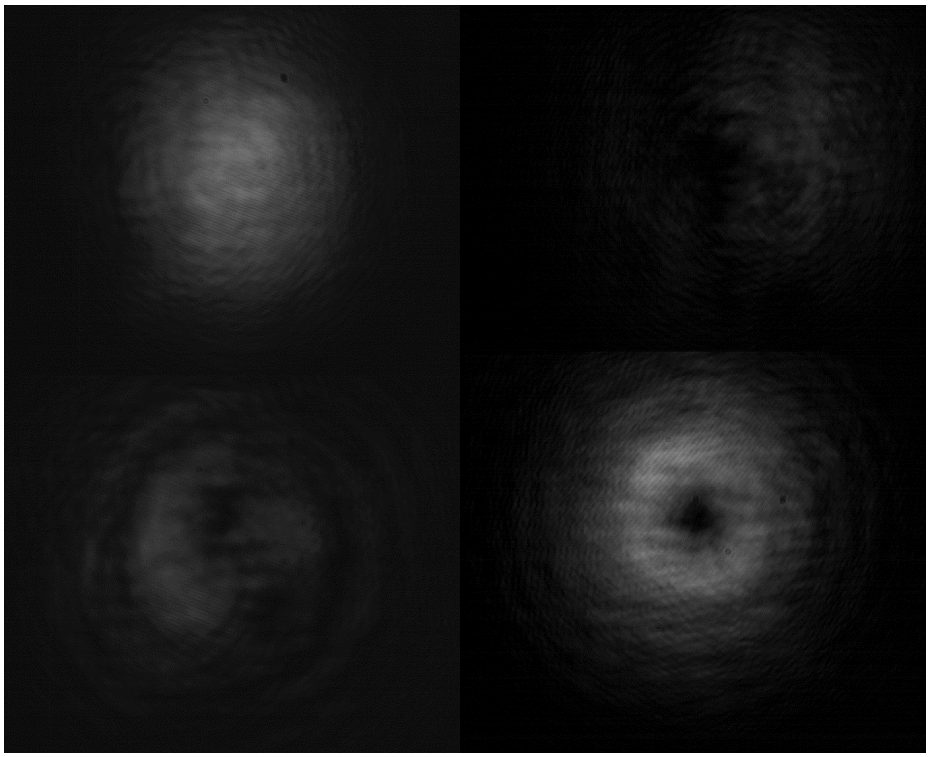

Figure 3.16: The even (left) and odd (right) output of the CoMMZI when a Gaussian (top) and l=1 beam (bottom) was sent in. The visibilities for both beams shown here is approximately 0.6.

The difference between the measured and expected visibilities could be explained by changes in the transverse profile of the beam during propagation. Nevertheless, the decreasing trend in visibility reflects the increasing flat phase component as the vortex is displaced farther from the center.

3.2.1 Limiting sampling area and signed visibility

As the previous section has shown, off-centered vortices and vortex-antivortex pairs reduce the visibility of the CoMMZI. In addition, an irregular intensity profile and the presence of other phase-disordering mechanics such as phonons would reduce the visibility even further. This would make it difficult for unequivocal vortex detection with a small number of photons, since it becomes indistinguishable from other sources of reduced visibility.

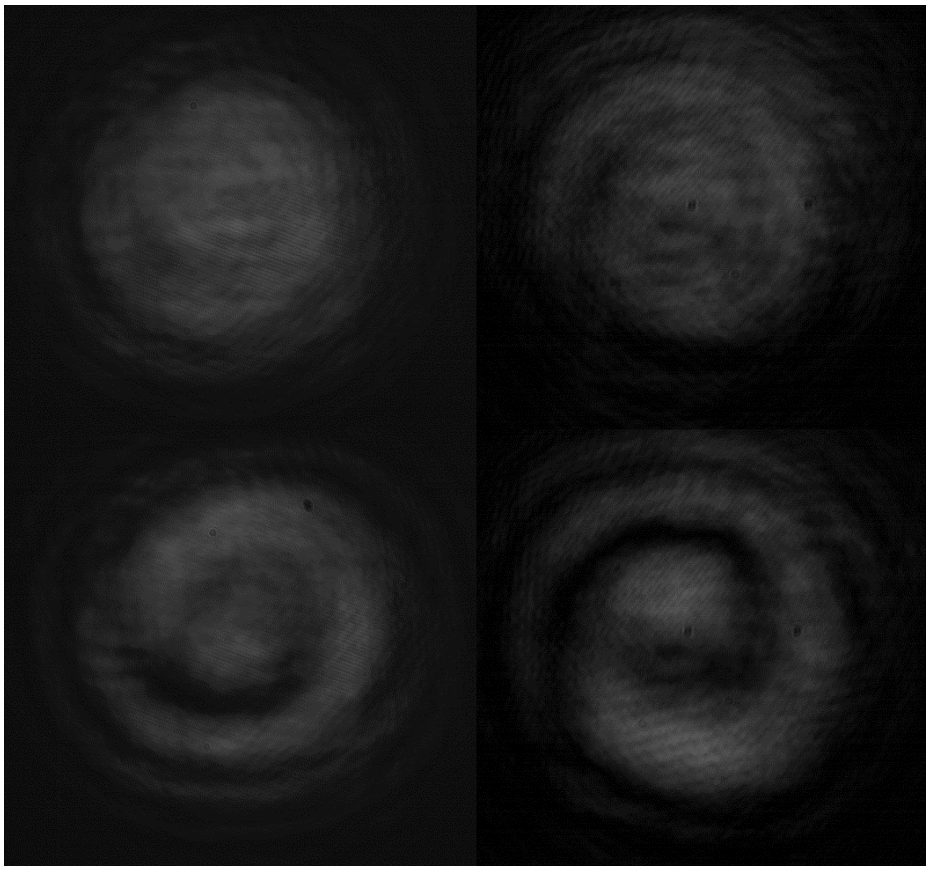

Figure 3.17: The even (left) and odd (right) output of the CoMMZI when a vortex-antivortex pair for which the cores were initially spaced 0.32mm apart (top) and 0.8mm apart (bottom). Visibilities for both results are approximately zero.

As discussed in Chapter II, it is thus necessary to impose stringent requirements for successful vortex detection. Such a requirement can be chosen by considering the fact that a field with a random spatial phase would show a visibility of 0, with the output from both ports being equal. When a l=1 vortex is present in the beam, we see a larger intensity output in the odd port compared to the even. Since the output of the odd port depends on a specific phase symmetry, the larger intensity is also a sufficient condition to determine the presence of vortices. For this, we define a

Displacement/Beam Waist	Measured Visibility	Expected Visibility
0.1	0.86 ± 0.02	0.90
0.2	0.68 ± 0.01	0.71
0.3	0.46 ± 0.05	0.49
0.4	0.32 ± 0.08	0.27

Table 3.1: Table depicting the measured and expected CoMMZI visibility for varying displacements of the vortex core from the center of the beam.

quantity known as signed visibility, given as

$$V_s = \frac{I_{even} - I_{odd}}{I_{even} + I_{odd}}, \tag{3.13}$$

where I_{even} and I_{odd} are the intensities from the even and odd port respectively. When the signed visibility is negative, it indicates vortices are present.

With this in mind, we look for methods to increase the chances of detection in scenarios for which low visibility is expected, such as in vortex-antivortex pairs. Figure 3.18 **a** shows the phase profile of a vortex-antivortex pair. The largest phase variation in the figure occurs close to the cores of the vortices, while the phase profile in the rest of the figure is fairly constant. Such a configuration would result in positive visibility. If a circular filter were applied to the phase such that only the portion with the largest variations in phase were sent into the CoMMZI, as in **b**, the resulting visibility would be negative. **c** shows a graph of signed visibility with the radius of this filter, and it is found that when the filter's radius is 1.3 times the displacement of an individual vortex (diameter 1.3 times the vortex-antivortex separation), the visibility is at its most negative.

This idea was tested using a circular filter superimposed on a CGH with a vortex anti-vortex pair. The oscilloscope screen on the top left of Figure 3.19 shows the voltage output in a photodetector when a vortex-antivortex pair was sent into the CoMMZI and the position of the large prism was varied sinusoidally by the piezo. The output shows 3 peaks and 2 valleys. When a circular filter with radius 1.3 times

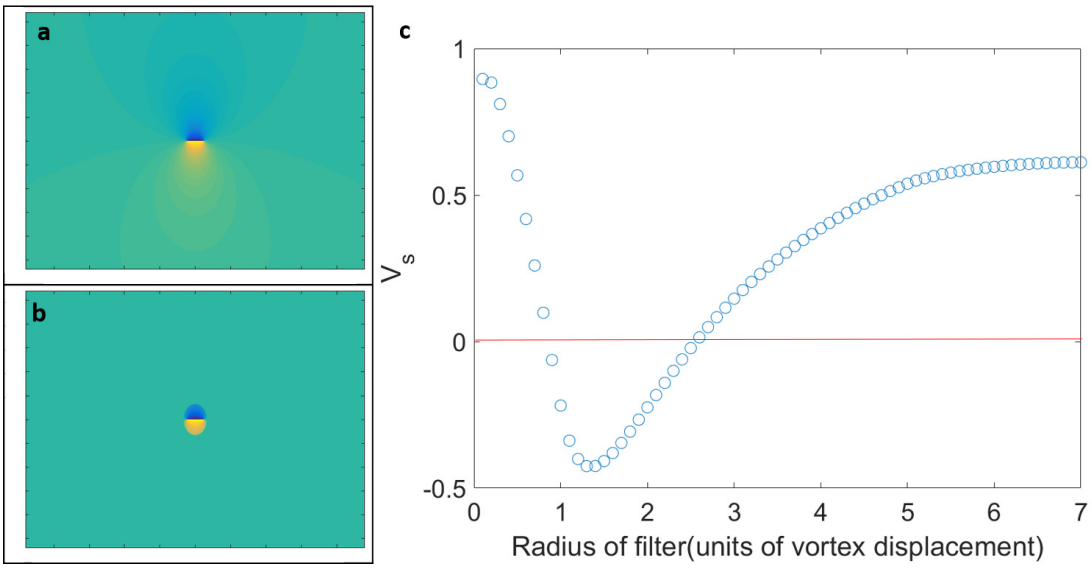

Figure 3.18: **a** depicts the phase profile of a vortex-antivortex pair, while **b** shows the same phase profile when a circular filter with a diameter 1.3 times the pair's separation is superimposed on it. **c** shows the change in the signed visibility with the size of the filter.

the vortex displacement was applied to the CGH, the output then became 3 valleys and 2 peaks, indicating a change in sign of the visiblity. The low intensity made it difficult to get an accurate read of the visibility, but the inversion of the voltage output is a sufficient indication. We were also able to recreate this change in the sign of the visibility using an iris with an uncut CGH.

The use of such filters is further explored when the CoMMZI was tested using polariton PL.

3.3 Experiments with Polariton Photoluminescence

Figure 3.20 shows the set-up we used for testing the CoMMZI with polariton PL. On the path to the CoMMZI, two f=300mm lenses were used to prevent the beam from getting larger than the CoMMZI's cross-section. A polarizing beam splitter (PBS) was used to linearly polarize the beam before it enters the CoMMZI, and a right-angled prism was placed after the even port to direct the port's output into a

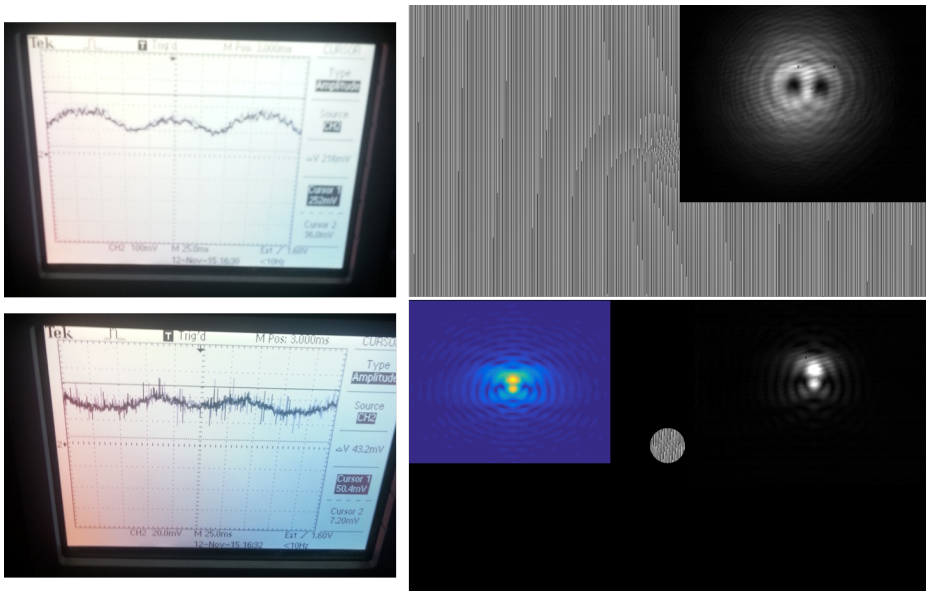

Figure 3.19: The left images show the change in the sign of the visibility when a circular filter is superimposed on a CGH designed to create a vortex-antivortex pair. The inset shows the transverse intensity profile of the uncut (top) and cut beam (bottom). The colored inset shows the simulated intensity profile for a propagated cut beam.

CCD camera. Both the odd and even port's output were focused into the CCD using a f=100mm lens. The polarization of the beam prior to entering the CoMMZI was to ensure maximum visibility. We have found the PL to be elliptically polarized and do not expect loss of vital information.

We first tested the CoMMZI with PL produced from a nonresonant Gaussian pump 2 μm in diameter. We do not expect vortex formation since the size of the beam is on the order of the healing length. This implies that if the beam were coherent, there should only be output from the even port. Prior to the experiment, we had adjusted the position of the large prism to ensure equal path length in both arms of the CoMMZI. This was done using a pulsed beam $\sim$ 100 fs in width. The path length was adjusted until we saw maximum visibility using this pulsed beam.

Figure 3.21 show the even (left) and odd (right) outputs for a position of -8meV detuning (top) and -6meV detuning (bottom). The even port's output is indeed

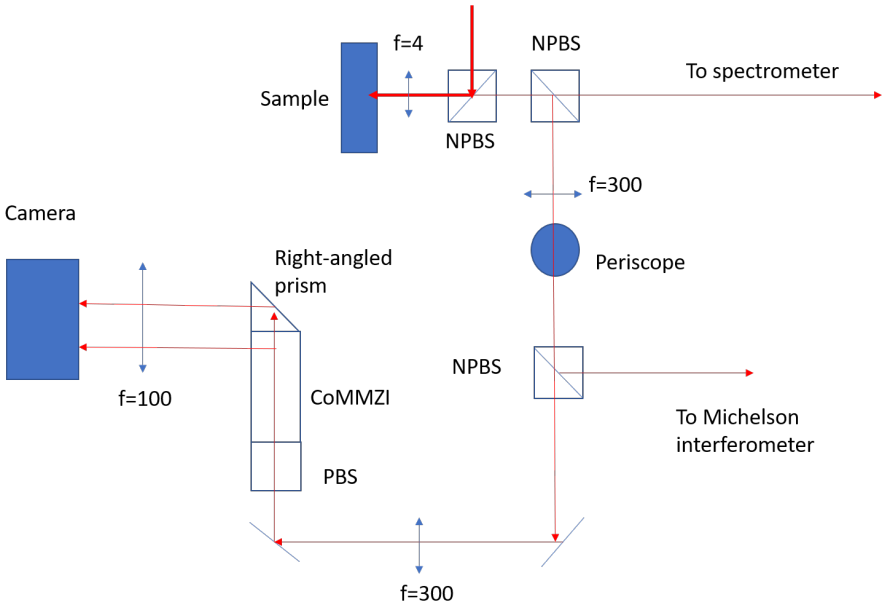

Figure 3.20: Set-up for testing the CoMMZI with polariton PL.

larger than the odd port's output, but the overall visibility found was very low. This is due to the presence of an incoherent population coexisting with the superfluid fraction. The larger diameter seen for the -6meV PL is due to the larger repulsive force experienced by the polaritons with the pump spot, which forces them to travel a longer distance from the pump spot before decaying.

As will be covered in Chapter IV, a possible method for detecting quantum vortices in polaritons is through the use of optically-induced ring pumps. This enables confinement of the population within a defined collection area to increase the chances of vortex detection. The separation from the exciton reservoir also reduces its influence. It is thus necessary to study the CW pump condition to identify sources of potential false positives.

Figure 3.22 shows the odd and even port outputs when an optically-induced ring pump of 30 μm diameter was used. This ring shape was created with an axicon. A notable difference when using this type of pumping is the appearance of higher order states when threshold is first achieved. The top row of Figure 3.22 shows an example of this higher order state, in which a standing-wave pattern is formed . As the pump

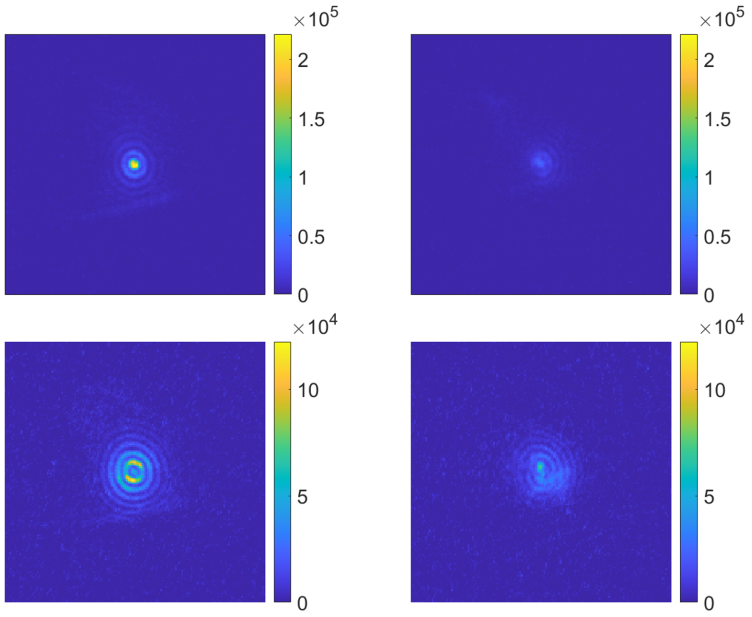

Figure 3.21: The even (left) and odd (right) output of the CoMMZI when polariton PL was sent in. The pump used was a Gaussian pump 2 μ m in diameter and 100meV higher in energy than the PL. The detunings used were -8meV (top) and -6meV (bottom). The visibility found was $\sim$ 0.1 for both detunings.

power is increased, the standing-wave pattern disappears and the pump spot becomes more homogeneous. The visibility also increases with pump power, with the highest power used showing a visibility close to 1. The higher order states formed within a ring trap will be the topic of discussion in Chapter IV.

Of particular attention to note is the presence of bright and dark spots at the center of the even and odd outputs respectively. The extent of the bright/dark spot is indicative of the range of the spatial coherence of the PL. At lower powers (top row of Figure 3.22), the spot covers a diameter of about $2\mu m$. At the highest power (bottom row of Figure 3.22), nearly the entire span of the PL emerges from the even port. This is consistent with what one would expect from reports on spatial coherence for polariton PL.

This variation in spatial extent across pump powers can be further explored by

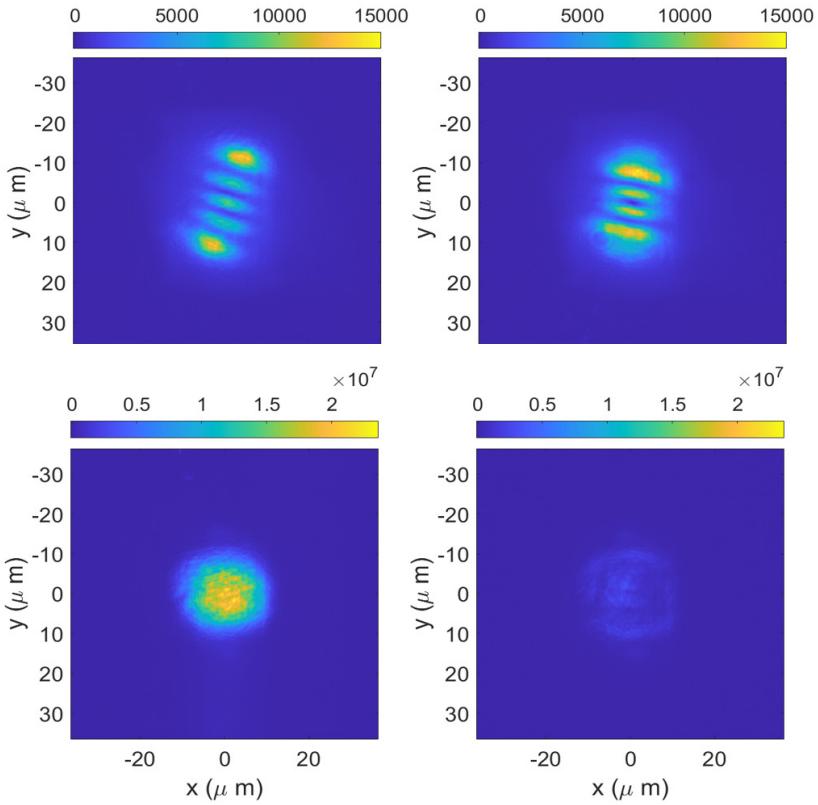

Figure 3.22: The even (left) and odd (center) output from the CoMMZI for polaritons pumped with an optically-induced ring pump. The images on the right show the original intensity profile before captured in the spectrometer. The PL shown here are for pump powers 30mW (top) and 186mW (bottom).

using a circular filter as described in Section 3.2.1. The circular filter is applied digitally to images from both ports of the CoMMZI, and the intensity within the filter is integrated across space to obtain the total intensity from each port. These quantities are then used to calculate the signed visibility as described with Equation 3.13. Figure 3.23, shows the plot of signed visibility (colorbar) with pump power and the radius of the circular filter. The evolution of the visibility is mostly what one would expect from a nonresonant pump, with visibility increasing with pump power as a larger fraction of the population is scattered into the ground state, and decreasing with increasing filter radius as the coherence drops farther from the center.

At 30mW, which was the threshold pump power, negative visibility was observed for filter radii from 3 μm to 20 μm. This result can be explained as a superposition of orbital angular momentum states near the center of the ring with an average orbital angular momentum of 0. More specifically, the Hermite-Gaussian mode seen at 30mW is a superposition of the Laguerre-Gaussian p=1, l=±1 and p=0, l=±3 state. The deviation from a signed visibility of -1 is due to imperfect alignment.

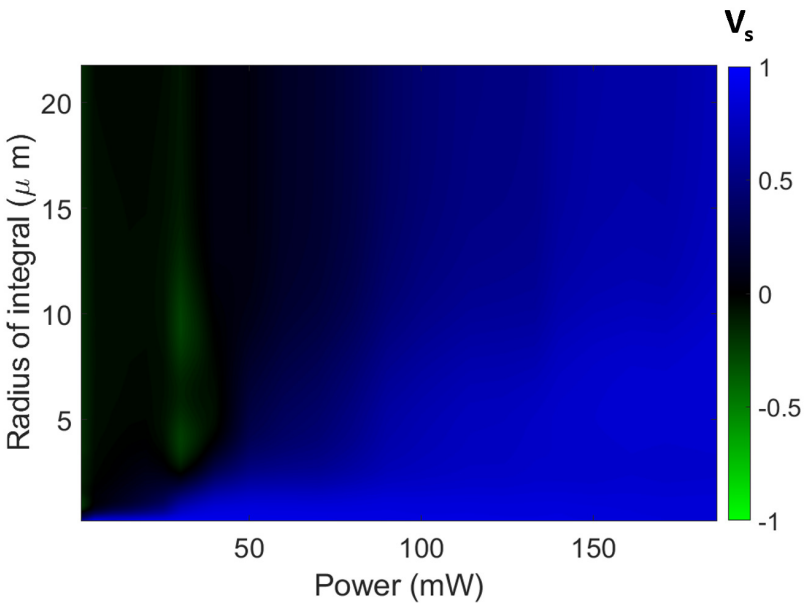

Figure 3.23: Signed visibility of the CoMMZI against pump power and filter radius when using an optically-induced ring pump.

3.4 Summary and Conclusion

In this Chapter, I have shown how vortex-carrying beams were created with a spatial light modulator and how we had tested the CoMMZI's efficacy in distinguishing orbital angular momentum states in both laser light and polariton photoluminescence (PL). I have shown that the CoMMZI can distinguish vortex-carrying beams of topological charge l=1 from a Gaussian beam, and that it can work with polariton PL. I have also shown how superimposing a filter on the signal can increase the chances of

detecting vortices.

The eventual goal is the detection of spontaneous vortices in a single realization of the condensate. This implies that the CoMMZI has to be able to successfully sort orbital angular momentum states with only a few thousand photons. To complicate matters, the vortices are not likely to be stationary, since they mostly follow the flow of polaritons which is influenced by pumping and decay. In Chapter II, I have shown simulations to demonstrate the efficacy of the CoMMZI for different expected scenarios of vortex behavior in a single-shot realization of a condensate. It is still necessary to further explore factors that would likely influence the formation and behavior of vortices, such as the degree of coherence and the interaction strength in the condensate itself. In the next chapter, I discuss these factors within a condensate formed in an optically-induced ring trap by looking at dispersion and temporal first-order correlation measurements. In the final chapter, I will describe a possible experiment that can be done with the CoMMZI for a single-shot realization.

CHAPTER IV

Multi-fluid Behavior for Polaritons in an Optically-induced Ring Pump

Early experiments with microcavity polaritons have used samples with short photon lifetimes ($\sim 10ps$). To maintain a steady population, a pump source would be required to continually supply photons, thus making polariton condensation an inherently non-equilibrium phenomenon. The short lifetime of the polaritons prevents it from achieving thermal equilibrium as well. This along with its driven-dissipative nature [116] not only adds to complications in experimental interpretation but also serves as a roadblock to practical applications. Early last decade, a new era of polariton studies began with the advent of samples possessing cavity lifetimes on the order of hundreds of picoseconds. This led to polariton lifetimes exceeding thermalization times, and evidence of equilibrium in the energy distribution and dispersion relationship has been observed [117, 118]. The low effective mass has also enabled long range motion on the order of 1 mm [119, 120], raising possibilities for applications in integrated circuits [121], waveguides [122] and logic devices [123]. The long range motion of long-lifetime polaritons has also enabled its study in traps with sizes on the order of tens of microns. In optically-induced traps, this is useful for separating the polaritons from the exciton reservoirs, which are confined to the perimeter of the trap at high powers [124, 125].

Recent studies done with this pump geometry have investigated quantum depletion [127], and polariton-polariton interaction strength in the absence of the exciton reservoir [128, 129]. These studies work primarily with the ground state of the ring trap, and while higher order states have been investigated [126], a study on the system dynamics as pump density is increased has yet to be conducted. In particular, the evolution of the system's coherence would lend insight into dephasing and broadening mechanisms that would be important for applications involving multiple modes. Furthermore, contradictory results on the polariton interaction strength [128, 131] highlight the need for deeper investigations even of the ground state. In this work, we investigate the evolution of the dispersion and temporal first-order correlation of the states of the ring trap as the system evolves with an increase in pump power. We observe the sudden onset of coherence as the system first crosses threshold into a narrow-band energy state, followed by its loss as more higher-order states are populated. At the highest pump powers, the system evolves into a composite of three states with coherence times spanning nearly three orders of magnitude. Our results are the first, to our knowledge, to document the evolution of temporal coherence of the states within an optically-induced ring trap for long-lifetime polaritons with increasing pump power. It lays groundwork for future studies on pre-thermalization dynamics within this system which would be valuable for applications seeking to use a coherent ground state.

In this chapter, I discuss spectrometric and temporal first-order correlation measurements for long-lifetime polaritons in an optically-induced ring trap. I first discuss how dispersion information can be obtained using a spectrometer set-up, followed by how temporal first-order correlation measurements can be obtained using a Michelson interferometer. I will then present our findings for long-lifetime polaritons in an optically-induced ring trap, then show some spatial and energy reconstructions at various pump powers which could lend us further insight into our findings. Fi-

nally, I will discuss how these results could give us information on what to expect for spontaneously formed vortices in such a system.

4.1 Obtaining energy-momentum information

A vital component of nearly every polariton experiment is the energy and momentum information of the position being studied. Signals from measurements at low pump power gives the single-particle dispersion, which contains information on the detuning of the position and thus its various properties such as light/matter fractions. At higher powers, measuring the momentum and energy would tell us when phase transition has taken place. This is seen as a sudden increase in the intensity of the photoluminescence signal (PL) and the accumulation of the signal into a narrow band of energy. In ground state condensation, this signal will be seen as a bright spot concentrated at the ground state and low momentum (k-space) values.

For obtaining dispersion information, the spectrometer is a valuable tool. The incoming PL is distributed along the energy axis though the use of a grating and 2 parabolic mirrors. With the spectrometer being factory-made, the main challenge lies in ensuring the k-space information is what is shown in the final result.

For that purpose, a series of lenses is used as part of the collection optics for the PL signal. A schematic of the set-up is shown in Figure 4.1. The photoluminescence signal is first collected from the sample using a powerful objective lens. This objective lens is able to collect up to 30 degrees of momentum information, making it the key factor in the success of this method. The signal is then sent through a series of 4 lenses, each spaced apart by the sum of its own and the adjacent lens' focal length. At each focal point, the Fourier transform of the signal is obtained, thus allowing for alternating real space and k-space signals. After the 4th lens, the k-space signal is then sent into the interferometer. If real-space information is desired, either one of the 300 mm lens can be removed.

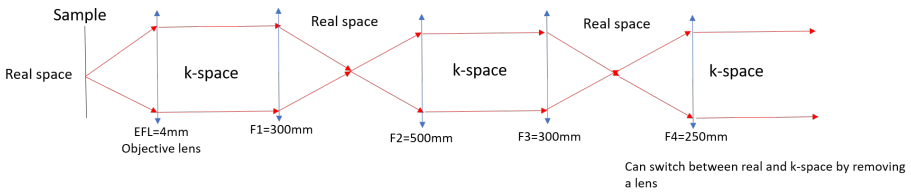

Figure 4.1: The lens arrangement for k-space imaging.

4.2 Temporal first-order correlation measurements

The coherence of the PL signal from polaritons is useful information for several reasons. The most obvious one being to determine if the population has undergone a phase transition. The coherence of a signal is measured by quantities such as its linewidth. In addition, the shape of the linewidth would give us insight into the various mechanisms leading to loss of coherence. For instance, a Lorentzian linewidth would be indicative of homogeneous broadening, in which the same broadening properties are experienced by all particles withini the same state. A Gaussian linewidth would be indicative of inhomogeneous broadening, for which different particles experience variations in broadening parameters. At a phase transition, the PL signal would show a large decrease in the linewidth. In a weakly interacting condensate, the main broadening mechanism would be lifetime broadening, and the linewidth would be a Lorentzian one. On the other extreme, a strongly interacting condensate would show a Gaussian linewidth.

While spectrometer readings could in principle tell us information on the coherence of the signal, they can often be limited by the spectral resolution. This would result in measurements of linewidths larger than the actual value. In addition, the convolution of the signal with the instrument response function would distort the shape of the signal, and thus likely give us erroneous insight into the physics of the system.

To obtain an accurate measurement of the coherence of the signal, the temporal first-order correlation function can be measured, which gives information on the co-

herence time of the signal. The linewidth of the signal can then be approximated by $\sigma \sim h/\tau_{coh}$, with τ_{coh} being the coherence time and σ being the linewidth. The temporal first-order correlation function, $g_1(\tau)$, is given as

$$|g_1(\tau)| = \frac{\langle E^*(t)E(t+\tau)\rangle}{|E(t)|^2}, \tag{4.1}$$

where $\langle E(t)\rangle$ is the field of the signal as a function of time and τ is the relative time delay between two copies of the same signal. The Fourier transform of $g_1(\tau)$ gives the spectral density, $S(\omega)$, which is proportional to the energy distribution of the signal. Thus, measuring $g_1(\tau)$ is one way to bypass the spectral resolution limitations of the spectrometer.

$|g_1(\tau)|$ can be measured using a Michelson interferometer. Such a set-up is shown in Figure 4.2. The signal from the sample is split evenly at the beam-splitter, with each signal being sent into separate retroreflectors. The retroreflectors used are corner retroreflectors, hence the beam is inverted along both the x and y-axis. The two beams are then collected by a lens and sent into a CCD camera to obtain real-space interference patterns (interferograms). Since both beams are inverted by the retroreflectors in the same manner, the fringe visibility, defined as

$$V = \frac{max - min}{max + min}, \tag{4.2}$$

where *max* and *min* refer to the maximum and minimum intensity along the fringe pattern respectively, should be uniform for a spatially-homogenous signal. One of the retroreflectors is placed on a moving delay stage, and as such it is possible to change the path length difference between the two arms. The delay between the signals is the controlled variable in this experiment, and the visibility can then be measured as a function of this delay time, τ. If the intensities in both arms are equal, the measured visibility at time delay τ would be equivalent to $g_1(\tau)$. A more general method of

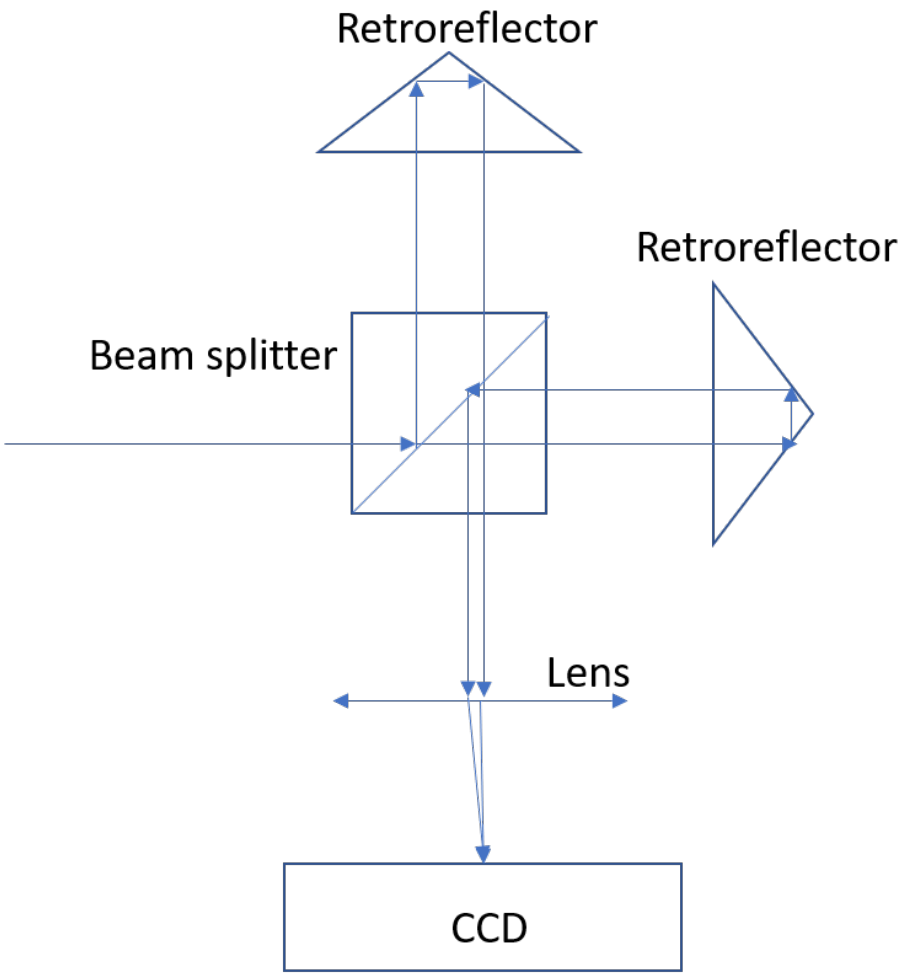

Figure 4.2: Michelson interferometer set-up with 2 retroreflectors, used for performing $g_1(\tau)$ measurements

extracting the value of $g_1(\tau)$ is discussed in Section 4.3.

Measurements of visibility often show decaying readings, a consequence of multiple frequencies within the same signal. Figure 4.3 illustrates this.

In an ideal monochromatic signal, the interference between equal signals in both arms would be totally constructive or destructive (left of 4.3), thus leading to a constant visibility of 1 for all delay times. If two signals of different frequencies were present (right of Figure 4.3), at a particular non-zero delay time, the maximum of one fringe pattern could be overlapping with the minimum of the other. This thus reduces the overall visibility of the interferogram. If only a few frequencies are present,

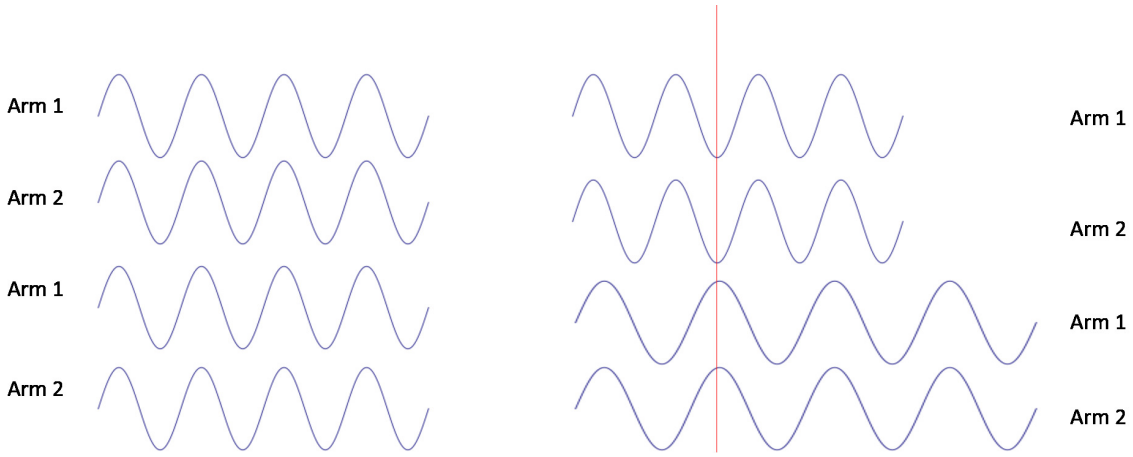

Figure 4.3: Total constructive interference takes place for all delay times if the signals in the two arms of the Michelson interferometer are monochromatic and of the same frequency (left). The visibility will thus always be 1. If multiple frequencies are present and at certain delay times, certain frequencies may show a bright fringe while other frequencies show a dark fringe. The averaging of different fringe intensities result in a 'washing out' of the overall fringe patterns and a decrease in the visibility.

the visibility would oscillate with delay time, showing maximums when all the fringe patterns show total constructive/destructive interference. This phenomenon is known as coherence revivals. As the number of frequencies increase, it becomes harder to find a delay time where coherence revivals can occur. This 'washing out' of multiple fringe patterns would lead to a drop in visibility to 0. Thus, the broader the range of frequencies present, the faster the drop in visibility to 0 and the shorter the coherence time.

4.3 Measurements for long-lifetime polaritons in an optically-induced ring trap

In a typical microcavity design, quantum well layers are placed within anti-nodes of a cavity enclosed within two Distributed Bragg Reflectors (DBRs). Each DBR is a set of alternating $Al_xGa_{1-x}As/AlAs$ layers of $\lambda/4$ thickness each. This design

maximizes the overlap of the exciton' dipole moment with the photon field, thus allowing for strong coupling in which the interactions between the two species give rise to polariton eigenstates. For our sample, the DBR sets have 32 and 40 layers respectively (Figure 4.4 (a)). The number of DBR layers is about twice that of early samples, which results in a high Q factor. Measurements of the linewidth give a Q factor of 10^4, as shown in Figure 4.4 (c), although the actual value is likely to be higher as our measurements were limited by the resolution. The thickness of the sample is $3\lambda/2$ and thus holds 3 sets of quantum wells. We made measurements on a position with a detuning of -8.4 meV, implying a photon fraction of ~ 0.8 . The low effective mass and interaction strength at this position allows collection of a large number of photons before thermalization, thus shedding light on the processes leading up to it.

To pump the sample, we used a continuous-wave laser with an energy ~ 100 meV above the lower polariton ground state energy. The off-resonance pumping ensures that coherence from the pump is not transferred to the polaritons, and that coherence observed in the photoluminescence (PL) signal can be interpreted as spontaneous symmetry breaking taking place within the polariton system itself. To reduce the heat load on the sample, an Electro-Optical Modulator was used to modulate the pump's intensity in time. The modulation was done at 1 MHz frequency with a duty cycle of 10%, such that the pump was incident on the sample for 100 nanoseconds during each cycle. The ring shape of the pump was created with a 0.5 degree axicon placed upbeam of the sample. A telescope set-up was used to change the ring's diameter to $50\mu m$.

4.3.1 Dispersion measurements

The condensation of polaritons can be observed as a sharp rise in the intensity of the photoluminescence (PL) signal captured with a spectrometer. Our results

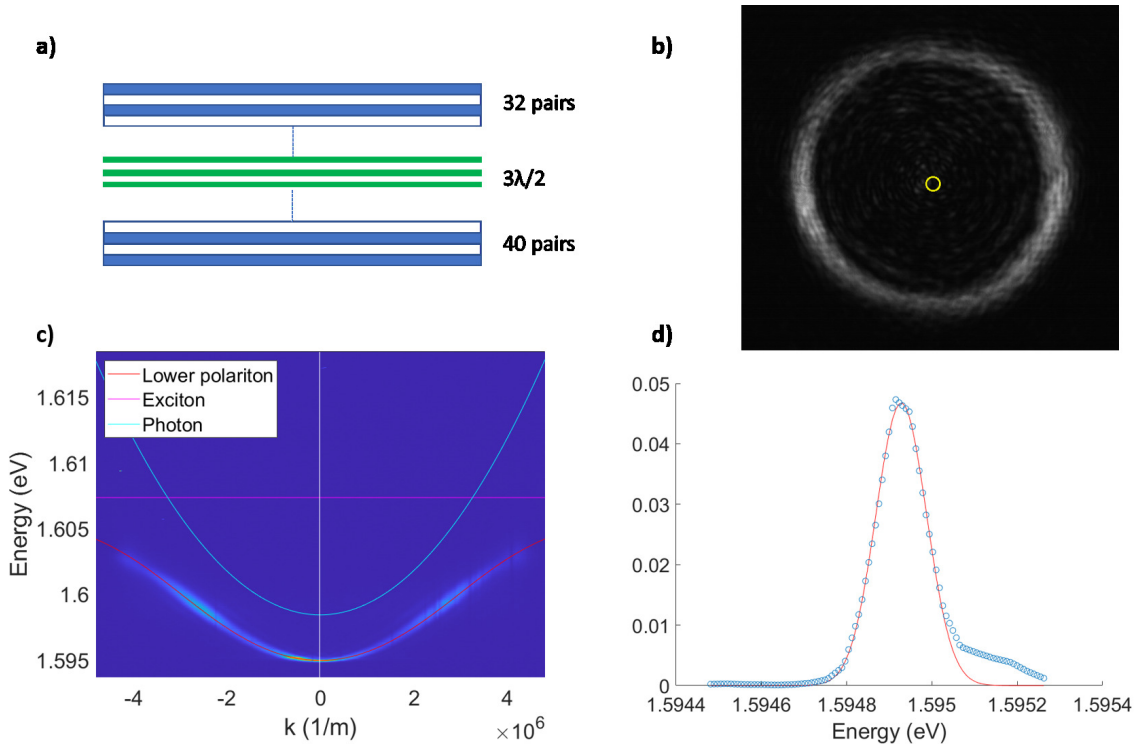

Figure 4.4: (a): Schematic of sample. (b): Profile of pump created by axicon, yellow circle indicates location of focused spot without axicon. (c): Dispersion of lower polaritons at a detuning -0.5meV more negative than shown in this work, together with the corresponding photon dispersion and exciton energy. Spectra was obtained from a $5\mu m$ radius about the center of the ring pump. Inset shows intensity profile taken across $k = 0$ line (white line) and its fit to a Gaussian profile. The linewidth found from fitting is 0.1 meV which gives a cavity Q factor of 10^4, although this measurement is resolution limited and the actual Q factor is thus likely to be higher.

reveal the existence of two threshold behaviors, as seen in Fig. 4.5 (a) and (b). Below 60 mW, the single particle dispersion can be seen, along with a blurring in the negative k direction indicating ballistic flow in that direction (Fig. 4.5 (c.1)). At 50mW, the single particle dispersion can still be seen, but the population has begun to accumulate towards lower energy states between 1.5955 eV and 1.596 eV. The first threshold occurs between 50 mW and 60 mW pump power, and is seen as a sharp rise in the excited state population and fraction. This corresponds to a condensation into a narrow band of higher energy states centered around 1.596 eV, as can be seen

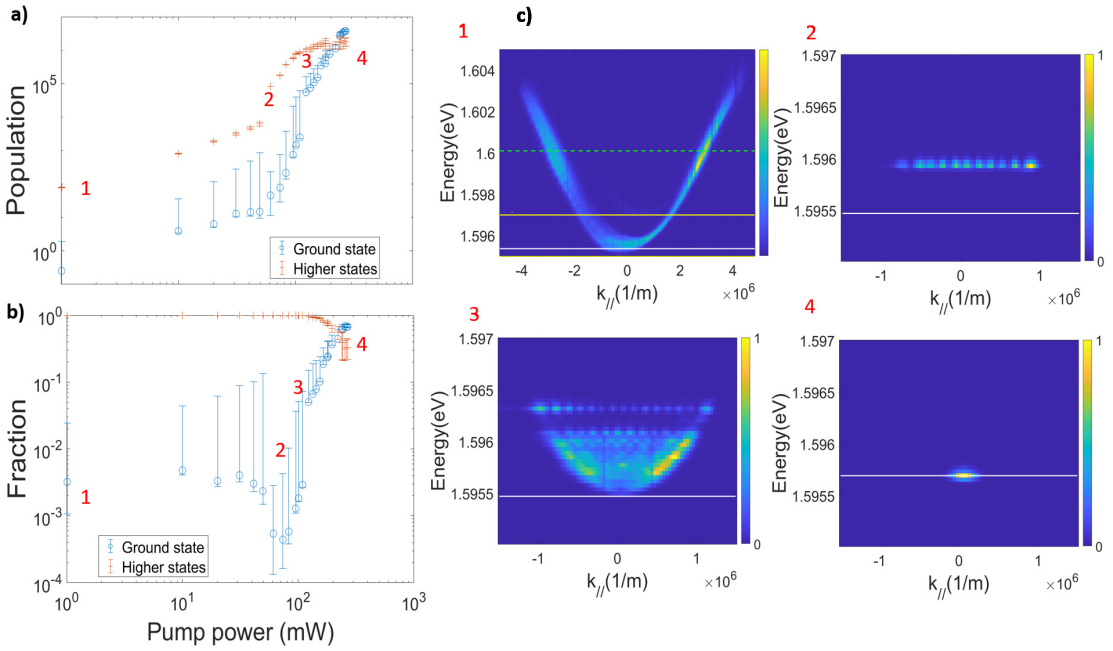

Figure 4.5: (a) and (b): Population intensity and fraction evolution respectively. Positions numbered on the graph correspond to the respective spectrometeric images shown in (c.1-4). The white line indicates the ground state energy at that particular pump power. This range is set to 1 spectral resolution (0.1 meV) for all powers. The method of determining the range of ground state and excited state energies is described in the text. (c): Spectrometer images taken for k space at 1mW (1), 60mW (2), 100mW (3), and 270mW (4). No spatial or spectral filtering was used.

in Fig. 4.5 (c.2). The second threshold is seen as a sharp rise in the ground state population and fraction between 120 mW and 130 mW pump power, corresponding to a large accumulation into a low momentum ground state as seen in Fig. 4.5 (c.4). We do not see an immediate drop in bandwidth, unlike for the first threshold. This is due to the persistence of populations in higher energy states even up to the highest power. At 180 mW, even though the polaritons are concentrated in the $k \sim 0$ state, a faint quadratic dispersion is still visible. At the highest pump power used (270 mW), the population has almost completely scattered into the $k \sim 0$ state with the quadratic dispersion only visible with intensity on a log scale.

The polariton population was approximated from the far-field PL signal by as-

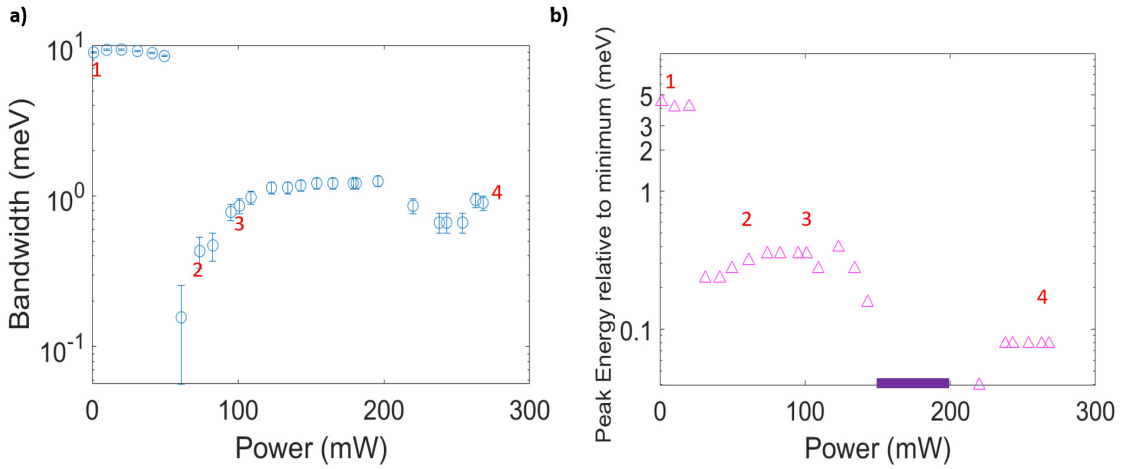

Figure 4.6: Top: Evolution of bandwidth with power. Bandwidths were determined by finding the energy range for which the population exceeds 0.05 times the maximum value, using population distributions integrated along the k-axis. Bottom: Evolution of the energy value with the largest population. Reference is taken from the corresponding value at 1mW pump power.

suming the signal to be rotationally symmetric. The average of the intensities at positive and negative k values was multiplied by a factor of $2\pi|k|dk$, for which dk was taken to be the length of a pixel in k space. The intensity at $k \sim 0$ was multiplied by $\pi|k|^2$. The PL signal at each pump power were then divided into two energy sets; a ground state energy set and an excited state energy set. The range of the ground state energy set was taken to be the spectrometer resolution. Below the second threshold, the center of this range was taken as the lowest energy with an observable PL signal, found by visual inspection of the spectrometer image at log scale intensity. At the lowest pump powers, ballistic flow is observed through a spread in population at lower momentum and energy. We thus chose a large error range which covers the span of populated states, which came to 0.5 meV. For powers above initial condensation, the error range was taken to be the spectrometer resolution. Above second threshold, the ground state range was defined to be within 1 spectrometer resolution of the energy with the largest population at $k \sim 0$. The polariton population at each power is then found by integrating across momentum values within the ground state energy range,

while the error is found by integrating across momentum values within the ground state energy range. The excited state energy range was assumed to be the energies above the ground state energy range, while the excited state error range was assumed to be half that of the ground state error range. The excited state population was found using the same calculations as for the ground state population.

The bandwidth of the polariton population is a useful quantity for monitoring the onset of phase transitions. A sudden drop in bandwidth would indicate a large accumulation of population within a narrow band of energies, indicative of threshold behavior. A sharp rise in the population is also expected to be seen when this happens, due to stimulated scattering by polaritons in the condensed state. We calculated the population bandwidth by taking the energy range for which the population exceeds 0.05 times the maximum value, after integration along the momentum axis, the results of which are shown in Fig. 4.6 (a). The bandwidth calculated at first threshold was found to be $\sim 0.1meV$, and is thus resolution-limited. Above the first threshold but prior to the second, the population was observed to scatter into a wider range of energy states, with the highest energy state 0.4 meV above the state at 60 mW (Fig. 4.5 (c.3)), a result of greater repulsive interactions between the polaritons formed along the ring. The bandwidth calculated was found to be $\sim 1meV$. We see a drop in bandwidth to 0.6 meV above 200 mW, as the system condenses into the ground state. This is larger than the bandwidth calculated at first threshold due to a small population occupying higher momentum states.

To examine the occupation of the higher-order modes, a quantity that could be measured is the energy with the largest population value, defined here as the peak energy. Fig. 4.6 (b) shows the evolution of the peak energy with pump power, calculated relative to the minimum value found between 150mW to 200mW. From 1 mW to 20 mW, the polariton population is accumulated in bottleneck states, and thus the peak energy is 5 meV above the ground state. We see a sharp drop of the

energy with peak population at 30 mW of 4 meV. This is followed by a rise of 0.2 meV after the first threshold. At second threshold, the population begins to accumulate in the ground state, resulting in a drop of 0.5 meV. From 150 mW up to 270 mW, we see a total blueshift of $\sim 0.1meV$, a result of inter-polariton interactions.

4.3.2 Temporal first-order correlation results

We performed $g_1(\tau)$ measurements using a Michelson interferometer with a retroreflector in each arm. To find the evolution of $g_1(\tau)$ at different pump powers, we chose the fringe profile corresponding to the position of the brightest spot in the interferogram taken at 272mW (dashed line in Fig 4.7 (a)). The 1-dimensional profile was then fitted to the equation:

$$I(x) = I_1 + I_2 + 2\sqrt{I_1 I_2}|g_1(\tau)|\cos(k_x x + \phi). \tag{4.3}$$

I_1 and I_2 are the intensities in each arm of the Michelson interferometer and were measured to be equal. k_x is the projection of the wavenumber in the x-direction and ϕ is the phase delay between the two arms. To account for instabilties in the set-up, we took the largest of 3 $g_1(\tau)$ measurements at a single delay time. The error bars in Fig. 4.7 were calculated from fitting errors at the chosen measurement. The resulting trends were then fitted to various functions, depending on the apparent shape of the graph.

Our results were fitted to three different functions for analysis. The simplest is:

$$|g_1(\tau)| = \exp\left(-\frac{(t-t_o)^2}{\tau_c^2}\right), \tag{4.4}$$

where t_o is the bias in time zero and τ_c is the coherence time. We have also used a

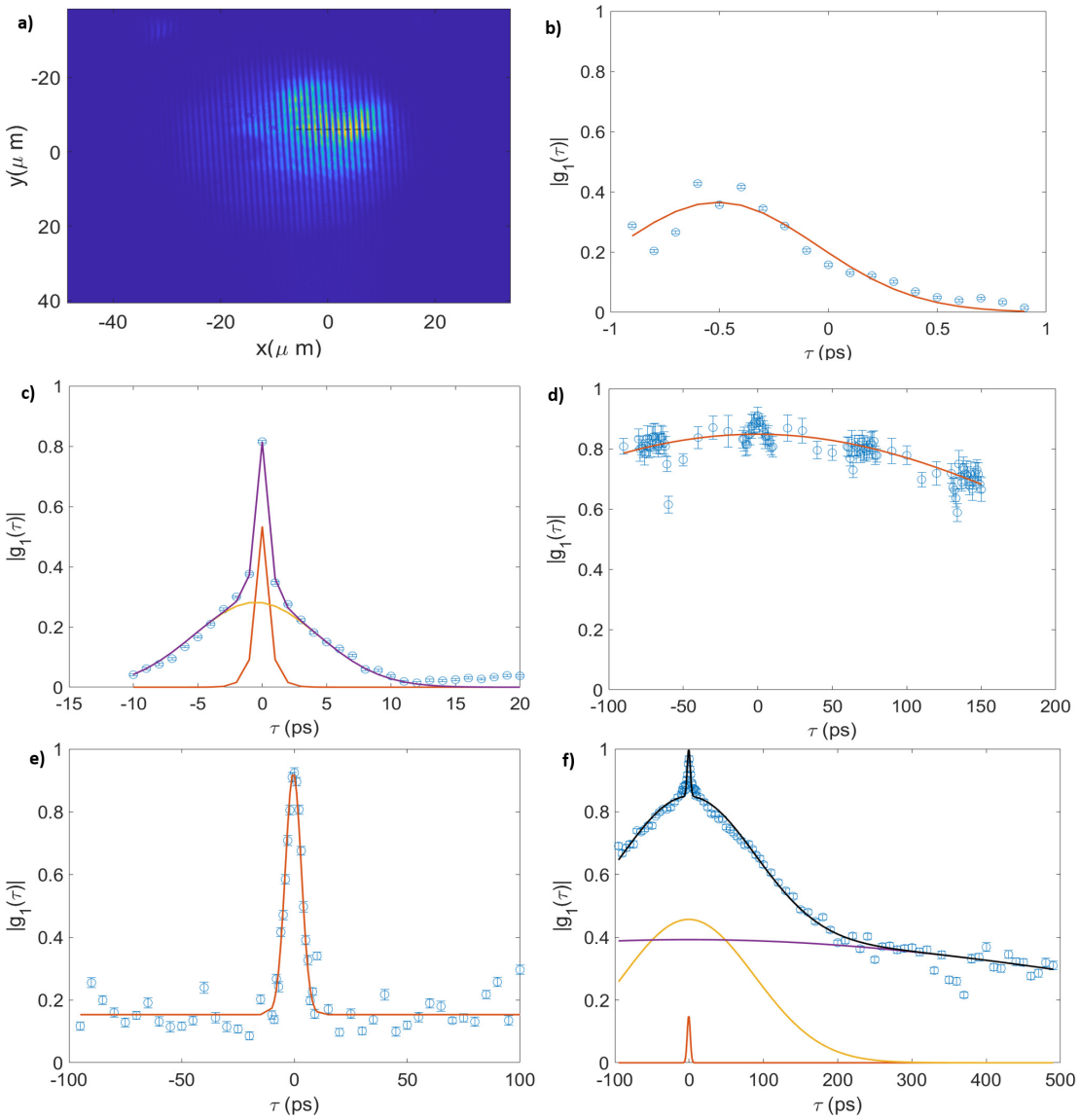

Figure 4.7: (a): Interferogram taken at a pump power of 270mW. The dashed line indicates the position from which $|g_1(\tau)|$ measurements were taken. The following data and fits were taken with pump power (b) 1mW, (c) 50mW, (d) 60mW, (e) 100mW, (f) 270mW. The equations used for fitting were Equation (4.4) for (b), (d) and (e), Equation (4.5) for (c), and Equation (4.6) for (f). For (e), a constant was added to the fit to account for vertical displacement caused by coherence revivals.

sum of a Gaussian and Exponential function, given by

$$|g_1(\tau)| = f_1 * \exp\left(-\frac{(t-t_o)^2}{\tau_{c1}^2}\right) + f_2 * \exp\left(-\frac{|t|-t_o}{\tau_{c2}}\right), \tag{4.5}$$

where a and b is the fraction of the Gaussian and Exponential population respectively. Finally, we have used a sum of three Gaussians:

$$|g_1(\tau)| = f_3 * \exp\left(-\frac{(t-t_o)^2}{\tau_{c3}^2}\right) + f_4 * \exp\left(-\frac{(t-t_o)^2}{\tau_{c4}^2}\right) + (1-f_3-f_4) * \exp\left(-\frac{(t-t_o)^2}{\tau_{c5}^2}\right). \tag{4.6}$$

The value of t_o was found from fitting at the lowest power of 1 mW, and fixed at this value for every other fit.

Below second threshold, temporal first-order correlation measurements show at most two distinct behaviors (Fig. 4.7). Fig. 4.7 (b). shows $|g_1(\tau)|$ as a function of delay time at 1mW. The maximum visibility is ~ 0.4 due to the low signal-to-noise ratio in the interferogram. The red curve shows the fit to a Eqn. (4.4) with a coherence time τ_c of 0.7(0.2) ps. Fig. 4.7 (c) shows the evolution of $|g_1(\tau)|$ with time delay for 50 mW. The fit is to Eqn. (4.5), with τ_{c1} and τ_{c2} at 6.0(0.6) ps and 0.6(0.2) ps respectively. The Exponential function can be attributed to the population in higher k-states and the Gaussian function the cumulation of population at lower momentum. We note that there is a revival that can be seen after 10ps delay. This is indicative of the coherent states that begin to form at this power, as can also be seen in Fig 4.5 (c.2). Fig. 4.7 (d) shows the $|g_1(\tau)|$ evolution at 60 mW. The fit is to Eqn. (4.5) with $\tau_c = 320(20)$ ps. The sudden increase in coherence time is consistent with the sharp drop in bandwidth as shown in Fig 2d. Small coherence revivals can also be seen at periods of 70ps, indicating that there are two coherent states spaced closer than the spectral resolution at this power. Fig. 4.7 (e) shows the $|g_1(\tau)|$ evolution at 100mW. Only the value between -20 ps and 20 ps delay was fit to Eqn. (4.4), with a constant added. to account for coherence revivals appearing after 20ps. The revivals show varying periods and no decay envelope could be observed, indicating the presence of multiple coherent states. The coherence time for the fitted Gaussian function is 5.0 (0.4) ps. We will refer to the sub-picosecond coherence time fraction

as the non-thermal fraction, the ps coherence time fraction as the thermal fraction, and the ~ 100 ps coherence time fraction as the quasi-condensate fraction.

Above second threshold, measurements found three distinct behaviors with coherence times varying by three orders of magnitude. Fitting for the three highest powers were done with Eqn. (4.6). We attribute each of these functions to a non-coherent fraction at higher momentum states, a fraction with coherence time on the order of a hundred picoseconds, and a fraction with coherence time close to 1 nanosecond respectively. At 180 mW, the thermal and quasi-condensate fractions (f_3 and f_4) are similar at 0.42(0.01) and 0.4(0.1) each, and have a coherence time (τ_{c3} and τ_{c4}) of 4.6(0.4) ps and 200 (40) ps respectively. There were too few data points to acquire an adequate fit for the near-nanosecond coherence time fraction, and the resulting error in the fit was thus large (τ_{c5} = 1000 (2000) ps). At 240 mW, the 3 component behavior becomes more obvious. The fractions f_3 and f_4 are 0.18 (0.01) and 0.52 (0.07) respectively. The three coherence times τ_{c3}, τ_{c4} and τ_{c5} are 2.8 (0.6) ps, 160 (20) ps and 700 (200) ps respectively. At 270 mW, shown in Fig. 4.7 (f), f_3 and f_4 are 0.15 (0.01) and 0.46 (0.03) respectively while τ_{c3}, τ_{c4} and τ_{c5} are 2.9 (0.6) ps, 125 (8) ps and 1000 (200) ps respectively. We will refer to the near-nanosecond coherence time fraction as the condensate fraction.

4.4 Discussion

From Fig. 4.8 (a), there is a decreasing trend seen for the coherence times of thermal and quasi-condensate populations, although the order of magnitude is unchanged. This thermal populations persists across both thresholds, and the quasi-condensate population appears above the first threshold and persists across the second. The gradual decrease in coherence times is likely a result of increasing interactions and increasing density with pump power. Based on comparisons with spectrometer images, the thermal fraction likely arises from the spread of populations across energy states

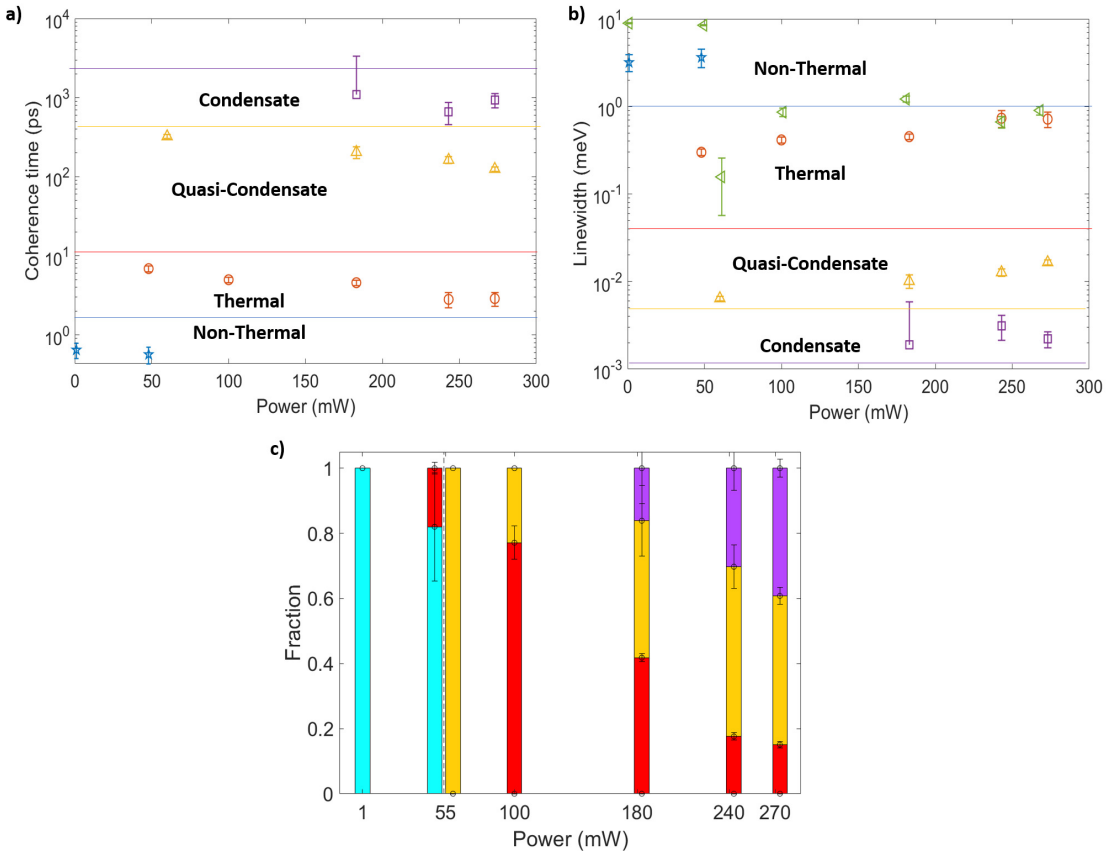

Figure 4.8: (a): Coherence times as found from fitting visibility data, separated into four categories according to their order of magnitude. (b): Linewidths as calculated from the coherence times in (a) and the corresponding bandwidths in Figure 4.6. (c): Population fractions as found from fitting visibility data. (d): Population fractions from spectrometer data at the corresponding pump powers, as calculated in Figure 4.5 (b).

within the finite square well created by the confinement of the polaritons within the optical trap. The quasi-condensate population at 60mW is clearly attributed to the narrow energy spread at first threshold. At 180 mW and above, two separate populations can be seen in the spectrometer image, although three can be measured from $g_1(\tau)$ measurements. This indicates that either the quasi-condensate and condensate population are so close in energy that they are not distinguishable in the spectrometer, or that the two populations exist at different times during the pump's duty cycle. Fig. 4.8 (b) shows the linewidth calculated from coherence times in (a). The

bandwidth calculated from spectrometer is shown on the same axis. The bandwidth is seen to be larger than or similar to the largest linewidth measured in our $g_1(\tau)$ results, which is expected due to the limited spectral resolution of the spectrometer.

Fig. 4.8 (c) shows the fraction of populations as measured in $|g_1(\tau)|$ measurements. Among the three highest pump powers, there is a clear trend of increasing condensate fraction. The quasi-condensate fraction increases from 180 mW to 240 mW and remains nearly constant up to 270mW, while the thermal fraction shows a clear decrease. This suggests that the condensate fraction is the final thermalized state of the system while the quasi-condensate may be an intermediate phase. To check the effects of weaker interaction strength, we have also performed similar measurements on a sample position 2 meV more negative in detuning. $|g_1(\tau)|$ measurements over that position do not show a clear sign of a near-nanosecond coherence time population at highest pump powers, and the resulting fit for the $\sim$ 100 ps coherence time fraction was closer to an Exponential decay rather than a Gaussian one (Figure 4.9). Spectrometer images show a wider spread of population in energy at highest powers (3 meV as opposed to 1.5 meV), and the thermal fraction is larger (0.43 as opposed to 0.15), suggesting that the absence of strong interactions at this detuning prevents the polaritons from achieving the condensate state before decaying. This presents more evidence that the quasi-condensate population is indeed an intermediate scattering step, although time resolved experiments are required to confirm this.

4.5 Summary and Conclusion

We have studied the evolution of long-lifetime polaritons through spectrometric and temporal first-order correlation measurements. Consistent with previous reports, we have found the initial condensation of the system into higher-order energy states, followed by scattering into lower energy ones and an eventual condensation into a low momentum ground state. Our $|g_1(\tau)|$ measurements reveal the presence of three

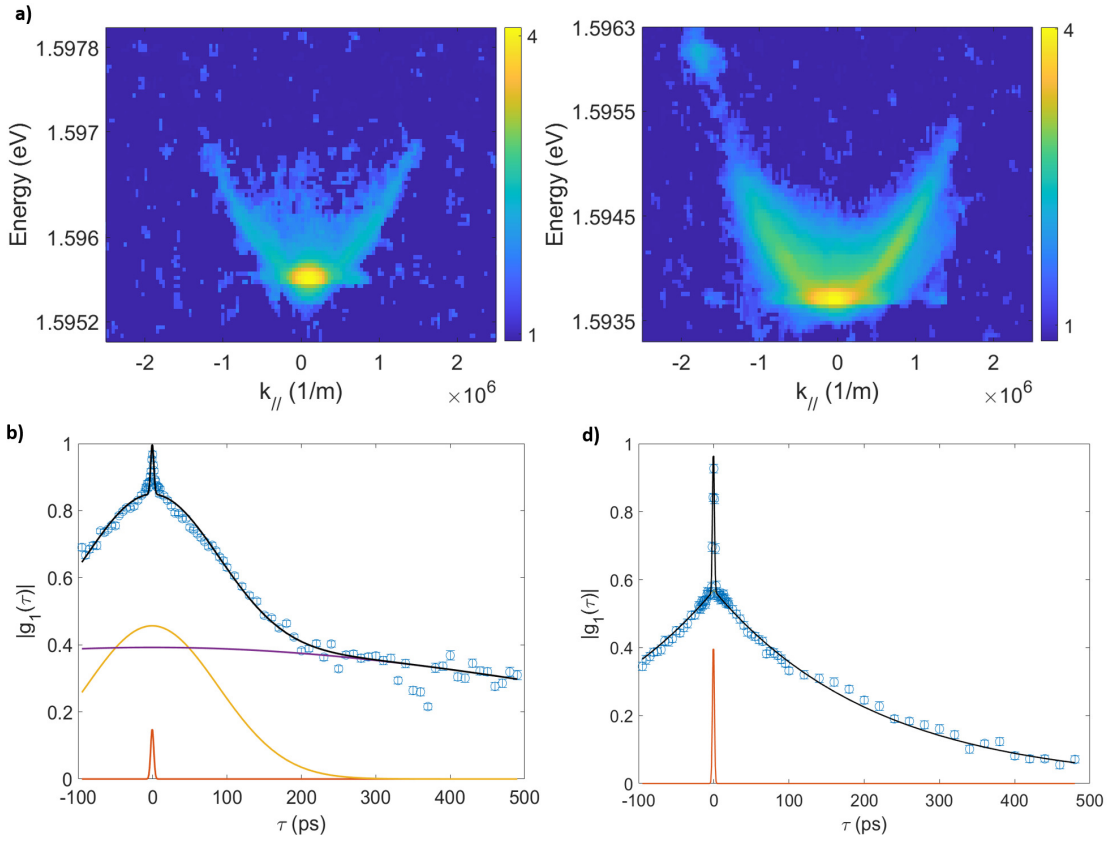

Figure 4.9: Comparison of log_{10} scale spectrometer images (a and c) and temporal first-order correlation function (b and d) at $\sim$ 270 mW pump power for -8.4 meV detuning (a and b), and -10.5 meV detuning (c and d). The photoluminescence signal for -10.5 meV detuning show a spread of 3 meV in energy, while the signal for -8.4 meV shows a spread of 1.5 meV. The near-nanosecond coherence time fraction is absent in the $|g_1(\tau)|$ evolution shown in (d), and the thermal fraction is more prominent (0.430 ± 0.008) than in (b) (0.15 ± 0.01).

different populations at highest powers, with coherence times and thus interaction strengths differing by three orders of magnitude. The quasi-condensate population is likely an intermediate scattering step before the final condensation into a condensate state. If so, time-resolved measurements would be useful in determining if the quasi-condensate state is a pre-thermalized state of the system [136, 137]. Our work lends insight into decoherence and condensation mechanics in long-lifetime polaritons confined within an optical ring trap, and paves the way for further studies

likely involving combined temporal and spatial first-order correlation measurements, alongside time-resolved measurements.

The low interaction strength fraction could have rather interesting consequences for the detection of vortices by the CoMMZI. If there is little interaction between vortex cores and its environment, it would mean that the vortex motion would be largely determined by the flow of the polaritons. Considering that the ground state condensate occupies low momentum states, this would mean that the vortices would be slow moving. As described in Chapter II, such situations would be ideal for detection with the CoMMZI. In addition, if the hundred-picosecond coherence time fraction is indeed a prethermalized state, it would be interesting to see if the transition to the near-nanosecond fraction is a result of vortex-antivortex recombination.

CHAPTER V

Future Work

As demonstrated in the previous few chapters, the detection of spontaneously created vortices in a single-shot realization of a polariton condensate is within th realm of possibility, but challenging. In this final chapter, I propose future work which could contribute to further understanding of state evolution within the optically-induced ring trap and push towards the unequivocal detection of such vortices while providing understanding and context to the nature of the vortices detected.

5.1 Future work for analysis of states in an optically-induced ring trap

In this section, I will first discuss spatial tomography scans which could be used to complement temporal first-order correlation measurements, as well as spatial first-order correlation measurements that would lend us insight into the likelihood of vortex formation. I will then discuss time-resolved experiments that could be performed to gain insight into the thermalization of the sample.

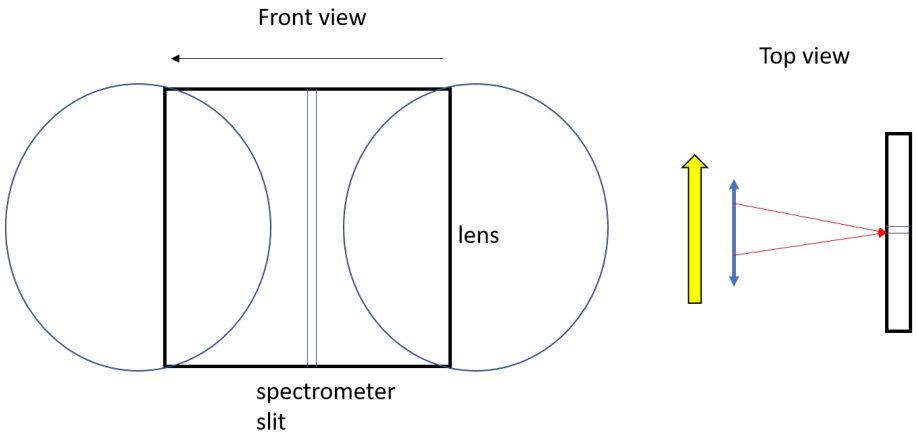

Figure 5.1: How spatial tomographical scans are carried out. The lens before the spectrometer is moved laterally across the spectrometer slit. Slices of the real space image is captured at each position.

5.1.1 Spatial Tomography scans to complement temporal first-order correlation measurements

As discussed in Chapter IV, our comparisons for the population fraction shown in the spectrometer and calculated from $g_1(\tau)$ measurements were limited due to the fact that spectrometer measurements were taken in momentum space (k-space). It would be useful to have access to the energetic distribution and the spatial profile of the various states within the optical ring trap. A direct comparison of the fraction calculated in $g_1(\tau)$ measurements could then be made with the corresponding energy distribution for the same spatial location. To achieve this, a spatial tomography scan could be done to create a 3-dimensional map of energy and space.

Figure 5.1 show how the spatial tomography scan is carried out. The lens prior to the spectrometer is placed on a motor-controlled stage and moved laterally across the spectrometer slit. This would shift the real space image of the polariton photoluminescence (PL) past the slit in which energy information could then be captured for each slice. The 3-dimensional map of energy and space is then constructed by piecing each slice together to reconstruct the real space image.

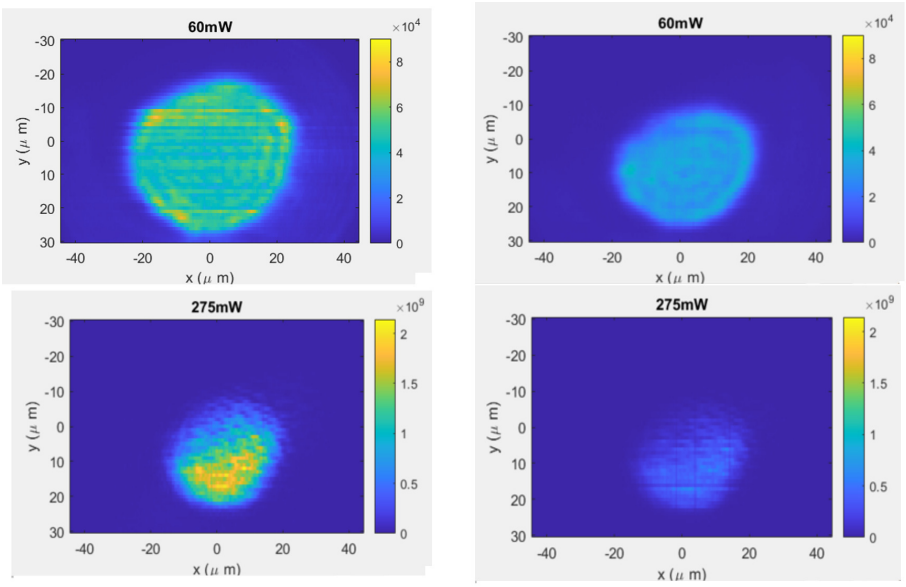

Figure 5.2: Scan results for -8.4meV detuning for 60mW (top) at 1.5959 eV (left) and 1.5957 eV (right). Results for 275mW (bottom) are at 1.5958 eV (left) and 1.59576 eV (right).

An example of such a scan is shown in Figure 5.2. The scan was performed for a spot on the sample with the same detuning for Chapter IV. Slices along the x-direction (long axis of sample) were taken. The top row shows the reconstruction of the energy states for 60mW of pump power, the threshold power for this position on the sample and ring diameter. The bottom row shows the reconstruction of the spatial profile at 275mW, when the ground state was achieved.

It should be noted that these results were not used to make comparisons with measurements shown in Chapter IV, as these scans were done with a different experimental set-up and as such, variations in the pumping conditions may have led to different observations. It should be noted that the higher order state shown in Figure 5.2 is not the standing wave ripple pattern shown in Chapter IV, despite attempts to recreate the same pump conditions. Instead, the pattern shown is closer to whispering-gallery modes as described in [126]. The energy states at intermediate pump powers also resemble more of a continuum distribution, instead of the clearly

discrete distribution seen in Chapter IV.

Even in a successful comparison, the spatial tomographical scan would still be limited by the spectral resolution of the spectrometer. It would thus be helpful to consider the measurement of spatial first-order correlation.

5.1.2 Spatial first-order correlation measurements

As previously discussed in Chapter III, the Berezinskii-Kosterlitz-Thouless transition (BKT) is characterized by a transition of the first order spatial correlation function from an exponentially decaying trend to a power law decay. The regime in which an exponentially decaying trend is observed is associated with the appearance of free vortices. As such, measurements at different pump powers would inform the experimenter of conditions in which vortices are more likely to be present.

Obtaining information on the spatial first-order correlation function requires a Michelson interferometer set-up similar to that shown in Chapter IV. One retroreflector is replaced by a mirror such that the two reflected beams are mirror images of each other. The interference of both beams would thus see a dependence of the fringe visibility perpendicular to the axis of symmetry. If the intensity in both arms are equal, the fringe visibility is equivalent to $g_1(r, -r, \tau)$, assuming a delay time of τ between the two beams. If the retroreflector used only inverts along one spatial axis, r is instead replaced by x or y.

Spatial first-order correlation measurements can be performed with time delay dependence as well. The resulting measurement would thus be dependent on both r and τ. The Fourier transform of this measurement would be the dispersion relationship, not restricted by the spectral resolution of the spectrometer. This would be useful for obtaining momentum information for the 3 fractions found in $g_1(\tau)$ measurements for Chapter IV.

5.1.3 Time-resolved measurements

As discussed in Chapter IV, time-resolved measurements would be needed to confirm if the two fractions with the highest coherence times exist at different times during the pump's duty cycle. Such an experiment could be performed with a streak camera. The streak camera resolves the signal in time by first converting the incident photons to electrons and passing the electrons through a time-dependent voltage sweep. The electrons are thus distributed across a temporal dimension defined along one spatial axis of a CCD camera. Streak cameras are often preceded by a monochromator, and it is thus possible to perform spectral measurements as well.

In an ideal experiment, the goal would be to observe the evolution of the bandwidth of the energy states confined within the optically-induced ring trap. A reduction in the order of magnitude of the linewidth could indicate the binding of free vortices as the condensate evolves into its equilibrium state. However, streak cameras also face limitations on spectral resolution and temporal resolution. It is thus unclear if such measurements would yield any useful information. It may be more useful to forego the spectral measurements and instead examine the time evolution of the spatial distribution of the energy states. The higher order states cover the entire span of the ring trap, while the lower energy states occupy a position near the bottom of the potential well. The evolution of the spatial distribution could thus give clues as to how the energy states may evolve in time. This could also be complemented with tomographical scans of spectrometer measurements as described in Section 5.1.1.

5.2 Future work for vortex-detection experiments

Despite the efficacy of the CoMMZI, vortex detection still remains a very challenging endeavour. In this section, I will discuss the obstacles in the way of a successful detection of spontaneous vortices in a single-shot condensate. I will then propose

strategies and equipment that could address such issues.

Even though the CoMMZI could in principle detect vortices with a low number of photons, the equipment required needs to be able to detect this low number. Electron Multiplying Charged Coupled Devices (EMCCDs) have proven to be viable candidates for observing polariton PL with a low number of photons, as shown by [102, 127]. However, the filamentation of the condensate shown in [102] for more negative detuning may compromise the overall visibility and thus impede the CoMMZI's efficacy. The more homogeneous profiles at more positive detuning would have less of an issue, but vortices at such detunings are more likely to combine early in the condensate's lifetime, which would lead to an overall homogeneous phase. It thus becomes a matter of optimization when finding the right detuning. If a more negative detuning position is desired, the spatial filtering technique discussed in Chapter III could be used to sample a more homogeneous position of the condensate.

The presence of optically-induced Orbital Angular Momentum (OAM) states that may lead to false positives in detection. Such states could be induced unintentionally if the pump has imperfect radial symmetry [138], or they may already exist in a superposition with a net OAM of zero such as in the case of the optically-induced ring trap shown in Chapter III. To avoid such complications, it may be helpful to use a standard Gaussian pump condition but capture the polariton PL at a different location. The goal in this scenario would be to capture the vortices as they move with the polariton flow through the sampling area. To increase the chances of detection, the sampling area could be located at a higher potential than the pump spot, such that the polaritons are moving at a slower speed due to the loss of kinetic energy [119]. A comparison between single-shot and continuous-wave (CW) pump conditions could also be done to identify OAM states that form under both conditions.

Time-resolved experiments for vortex detection could be complemented with time-resolved experiments described in the previous section. Such experiments could pro-

vide insights into the role of vortices in phase transitions, such as through critical slowing in the presence of topological defects [139]. However, the low number of photons would once again be a detriment, and the problem would be made worse by the extremely low quantum efficiency (QE) of the streak camera's photocathode. For the wavelength of PL observed, the photocathode of the Hamamatsu streak camera would only have a QE of 2%. Not only would that increase the photon number requirement discussed in Chapter III, it would also lead to more false positive or false negative detections. Until more efficient photocathodes become available, a possible workaround would be to examine samples with a range of detunings. More negative detuning samples would allow observations earlier in the thermalization process. If this approach is taken, caution must be exercised in drawing conclusions as quantities that could affect vortex behavior, such as the healing length and interaction strength, are different for different detunings.

A test of single-shot capabilities that could be done prior to testing with samples like GaAs would be to use more disordered samples like CdTe. Due to lattice mismatch, CdTe samples have more surface defects and are it is thus more likely for spontaneously formed vortices to exhibit deterministic behavior, as shown in [23, 22]. Standard pump conditions, such as with a Gaussian profile, could be used to ensure angular momentum states would not be induced by the pump. While the vortices may exhibit deterministic behavior, this behavior is not controlled by the experimenter. It would thus be a test of the CoMMZI in detecting vortices travelling through uncontrolled paths. Another alternative woud be to consider using shorter lifetime samples for a larger polariton decay rate and hence the number of photons carrying an average vortex phase. The downside of using shorter lifetime samples would be that we may not catch behavior expected for samples in equilibrium, such as the BKT transition in which vortices would become bounded. The short lifetime would also make it difficult for polaritons to propagate far from the pump spot if such configurations were

desired.

5.3 Summary and Conclusion

In this thesis, I have discussed the development and testing of the Compact Mirroring Mach-Zehnder Interferometer, an interferometer which could detect vortices in polariton PL with a low number of photons. I have then discussed simulation results on the minimum photon number requirement for detecting vortices given various scenarios of vortex behavior, then discussed spectrometric and temporal first-order correlation measurements for a polariton system within an optically-induced ring trap. I have shown that the CoMMZI can detect orbital angular momentum states with polariton systems, and shown that it is possible to detect vortices with photon numbers as low as ~ 10. The $g_1(\tau)$ results show the existance of three fractions at highest pump power, with coherence times spanning nearly three orders of magnitude. Time-resolved experiments could be use to determine if these fractions coexist during the duty cycle of the pump and if this is evidence for prethermalization.

The detection of spontaneous quantum vortices in a single realization of a polariton condensate is challenging, but would be a significant milestone for phase transition studies in polariton systems. With the powerful potential applications of polaritons, such studies would undoubtedly be useful for further understanding how such systems acquire coherence. As of now, EMCCD cameras used to capture signals time-integrated over a single realization appear to be the most viable candidate, due to their ability to detect very low photon numbers. Time-resolved experiments could be performed with streak cameras of improved quantum efficiency.

APPENDICES

APPENDIX A

Appendix for "Testing of the Compact Mirroring Mach-Zehnder Interferometer"

A.1 The small and large prism of the CoMMZI

In this section, I show the parameters used for the large and small prism of the CoMMZI and explain how these parameters were calculated.

Figure A.1 shows the parameters of the large prism and Figure A.2 shows the parameters of the small prism.

The schematic used to calculate these dimensions are given in Figure A.3. The angle β was first fixed to 50 degrees, making it larger than the critical angle for BK7, with a refractive index of 1.5 (41.8 degrees). Using symmetry constraints, α can be calculated using

$$180 - \alpha = \alpha + \beta\alpha = 90 - \frac{\beta}{2}. \tag{A.1}$$

With $\beta = 50$ degrees, α would be 65 degrees. If we assume that the beam enters

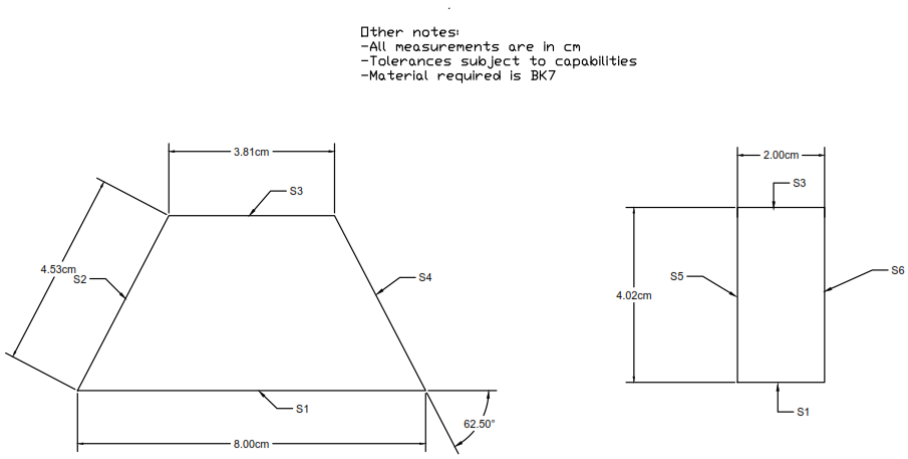

Figure A.1: Parameters of the large prism used in the CoMMZI

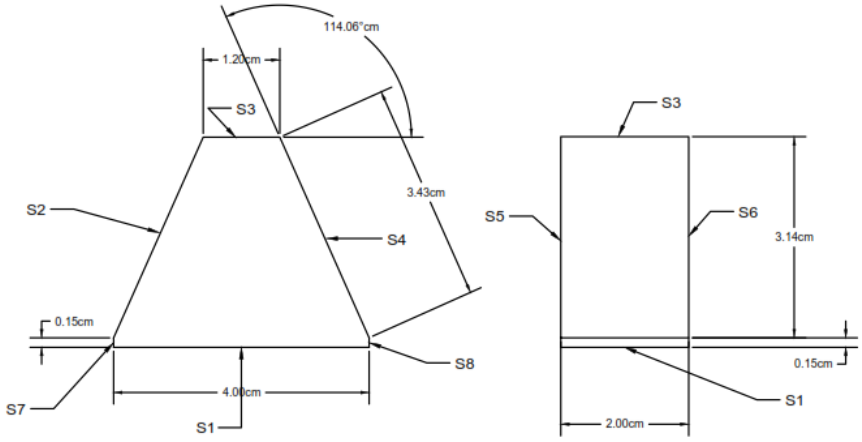

Figure A.2: Parameters of the small prism used in the CoMMZI

1cm from the left edge of the large prism, and that the length L_{large} of the large prism is 8cm long, the path length of the beam and the height of the prism can then be calculated. The path length inside the large prism is calculated to be 12.12cm.

The small prism is more complicated to calculate, due to the constraints of both path length and symmetry. α is first related to x through its relationship with β via Equation A.1. This gives:

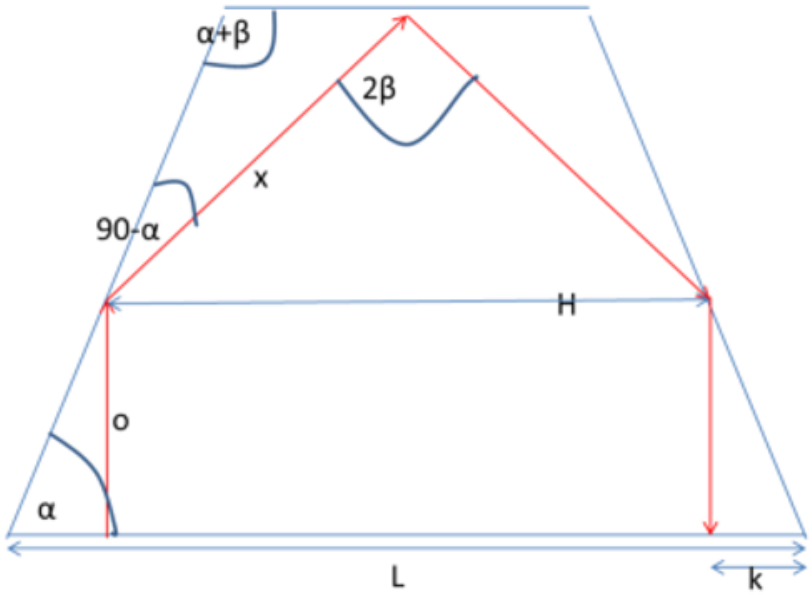

Figure A.3: Schematic used to calculate parameters for CoMMZI

$$\begin{aligned} \sin\beta &= \frac{\frac{L_{small}}{2} - k}{x}, \\ \sin(180 - 2\alpha) &= \frac{\frac{L_{small}}{2} - k}{x}, \\ \sin(2\alpha) &= \frac{\frac{L_{small}}{2} - k}{x}, \end{aligned} \tag{A.2}$$

where L_{small} is the length of the base of the small prism. The total path length inside the small prism is then constrained to match the path length of the large prism. This results in the constraint on x to make it $x = p - k\tan\alpha$, where p is the path length inside the small prism. Substituting this value of x into Equation A.2, the following equation is obtained:

$$p\sin 2\alpha - k\tan\alpha\sin 2\alpha = \frac{L_{small}}{2} - k \tag{A.3}$$

Letting L_{small} be 4cm and thus k = 1cm, a value of 68.8 degrees for α was obtained. β is thus 42.4 degrees, larger than the critical angle.

A.2 Computer Generated Holograms and phase profiles extracted with the Fringe Demodulation method

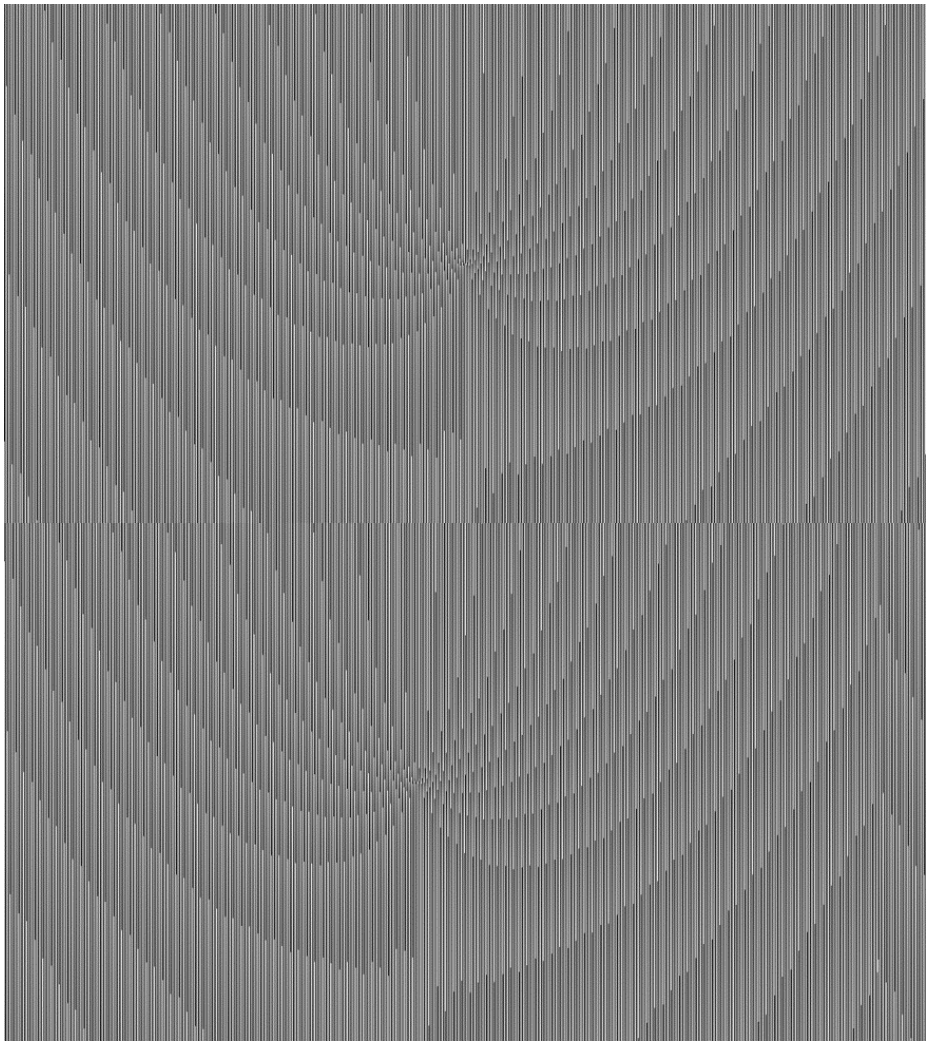

Figure A.4: Computer Generated Holograms for an on-centered l=1 vortex (top) and an off-centered l=1 vortex (bottom)

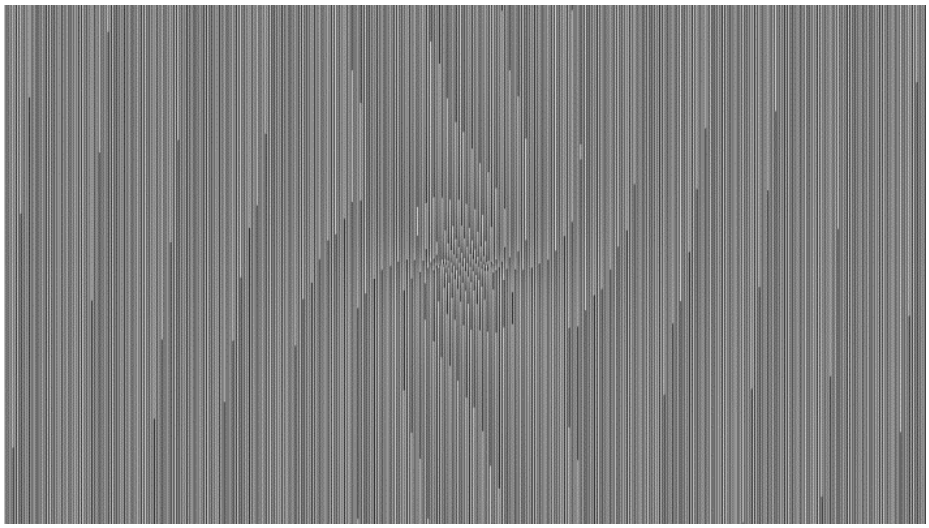

Figure A.5: Computer Generated Holograms for a vortex-antivortex pair with a core separation of 0.4mm

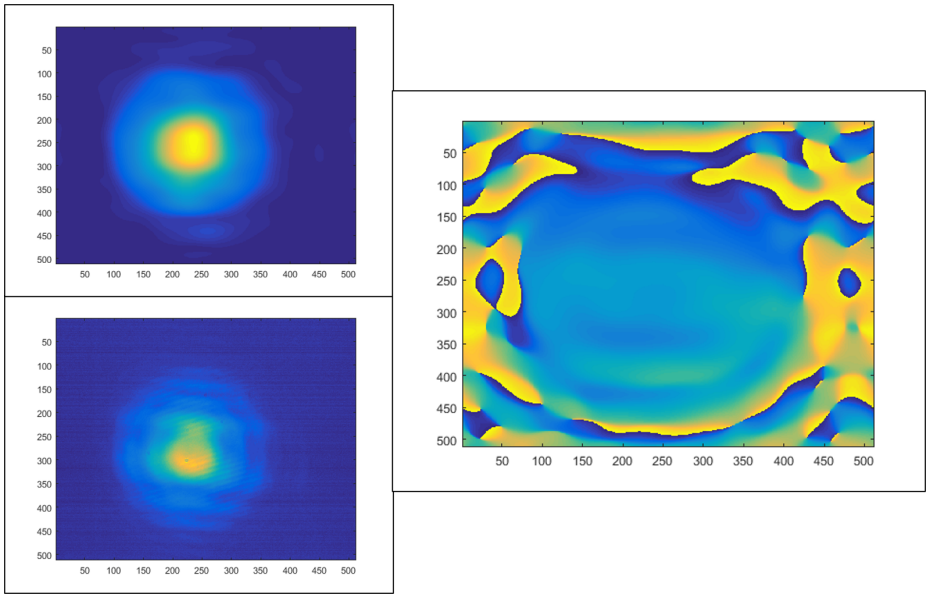

Figure A.6: Intensity profile (top left) and phase profile (right) extracted for a Gaussian beam interfering with another Gaussian beam. The original intensity profile is shown on the bottom left. The extracted intensity profile is the product of two Gaussian profiles, and thus does not resemble the original.

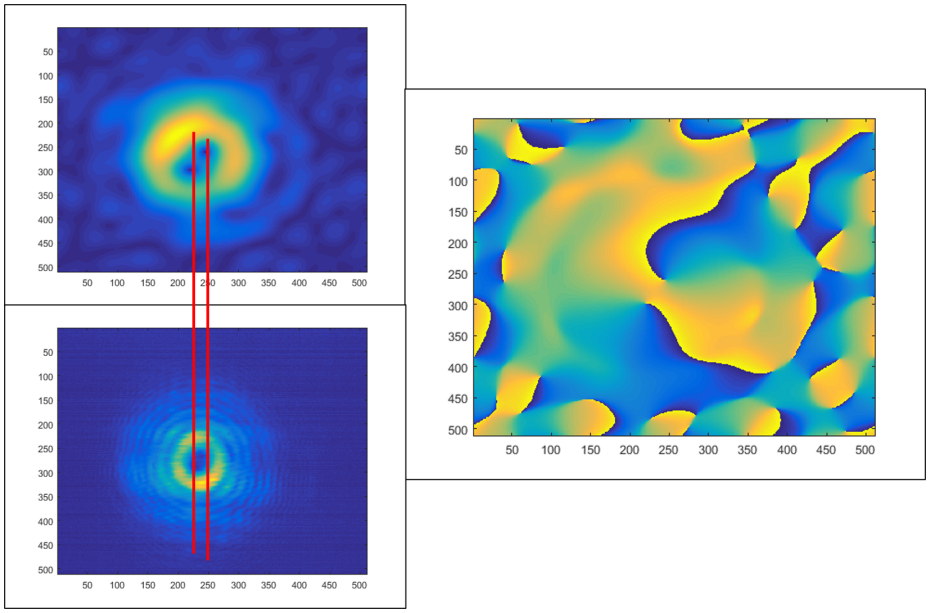

Figure A.7: Intensity profile (top left) and phase profile (right) extracted for a l=2 beam interfering with a Gaussian beam. The original intensity profile is shown on the bottom left. The extracted intensity profile is the product of the two beam profiles, and thus does not resemble the original.

APPENDIX B

Appendix for "Multi-fluid behavior for polaritons in an optically-induced ring pump"

In this Appendix, we show data for polariton photoluminescence (PL) experiments done with an optically-induced ring pump at a position with -10.5meV detuning. The diameter of the ring pump was $50\mu m$, just as with the -8.4meV data set presented in Chapter 4.

B.1 Spectrometer data for -10.5meV detuning using an optically-induced ring pump

Figure B.1 shows the evolution of the polariton population and fraction with pump power for -10.5meV detuning, 2meV more negative than the -8.4meV data presented in Chapter 4. The main difference between these two data sets is the second threshold occuring at 170mW instead of 120mW, and the drop in ground state fraction above 250mW is not observed. The first threshold occurs at 50mW, just as with the -8.4meV detuning data.

Figure B.2 shows the spectrometer images at various pump powers for -10.5meV detuning. We were able to reach a higher power than for the -8.4meV detuning data,

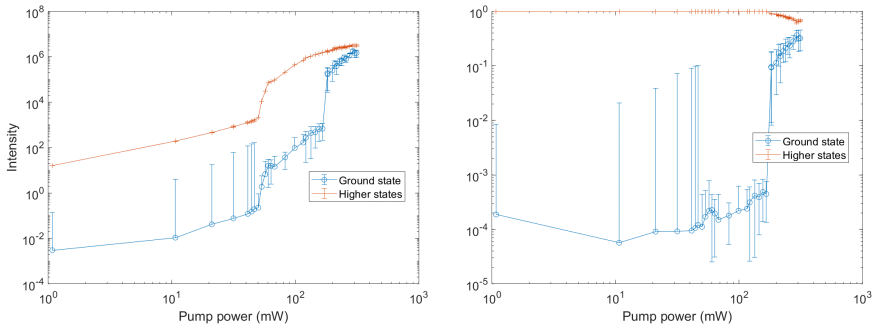

Figure B.1: Evolution of polariton population and fraction with pump power for -10.5meV detuning

at 313mW. However, a faint parabolic dispersion could still be observed, a result of less effective scattering due to decreased interactions.

Figure B.3 shows the evolution of the bandwidth with pump power. The method of calculating the bandwidth is the same as for -8.4meV, with the limits of the bandwidth set at when the population drops to 0.05 times the maximum value. Unlike for -8.4meV, there is no second dip at intermediate powers. The bandwidth also remains consistently above the spectral resolution of 0.1meV.

Figure B.4 shows the energy with the highest population value at different pump powers relative to the value at 1mW. The drop from 1mw to 30mW is 1.5meV greater, and is a result of the more parabolic dispersion at a more negative detuning.

B.2 $|g_1(\tau)|$ data for -10.5meV detuning using an optically-induced ring pump

Figure B.5 shows the $g_1(\tau)$ results for 6 different pump powers taken at -10.5meV detuning. The fit to a sum of a Gaussian and Exponential, given as

$$a * \exp(-\frac{\tau - t_0}{\tau_{c1}}) + (1-a)\exp(-\frac{|\tau| - t_0}{\tau_{c2}}), \tag{B.1}$$

was used for 32mW (**a**), 204mW (**d**), 277mW (**e**) and 300mW (**f**). A Gaussian

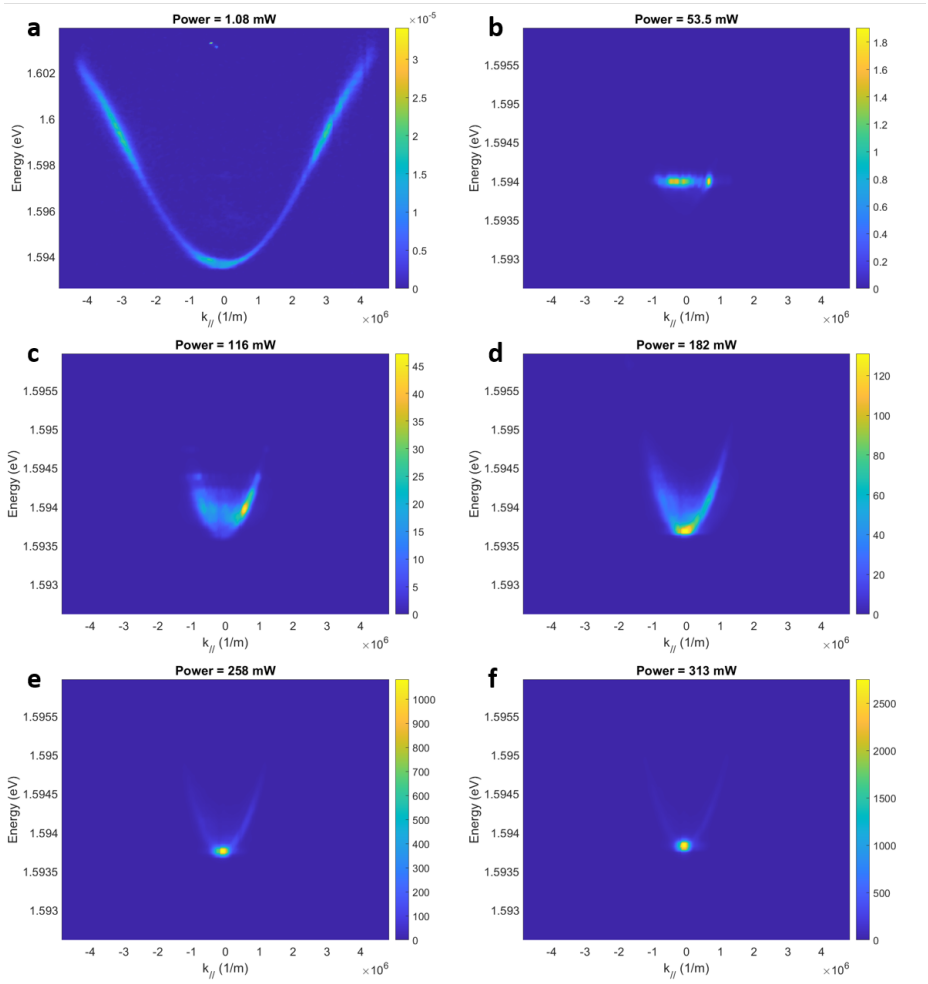

Figure B.2: Spectrometer images for various pump powers for -10.5meV detuning

fit was used for 157mW (**c**), and no fit was done for 57mW (**b**). The fit to 32mW was poor with an error 7 orders of magnitude higher than the fit result, and thus would not be presented here. The regular coherence revivals at 57mW indicates the presence of 2 narrow band energy states. The period of 50ps indicates that these energy states are 0.08meV apart in energy.

Table B.2 shows the results of Gaussian and Exponential fitting at the relevant pump powers.

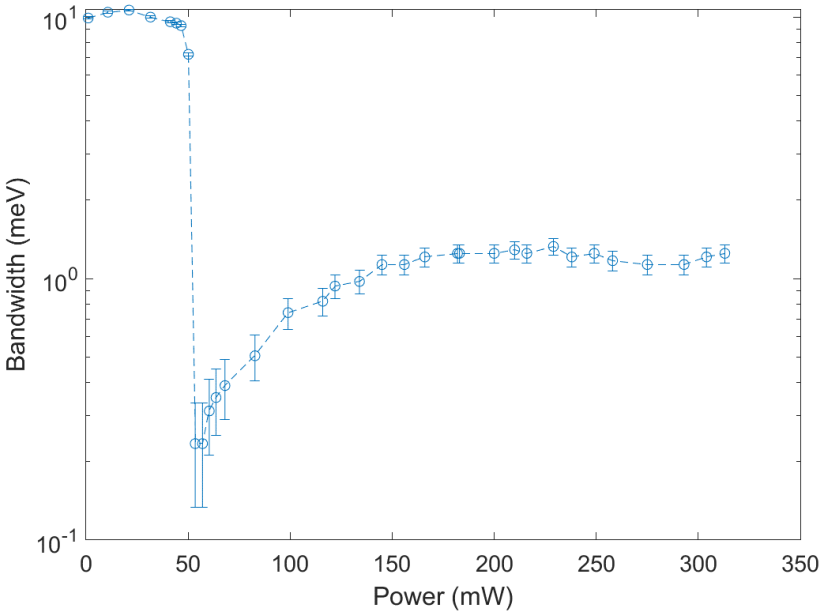

Figure B.3: Evolution of bandwidth with pump power for -10.5meV detuning

Power (mW)	Fraction a	τ_{c1} (ps)	τ_{c2} (ps)
204	0.74 ± 0.02	2.7 ± 0.2	180 ± 40
277	0.430 ± 0.008	1.7 ± 0.2	220 ± 10
300	0.417 ± 0.008	1.6 ± 0.2	230 ± 10

Table B.1: Table of fitting results for Gaussian and Exponential fits to $|g_1(\tau)|$

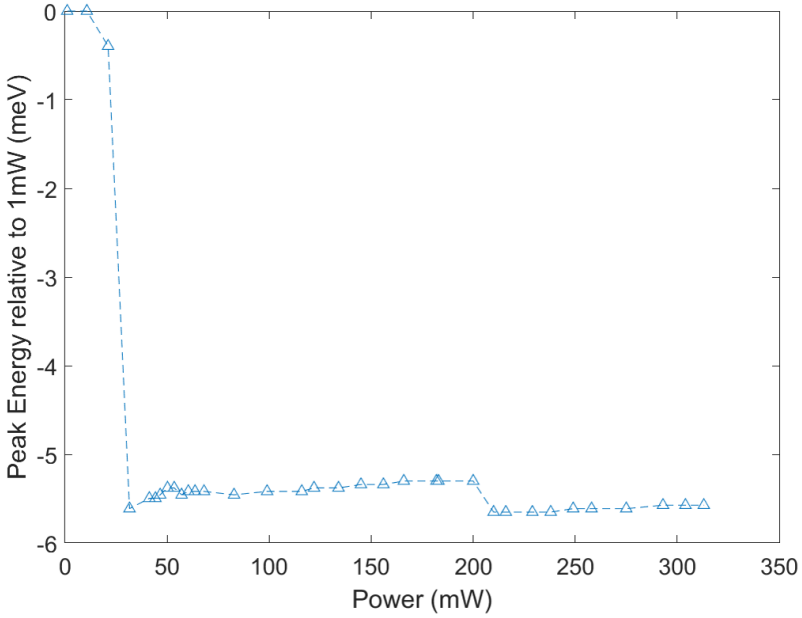

Figure B.4: Evolution of energy with peak population with pump power for -10.5meV detuning

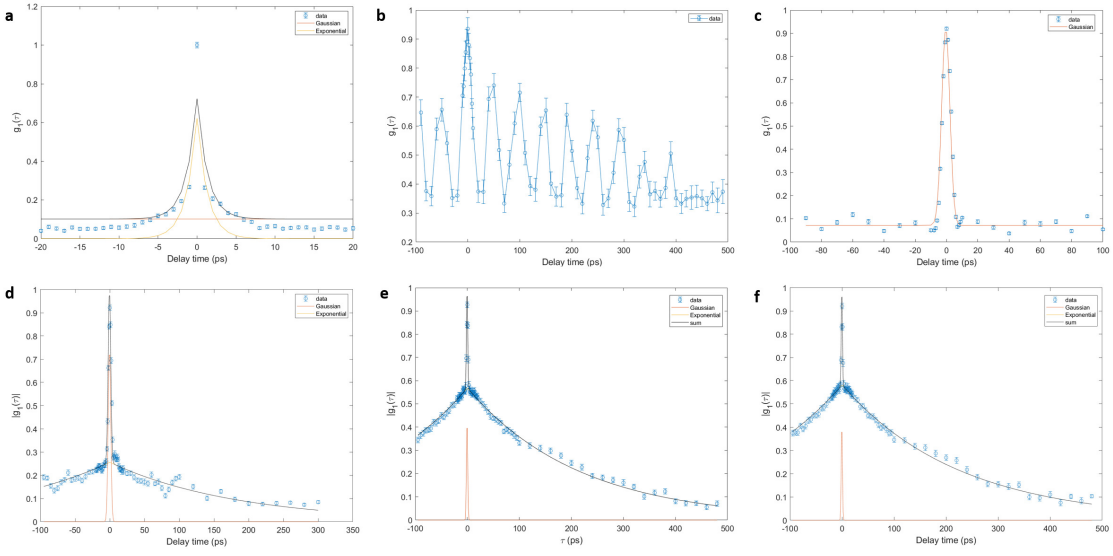

Figure B.5: $g_1(\tau)$ results for 32mW (**a**), 57mW (**b**), 157mW (**c**), 204mW (**d**), 277mW (**e**) and 300mW (**f**)

BIBLIOGRAPHY

BIBLIOGRAPHY

[1] P. R. Berman. Cavity quantum electrodynamics. 1994.

[2] Herbert Walther, Benjamin T H Varcoe, Berthold-Georg Englert, and Thomas Becker. Cavity quantum electrodynamics. *Reports on Progress in Physics*, 69(5):1325–1382, May 2006.

[3] Tim Byrnes, Na Young Kim, and Yoshihisa Yamamoto. Exciton–polariton condensates. *Nature Physics*, 10(11):803–813, November 2014.

[4] Hui Deng, Hartmut Haug, and Yoshihisa Yamamoto. Exciton-polariton Bose-Einstein condensation. *Reviews of Modern Physics*, 82(2):1489–1537, May 2010.

[5] S. Christopoulos, G. Baldassarri Höger von Högersthal, A. J. D. Grundy, P. G. Lagoudakis, A. V. Kavokin, J. J. Baumberg, G. Christmann, R. Butté, E. Feltin, J.-F. Carlin, and N. Grandjean. Room-Temperature Polariton Lasing in Semiconductor Microcavities. *Physical Review Letters*, 98(12):126405, March 2007.

[6] Ayan Das, Pallab Bhattacharya, Junseok Heo, Animesh Banerjee, and Wei Guo. Polariton Bose–Einstein condensate at room temperature in an Al(Ga)N nanowire–dielectric microcavity with a spatial potential trap. *Proceedings of the National Academy of Sciences*, 110(8):2735–2740, February 2013.

[7] S. Kéna-Cohen and S. R. Forrest. Room-temperature polariton lasing in an organic single-crystal microcavity. *Nature Photonics*, 4(6):371–375, June 2010.

[8] C. Schneider, K. Winkler, M. D. Fraser, M. Kamp, Y. Yamamoto, E. A. Ostrovskaya, and S. Höfling. Exciton-polariton trapping and potential landscape engineering. *Reports on Progress in Physics*, 80(1):016503, November 2016.

[9] Zhaorong Wang, Bo Zhang, and Hui Deng. Dispersion engineering for vertical microcavities using subwavelength gratings. *Physical review letters*, 114(7):073601, 2015.

[10] T. Jacqmin, I. Carusotto, I. Sagnes, M. Abbarchi, D. D. Solnyshkov, G. Malpuech, E. Galopin, A. Lemaître, J. Bloch, and A. Amo. Direct Observation of Dirac Cones and a Flatband in a Honeycomb Lattice for Polaritons. *Physical Review Letters*, 112(11):116402, March 2014.

[11] Na Young Kim, Kenichiro Kusudo, Congjun Wu, Naoyuki Masumoto, Andreas Löffler, Sven Höfling, Norio Kumada, Lukas Worschech, Alfred Forchel, and Yoshihisa Yamamoto. Dynamical d-wave condensation of exciton–polaritons in a two-dimensional square-lattice potential. *Nature Physics*, 7(9):681–686, September 2011.

[12] Naoyuki Masumoto, Na Young Kim, Tim Byrnes, Kenichiro Kusudo, Andreas Löffler, Sven Höfling, Alfred Forchel, and Yoshihisa Yamamoto. Exciton–polariton condensates with flat bands in a two-dimensional kagome lattice. *New Journal of Physics*, 14(6):065002, June 2012.

[13] Sanjib Ghosh and Timothy C. H. Liew. Quantum computing with exciton-polariton condensates. *npj Quantum Information*, 6(1):16, December 2020.

[14] M. H. Anderson, J. R. Ensher, M. R. Matthews, C. E. Wieman, and E. A. Cornell. Observation of Bose-Einstein Condensation in a Dilute Atomic Vapor. *Science*, 269(5221):198–201, July 1995.

[15] Hui Deng, Gregor Weihs, Charles Santori, Jacqueline Bloch, and Yoshihisa Yamamoto. Condensation of Semiconductor Microcavity Exciton Polaritons. *Science*, 298(5591):199–202, October 2002.

[16] J. Kasprzak, M. Richard, S. Kundermann, A. Baas, P. Jeambrun, J. M. J. Keeling, F. M. Marchetti, M. H. Szymańska, R. André, J. L. Staehli, V. Savona, P. B. Littlewood, B. Deveaud, and Le Si Dang. Bose–Einstein condensation of exciton polaritons. *Nature*, 443(7110):409–414, September 2006.

[17] Wolfgang H. Nitsche, Na Young Kim, Georgios Roumpos, Christian Schneider, Martin Kamp, Sven Höfling, Alfred Forchel, and Yoshihisa Yamamoto. Algebraic order and the Berezinskii-Kosterlitz-Thouless transition in an exciton-polariton gas. *Physical Review B*, 90(20):205430, November 2014.

[18] Georgios Roumpos, Michael Lohse, Wolfgang H. Nitsche, Jonathan Keeling, Marzena Hanna Szymańska, Peter B. Littlewood, Andreas Löffler, Sven Höfling, Lukas Worschech, Alfred Forchel, and Yoshihisa Yamamoto. Power-law decay of the spatial correlation function in exciton-polariton condensates. *Proceedings of the National Academy of Sciences*, 109(17):6467–6472, April 2012.

[19] Tim Byrnes, Tomoyuki Horikiri, Natsuko Ishida, Michael Fraser, and Yoshihisa Yamamoto. Negative Bogoliubov dispersion in exciton-polariton condensates. *Physical Review B*, 85(7):075130, February 2012.

[20] S. Utsunomiya, L. Tian, G. Roumpos, C. W. Lai, N. Kumada, T. Fujisawa, M. Kuwata-Gonokami, A. Löffler, S. Höfling, A. Forchel, and Y. Yamamoto. Observation of Bogoliubov excitations in exciton-polariton condensates. *Nature Physics*, 4(9):700–705, September 2008.

[21] N. Takemura, S. Trebaol, M. Wouters, M. T. Portella-Oberli, and B. Deveaud. Polaritonic Feshbach resonance. *Nature Physics*, 10(7):500–504, July 2014.

[22] K. G. Lagoudakis, F. Manni, B. Pietka, M. Wouters, T. C. H. Liew, V. Savona, A. V. Kavokin, R. André, and B. Deveaud-Plédran. Probing the Dynamics of Spontaneous Quantum Vortices in Polariton Superfluids. *Physical Review Letters*, 106(11):115301, March 2011.

[23] K. G. Lagoudakis, M. Wouters, M. Richard, A. Baas, I. Carusotto, R. André, Le Si Dang, and B. Deveaud-Plédran. Quantized vortices in an exciton–polariton condensate. *Nature Physics*, 4(9):706–710, September 2008.

[24] T. W. B. Kibble. Topology of cosmic domains and strings. *Journal of Physics A: Mathematical and General*, 9(8):1387, 1976.

[25] W. H. Zurek. Cosmological experiments in condensed matter systems. *Physics Reports*, 276(4):177–221, November 1996.

[26] Georgios Roumpos, Michael D. Fraser, Andreas Löffler, Sven Höfling, Alfred Forchel, and Yoshihisa Yamamoto. Single vortex-antivortex pair in an exciton-polariton condensate. *Nature Physics*, 7(2):129–133, February 2011.

[27] Robert Dall, Michael D. Fraser, Anton S. Desyatnikov, Guangyao Li, Sebastian Brodbeck, Martin Kamp, Christian Schneider, Sven Höfling, and Elena A. Ostrovskaya. Creation of Orbital Angular Momentum States with Chiral Polaritonic Lenses. *Physical Review Letters*, 113(20):200404, November 2014.

[28] D. N. Krizhanovskii, D. M. Whittaker, R. A. Bradley, K. Guda, D. Sarkar, D. Sanvitto, L. Vina, E. Cerda, P. Santos, K. Biermann, R. Hey, and M. S. Skolnick. Effect of Interactions on Vortices in a Nonequilibrium Polariton Condensate. *Physical Review Letters*, 104(12):126402, March 2010.

[29] J. J. Hopfield. Theory of the Contribution of Excitons to the Complex Dielectric Constant of Crystals. *Physical Review*, 112(5):1555–1567, December 1958.

[30] L. Bányai, P. Gartner, O. M. Schmitt, and H. Haug. Condensation kinetics for bosonic excitons interacting with a thermal phonon bath. *Physical Review B*, 61(13):8823–8834, April 2000.

[31] D. B. Tran Thoai and H. Haug. Ortho-exciton polariton relaxation by phonon scattering in Cu2O. *Solid State Communications*, 115(7):379–382, July 2000.

[32] L. Banyai and P. Gartner. Real-Time Bose-Einstein Condensation in a Finite Volume with a Discrete Spectrum. *Physical Review Letters*, 88(21):210404, May 2002.

[33] F. Tassone, C. Piermarocchi, V. Savona, A. Quattropani, and P. Schwendimann. Photoluminescence decay times in strong-coupling semiconductor microcavities. *Physical Review B*, 53(12):R7642–R7645, March 1996.

[34] F. Tassone, C. Piermarocchi, V. Savona, A. Quattropani, and P. Schwendimann. Bottleneck effects in the relaxation and photoluminescence of microcavity polaritons. *Physical Review B*, 56(12):7554–7563, September 1997.

[35] F. Tassone and Y. Yamamoto. Exciton-exciton scattering dynamics in a semiconductor microcavity and stimulated scattering into polaritons. *Physical Review B*, 59(16):10830–10842, April 1999.

[36] J. Bloch and J. Y. Marzin. Photoluminescence dynamics of cavity polaritons under resonant excitation in the picosecond range. *Physical Review B*, 56(4):2103–2108, July 1997.

[37] Huy Thien Cao, T. D. Doan, D. B. Tran Thoai, and H. Haug. Condensation kinetics of cavity polaritons interacting with a thermal phonon bath. *Physical Review B*, 69(24):245325, June 2004.

[38] T. D. Doan, Huy Thien Cao, D. B. Tran Thoai, and H. Haug. Condensation kinetics of microcavity polaritons with scattering by phonons and polaritons. *Physical Review B*, 72(8):085301, August 2005.

[39] A Imamog, RJ Ram, S Pau, Y Yamamoto, et al. Nonequilibrium condensates and lasers without inversion: Exciton-polariton lasers. *Physical Review A*, 53(6):4250, 1996.

[40] P. C. Hohenberg. Existence of Long-Range Order in One and Two Dimensions. *Physical Review*, 158(2):383–386, June 1967.

[41] N. D. Mermin and H. Wagner. Absence of Ferromagnetism or Antiferromagnetism in One- or Two-Dimensional Isotropic Heisenberg Models. *Physical Review Letters*, 17(22):1133–1136, November 1966.

[42] David R. Nelson and J. M. Kosterlitz. Universal Jump in the Superfluid Density of Two-Dimensional Superfluids. *Physical Review Letters*, 39(19):1201–1205, November 1977.

[43] J. M. Kosterlitz and D. J. Thouless. Ordering, metastability and phase transitions in two-dimensional systems. *Journal of Physics C: Solid State Physics*, 6(7):1181, 1973.

[44] Richard J. Fletcher, Martin Robert-de-Saint-Vincent, Jay Man, Nir Navon, Robert P. Smith, Konrad Viebahn, and Zoran Hadzibabic. Unification of BKT and BEC Phase Transitions in a Trapped Two-Dimensional Bose Gas. *arXiv:1501.02262 [cond-mat, physics:physics, physics:quant-ph]*, January 2015.

[45] Yijie Shen, Xuejiao Wang, Zhenwei Xie, Changjun Min, Xing Fu, Qiang Liu, Mali Gong, and Xiaocong Yuan. Optical vortices 30 years on: OAM manipulation from topological charge to multiple singularities. *Light: Science & Applications*, 8(1):90, December 2019.

[46] L. Allen, M. W. Beijersbergen, R. J. C. Spreeuw, and J. P. Woerdman. Orbital angular momentum of light and the transformation of Laguerre-Gaussian laser modes. *Physical Review A*, 45(11):8185–8189, June 1992.

[47] Ward Brullot, Maarten K. Vanbel, Tom Swusten, and Thierry Verbiest. Resolving enantiomers using the optical angular momentum of twisted light. *Science Advances*, 2(3):e1501349, March 2016.

[48] David G. Grier. A revolution in optical manipulation. *Nature*, 424(6950):810–816, August 2003.

[49] S. B. Wang and C. T. Chan. Lateral optical force on chiral particles near a surface. *Nature Communications*, 5(1):3307, May 2014.

[50] Yang Zhao, Amir N. Askarpour, Liuyang Sun, Jinwei Shi, Xiaoqin Li, and Andrea Alù. Chirality detection of enantiomers using twisted optical metamaterials. *Nature Communications*, 8(1):14180, April 2017.

[51] Gregory Foo, David M. Palacios, and Grover A. Swartzlander. Optical vortex coronagraph. *Optics Letters*, 30(24):3308–3310, December 2005.

[52] Martin Harwit. Photon Orbital Angular Momentum in Astrophysics. *The Astrophysical Journal*, 597(2):1266, November 2003.

[53] Jae Hoon Lee, Gregory Foo, Eric G. Johnson, and Grover A. Swartzlander. Experimental Verification of an Optical Vortex Coronagraph. *Physical Review Letters*, 97(5):053901, August 2006.

[54] Grover A. Swartzlander, Erin L. Ford, Rukiah S. Abdul-Malik, Laird M. Close, Mary Anne Peters, David M. Palacios, and Daniel W. Wilson. Astronomical demonstration of an optical vortex coronagraph. *Optics Express*, 16(14):10200–10207, July 2008.

[55] Fabrizio Tamburini, Bo Thidé, Gabriel Molina-Terriza, and Gabriele Anzolin. Twisting of light around rotating black holes. *Nature Physics*, 7(3):195–197, March 2011.

[56] Julio T. Barreiro, Tzu-Chieh Wei, and Paul G. Kwiat. Beating the channel capacity limit for linear photonic superdense coding. *Nature Physics*, 4(4):282–286, April 2008.

[57] P. Jia, Y. Yang, C. J. Min, H. Fang, and X.-C. Yuan. Sidelobe-modulated optical vortices for free-space communication. *Optics Letters*, 38(4):588–590, February 2013.

[58] Long Li, Runzhou Zhang, Zhe Zhao, Guodong Xie, Peicheng Liao, Kai Pang, Haoqian Song, Cong Liu, Yongxiong Ren, Guillaume Labroille, Pu Jian, Dmitry Starodubov, Brittany Lynn, Robert Bock, Moshe Tur, and Alan E. Willner.

High-Capacity Free-Space Optical Communications Between a Ground Transmitter and a Ground Receiver via a UAV Using Multiplexing of Multiple Orbital-Angular-Momentum Beams. *Scientific Reports*, 7(1):1–12, December 2017.

[59] Jian Wang, Jeng-Yuan Yang, Irfan M. Fazal, Nisar Ahmed, Yan Yan, Hao Huang, Yongxiong Ren, Yang Yue, Samuel Dolinar, Moshe Tur, and Alan E. Willner. Terabit free-space data transmission employing orbital angular momentum multiplexing. *Nature Photonics*, 6(7):488–496, July 2012.

[60] A. E. Willner, H. Huang, Y. Yan, Y. Ren, N. Ahmed, G. Xie, C. Bao, L. Li, Y. Cao, Z. Zhao, J. Wang, M. P. J. Lavery, M. Tur, S. Ramachandran, A. F. Molisch, N. Ashrafi, and S. Ashrafi. Optical communications using orbital angular momentum beams. *Advances in Optics and Photonics*, 7(1):66–106, March 2015.

[61] Yan Yan, Guodong Xie, Martin P. J. Lavery, Hao Huang, Nisar Ahmed, Changjing Bao, Yongxiong Ren, Yinwen Cao, Long Li, Zhe Zhao, Andreas F. Molisch, Moshe Tur, Miles J. Padgett, and Alan E. Willner. High-capacity millimetre-wave communications with orbital angular momentum multiplexing. *Nature Communications*, 5(1):4876, December 2014.

[62] I. Chuang, R. Durrer, N. Turok, and B. Yurke. Cosmology in the laboratory: Defect dynamics in liquid crystals. *Science (New York, N.Y.)*, 251(4999):1336–1342, March 1991.

[63] P. C. Hendry, N. S. Lawson, R. a. M. Lee, P. V. E. McClintock, and C. D. H. Williams. Generation of defects in superfluid 4 He as an analogue of the formation of cosmic strings. *Nature*, 368(6469):315–317, March 1994.

[64] Adolfo del Campo and Wojciech H. Zurek. Universality of phase transition dynamics: Topological defects from symmetry breaking. *International Journal of Modern Physics A*, 29(08):1430018, March 2014.

[65] T.W.B Kibble and G.R Pickett. Introduction. Cosmology meets condensed matter. *Philosophical Transactions of the Royal Society A: Mathematical, Physical and Engineering Sciences*, 366(1877):2793–2802, August 2008.

[66] Asja Jelić and Leticia F. Cugliandolo. Quench dynamics of the 2dXYmodel. *Journal of Statistical Mechanics: Theory and Experiment*, 2011(02):P02032, February 2011.

[67] Pablo Laguna and Wojciech Hubert Zurek. Density of Kinks after a Quench: When Symmetry Breaks, How Big are the Pieces? *Physical Review Letters*, 78(13):2519–2522, March 1997.

[68] Minchul Lee, Seungju Han, and Mahn-Soo Choi. Kibble-Zurek mechanism in a topological phase transition. *Physical Review B*, 92(3):035117, July 2015.

[69] W. H. Zurek. Cosmological experiments in superfluid helium? *Nature*, 317(6037):505–508, October 1985.

[70] Gregory P Bewley, Daniel P Lathrop, and Katepalli R Sreenivasan. Visualization of quantized vortices. *Nature*, 441(7093):588–588, 2006.

[71] Olli V. Lounasmaa and Erkki Thuneberg. Vortices in rotating superfluid 3He. *Proceedings of the National Academy of Sciences*, 96(14):7760–7767, July 1999.

[72] Jérôme Beugnon and Nir Navon. Exploring the Kibble–Zurek mechanism with homogeneous Bose gases. *Journal of Physics B: Atomic, Molecular and Optical Physics*, 50(2):022002, January 2017.

[73] F. Chevy, K. W. Madison, V. Bretin, and J. Dalibard. Interferometric detection of a single vortex in a dilute Bose-Einstein condensate. *Physical Review A*, 64(3):031601, August 2001.

[74] Bogdan Damski and Wojciech H. Zurek. Soliton Creation During a Bose-Einstein Condensation. *Physical Review Letters*, 104(16):160404, April 2010.

[75] M. R. Matthews, B. P. Anderson, P. C. Haljan, D. S. Hall, C. E. Wieman, and E. A. Cornell. Vortices in a Bose-Einstein Condensate. *Physical Review Letters*, 83(13):2498–2501, September 1999.

[76] R. Srinivasan. Vortices in Bose-Einstein condensates: A review of the experimental results. *Pramana*, 66(1):3–30, January 2006.

[77] Chad N. Weiler, Tyler W. Neely, David R. Scherer, Ashton S. Bradley, Matthew J. Davis, and Brian P. Anderson. Spontaneous vortices in the formation of Bose–Einstein condensates. *Nature*, 455(7215):948–951, October 2008.

[78] P. Engels, I. Coddington, P. C. Haljan, and E. A. Cornell. Nonequilibrium Effects of Anisotropic Compression Applied to Vortex Lattices in Bose-Einstein Condensates. *Physical Review Letters*, 89(10):100403, August 2002.

[79] K. W. Madison, F. Chevy, W. Wohlleben, and J. Dalibard. Vortex Formation in a Stirred Bose-Einstein Condensate. *Physical Review Letters*, 84(5):806–809, January 2000.

[80] A. A. Abrikosov. The magnetic properties of superconducting alloys. *Journal of Physics and Chemistry of Solids*, 2(3):199–208, January 1957.

[81] Frederick S. Wells, Alexey V. Pan, X. Renshaw Wang, Sergey A. Fedoseev, and Hans Hilgenkamp. Analysis of low-field isotropic vortex glass containing vortex groups in YBa2Cu3O7-x thin films visualized by scanning SQUID microscopy. *Scientific Reports*, 5, March 2015.

[82] Sumanta Tewari, S. Das Sarma, Chetan Nayak, Chuanwei Zhang, and P. Zoller. Quantum Computation using Vortices and Majorana Zero Modes of a ${p}_{x}+i{p}_{y}$ Superfluid of Fermionic Cold Atoms. *Physical Review Letters*, 98(1):010506, January 2007.

[83] R. P. Feynman. Chapter II Application of Quantum Mechanics to Liquid Helium. In C. J. Gorter, editor, *Progress in Low Temperature Physics*, volume 1, pages 17–53. Elsevier, January 1955.

[84] A Yu Vasiliev, A E Tarkhov, L I Menshikov, P O Fedichev, and Uwe R Fischer. Universality of the Berezinskii–Kosterlitz–Thouless type of phase transition in the dipolar XY-model. *New Journal of Physics*, 16(5):053011, May 2014.

[85] T. C. H. Liew, O. A. Egorov, M. Matuszewski, O. Kyriienko, X. Ma, and E. A. Ostrovskaya. Instability-induced formation and nonequilibrium dynamics of phase defects in polariton condensates. *Physical Review B*, 91(8):085413, February 2015.

[86] Jonathan Leach, Miles J. Padgett, Stephen M. Barnett, Sonja Franke-Arnold, and Johannes Courtial. Measuring the Orbital Angular Momentum of a Single Photon. *Physical Review Letters*, 88(25):257901, June 2002.

[87] Martin P. J. Lavery, Angela Dudley, Andrew Forbes, Johannes Courtial, and Miles J. Padgett. Robust interferometer for the routing of light beams carrying orbital angular momentum. *New Journal of Physics*, 13(9):093014, 2011.

[88] A. Amo, S. Pigeon, D. Sanvitto, V. G. Sala, R. Hivet, I. Carusotto, F. Pisanello, G. Leménager, R. Houdré, E. Giacobino, C. Ciuti, and A. Bramati. Polariton Superfluids Reveal Quantum Hydrodynamic Solitons. *Science*, 332(6034):1167–1170, June 2011.

[89] Gaël Nardin, Gabriele Grosso, Yoan Léger, Barbara Pięt̨ka, François Morier-Genoud, and Benoît Deveaud-Plédran. Hydrodynamic nucleation of quantized vortex pairs in a polariton quantum fluid. *Nature Physics*, 7(8):635–641, August 2011.

[90] D. Sanvitto, S. Pigeon, A. Amo, D. Ballarini, M. De Giorgi, I. Carusotto, R. Hivet, F. Pisanello, V. G. Sala, P. S. S. Guimaraes, R. Houdré, E. Giacobino, C. Ciuti, A. Bramati, and G. Gigli. All-optical control of the quantum flow of a polariton condensate. *Nature Photonics*, 5(10):610–614, October 2011.

[91] T. Boulier, H. Terças, D. D. Solnyshkov, Q. Glorieux, E. Giacobino, G. Malpuech, and A. Bramati. Vortex Chain in a Resonantly Pumped Polariton Superfluid. *Scientific Reports*, 5:9230, March 2015.

[92] T. Boulier, E. Cancellieri, N.D. Sangouard, Q. Glorieux, A.V. Kavokin, D.M. Whittaker, E. Giacobino, and A. Bramati. Injection of Orbital Angular Momentum and Storage of Quantized Vortices in Polariton Superfluids. *Physical Review Letters*, 116(11):116402, March 2016.

[93] Lorenzo Dominici, Ricardo Carretero-González, Antonio Gianfrate, Jesús Cuevas-Maraver, Augusto S. Rodrigues, Dimitri J. Frantzeskakis, Giovanni Lerario, Dario Ballarini, Milena De Giorgi, Giuseppe Gigli, Panayotis G. Kevrekidis, and Daniele Sanvitto. Interactions and scattering of quantum vortices in a polariton fluid. *Nature Communications*, 9(1):1467, April 2018.

[94] D. Sanvitto, F. M. Marchetti, M. H. Szymańska, G. Tosi, M. Baudisch, F. P. Laussy, D. N. Krizhanovskii, M. S. Skolnick, L. Marrucci, A. Lemaître, J. Bloch, C. Tejedor, and L. Viña. Persistent currents and quantized vortices in a polariton superfluid. *Nature Physics*, 6(7):527–533, July 2010.

[95] F. M. Marchetti, M. H. Szymańska, C. Tejedor, and D. M. Whittaker. Spontaneous and Triggered Vortices in Polariton Optical-Parametric-Oscillator Superfluids. *Physical Review Letters*, 105(6):063902, August 2010.

[96] G. Tosi, F. M. Marchetti, D. Sanvitto, C. Antón, M. H. Szymańska, A. Berceanu, C. Tejedor, L. Marrucci, A. Lemaître, J. Bloch, and L. Viña. Onset and Dynamics of Vortex-Antivortex Pairs in Polariton Optical Parametric Oscillator Superfluids. *Physical Review Letters*, 107(3):036401, July 2011.

[97] C. Antón, G. Tosi, M. D. Martín, L. Viña, A. Lemaître, and J. Bloch. Role of supercurrents on vortices formation in polariton condensates. *Optics Express*, 20(15):16366–16373, July 2012.

[98] H. Sigurdsson, O. A. Egorov, X. Ma, I. A. Shelykh, and T. C. H. Liew. Information processing with topologically protected vortex memories in exciton-polariton condensates. *Physical Review B*, 90(1), July 2014. arXiv: 1403.5047.

[99] Thomas Boulier, Emiliano Cancellieri, Nicolas D. Sangouard, Romain Hivet, Quentin Glorieux, Élisabeth Giacobino, and Alberto Bramati. Lattices of quantized vortices in polariton superfluids. *Comptes Rendus Physique*.

[100] S. Burger, K. Bongs, S. Dettmer, W. Ertmer, K. Sengstock, A. Sanpera, G. V. Shlyapnikov, and M. Lewenstein. Dark Solitons in Bose-Einstein Condensates. *Physical Review Letters*, 83(25):5198–5201, December 1999.

[101] M. D. Fraser, G. Roumpos, and Y. Yamamoto. Vortex-antivortex pair dynamics in an excitonpolariton condensate. *New Journal of Physics*, 11(11):113048, 2009.

[102] E. Estrecho, T. Gao, N. Bobrovska, M. D. Fraser, M. Steger, L. Pfeiffer, K. West, T. C. H. Liew, M. Matuszewski, D. W. Snoke, A. G. Truscott, and E. A. Ostrovskaya. Single-shot condensation of exciton polaritons and the hole burning effect. *Nature Communications*, 9(1):2944, August 2018.

[103] Andrew Forbes, Angela Dudley, and Melanie McLaren. Creation and detection of optical modes with spatial light modulators. *Advances in Optics and Photonics*, 8(2):200–227, June 2016.

[104] Gregorius C. G. Berkhout, Martin P. J. Lavery, Johannes Courtial, Marco W. Beijersbergen, and Miles J. Padgett. Efficient Sorting of Orbital Angular Momentum States of Light. *Physical Review Letters*, 105(15):153601, October 2010.

[105] Yuanhui Wen, Ioannis Chremmos, Yujie Chen, Jiangbo Zhu, Yanfeng Zhang, and Siyuan Yu. Spiral Transformation for High-Resolution and Efficient Sorting of Optical Vortex Modes. *Physical Review Letters*, 120(19):193904, May 2018.

[106] Paul Bierdz, Minho Kwon, Connor Roncaioli, and Hui Deng. High fidelity detection of the orbital angular momentum of light by time mapping. *New Journal of Physics*, 15(11):113062, 2013.

[107] Cheng-Yeh Lee, Chuan-Ching Chang, Chun-Yu Cho, Pi-Hui Tuan, and Yung-Fu Chen. Generation of Higher Order Vortex Beams From a YVO_4/Nd:YVO_4 Self-Raman Laser via Off-Axis Pumping With Mode Converter. *IEEE Journal of Selected Topics in Quantum Electronics*, 21(1):318–322, January 2015.

[108] Filippo Cardano, Ebrahim Karimi, Sergei Slussarenko, Lorenzo Marrucci, Corrado de Lisio, and Enrico Santamato. Polarization pattern of vector vortex beams generated by q-plates with different topological charges. *Applied Optics*, 51(10):C1–C6, April 2012.

[109] Lorenzo Marrucci. The q-plate and its future. *Journal of Nanophotonics*, 7(1):078598, September 2013.

[110] K. Sueda, G. Miyaji, N. Miyanaga, and M. Nakatsuka. Laguerre-Gaussian beam generated with a multilevel spiral phase plate for high intensity laser pulses. In *Conference on Lasers and Electro-Optics*, page JThE2. Optical Society of America, May 2005.

[111] D. Rozas, C. T. Law, and G. A. Swartzlander, Jr. Propagation dynamics of optical vortices. *Journal of the Optical Society of America B*, 14(11):3054, November 1997.

[112] Mark R. Dennis. Rows of optical vortices from elliptically perturbing a high-order beam. *Optics Letters*, 31(9):1325, May 2006.

[113] Salla Gangi Reddy, Chithrabhanu Permangatt, Shashi Prabhakar, Ali Anwar, J Banerji, and RP Singh. Divergence of optical vortex beams. *Applied optics*, 54(22):6690–6693, 2015.

[114] Jeffrey A. Davis, Don M. Cottrell, Juan Campos, María J. Yzuel, and Ignacio Moreno. Encoding amplitude information onto phase-only filters. *Applied Optics*, 38(23):5004, August 1999.

[115] Victor Arrizón, Ulises Ruiz, Rosibel Carrada, and Luis A. González. Pixelated phase computer holograms for the accurate encoding of scalar complex fields. *Journal of the Optical Society of America A*, 24(11):3500, November 2007.

[116] Michiel Wouters and Iacopo Carusotto. Excitations in a nonequilibrium bose-einstein condensate of exciton polaritons. *Physical review letters*, 99(14):140402, 2007.

[117] Davide Caputo, Dario Ballarini, Galbadrakh Dagvadorj, Carlos Sánchez Muñoz, Milena De Giorgi, Lorenzo Dominici, Kenneth West, Loren N. Pfeiffer, Giuseppe Gigli, Fabrice P. Laussy, Marzena H. Szymańska, and Daniele Sanvitto. Topological order and thermal equilibrium in polariton condensates. *Nature Materials*, 17(2):145–151, February 2018.

[118] Yongbao Sun, Patrick Wen, Yoseob Yoon, Gangqiang Liu, Mark Steger, Loren N Pfeiffer, Ken West, David W Snoke, and Keith A Nelson. Bose-einstein condensation of long-lifetime polaritons in thermal equilibrium. *Physical review letters*, 118(1):016602, 2017.

[119] Bryan Nelsen, Gangqiang Liu, Mark Steger, David W Snoke, Ryan Balili, Ken West, and Loren Pfeiffer. Dissipationless flow and sharp threshold of a polariton condensate with long lifetime. *Physical Review X*, 3(4):041015, 2013.

[120] Mark Steger, Gangqiang Liu, Bryan Nelsen, Chitra Gautham, David W Snoke, Ryan Balili, Loren Pfeiffer, and Ken West. Long-range ballistic motion and coherent flow of long-lifetime polaritons. *Physical Review B*, 88(23):235314, 2013.

[121] TCH Liew, AV Kavokin, and IA Shelykh. Optical circuits based on polariton neurons in semiconductor microcavities. *Physical Review Letters*, 101(1):016402, 2008.

[122] F Hu, Y Luan, ME Scott, J Yan, DG Mandrus, X Xu, and Z Fei. Imaging exciton–polariton transport in mose 2 waveguides. *Nature Photonics*, 11(6):356–360, 2017.

[123] TCH Liew, AV Kavokin, T Ostatnickỳ, M Kaliteevski, IA Shelykh, and RA Abram. Exciton-polariton integrated circuits. *Physical review B*, 82(3):033302, 2010.

[124] M Boozarjmehr, M Steger, K West, LN Pfeiffer, DW Snoke, AG Truscott, EA Ostrovskaya, and M Pieczarka. Spatial distribution of an optically induced excitonic reservoir below exciton-polariton condensation threshold. *arXiv preprint arXiv:1912.07765*, 2019.

[125] Maciej Pieczarka, Maryam Boozarjmehr, Eliezer Estrecho, Yoseob Yoon, Mark Steger, K West, Loren N Pfeiffer, Keith Adam Nelson, David W Snoke, AG Truscott, et al. Effect of optically induced potential on the energy of trapped exciton polaritons below the condensation threshold. *Physical Review B*, 100(8):085301, 2019.

[126] Yongbao Sun, Yoseob Yoon, Saeed Khan, Li Ge, Mark Steger, Loren N Pfeiffer, Ken West, Hakan E Türeci, David W Snoke, and Keith A Nelson. Stable switching among high-order modes in polariton condensates. *Physical Review B*, 97(4):045303, 2018.

[127] Maciej Pieczarka, Eliezer Estrecho, Maryam Boozarjmehr, Olivier Bleu, Mark Steger, Kenneth West, Loren N Pfeiffer, David W Snoke, Jesper Levinsen, Meera M Parish, et al. Observation of quantum depletion in a non-equilibrium exciton–polariton condensate. *Nature communications*, 11(1):1–7, 2020.

[128] Yongbao Sun, Yoseob Yoon, Mark Steger, Gangqiang Liu, Loren N Pfeiffer, Ken West, David W Snoke, and Keith A Nelson. Direct measurement of polariton–polariton interaction strength. *Nature Physics*, 13(9):870–875, 2017.

[129] E Estrecho, T Gao, N Bobrovska, D Comber-Todd, MD Fraser, Mark Steger, K West, LN Pfeiffer, J Levinsen, MM Parish, et al. Direct measurement of polariton-polariton interaction strength in the thomas-fermi regime of exciton-polariton condensation. *Physical Review B*, 100(3):035306, 2019.

[130] Daniele Sanvitto and Stéphane Kéna-Cohen. The road towards polaritonic devices. *Nature Materials*, 15(10):1061–1073, October 2016.

[131] Alexis Askitopoulos, Lucy Pickup, Sergey Alyatkin, Anton Zasedatelev, Konstantinos G. Lagoudakis, Wolfgang Langbein, and Pavlos G. Lagoudakis. Giant increase of temporal coherence in optically trapped polariton condensate, 2019.

[132] M Sich, JK Chana, OA Egorov, Helgi Sigurdsson, IA Shelykh, DV Skryabin, PM Walker, E Clarke, B Royall, MS Skolnick, et al. Transition from propagating polariton solitons to a standing wave condensate induced by interactions. *Physical review letters*, 120(16):167402, 2018.

[133] Seonghoon Kim, Bo Zhang, Zhaorong Wang, Julian Fischer, Sebastian Brodbeck, Martin Kamp, Christian Schneider, Sven Höfling, and Hui Deng. Coherent polariton laser. *Physical Review X*, 6(1):011026, 2016.

[134] LK Thomsen and HM Wiseman. Atom-laser coherence and its control via feedback. *Physical Review A*, 65(6):063607, 2002.

[135] DM Whittaker and PR Eastham. Coherence properties of the microcavity polariton condensate. *EPL (Europhysics Letters)*, 87(2):27002, 2009.

[136] Jürgen Berges, Sz Borsányi, and Christof Wetterich. Prethermalization. *Physical review letters*, 93(14):142002, 2004.

[137] Michael Gring, Maximilian Kuhnert, Tim Langen, Takuya Kitagawa, Bernhard Rauer, Matthias Schreitl, Igor Mazets, D Adu Smith, Eugene Demler, and Jörg Schmiedmayer. Relaxation and prethermalization in an isolated quantum system. *Science*, 337(6100):1318–1322, 2012.

[138] Xuekai Ma, Ulf Peschel, and Oleg A Egorov. Incoherent control of topological charges in nonequilibrium polariton condensates. *Physical Review B*, 93(3):035315, 2016.

[139] Tim Langen, Thomas Gasenzer, and Jörg Schmiedmayer. Prethermalization and universal dynamics in near-integrable quantum systems. *Journal of Statistical Mechanics: Theory and Experiment*, 2016(6):064009, 2016.